A study on homonymous visual field deficits using brain imaging and simulations

by Anthony Beh, MSc

Thesis submitted to the University of Nottingham
for the degree of Doctor of Philosophy

Aug 2022

Abstract

Homonymous visual field deficit (HVFD) is a common and devastating complication of cerebral strokes. This impairment has a dramatic impact on quality of life, disrupting multiple facets of daily life – most notably reading fluency. At present, there are no universally accepted, effective rehabilitation programs for HVFD. The most promising strategies involve repetitive visual stimulation in the ‘blind’ field using a broad range of stimuli to perceptually “retrain” visual function. Although effectiveness of this approach varies substantially, it could be because the most appropriate areas of the field are not targeted or the stimulus used in training is not optimized for each patient. A major issue in rehabilitating HVFD is the heterogeneity across individuals, where there is variability in lesion size, location, time since lesion, and most importantly the pattern of residual visual capacity. The potential for recovery may be limited to individuals with intact cortical structures or alternative visual pathways that could support some level of visual reorganization.

To address this issue, this thesis discusses the use of a cross-modal imaging approach to characterize HVFD, complementing standard visual assessments and perimetry with high-resolution definitions of patient-specific patterns of residual visual field coverage and cortical integrity. Here I present detailed perimetry and brain imaging datasets from 4 stroke survivors with HVFD (2 with hemianopia, 2 with

quandrantanopia). My data reveals mismatches between the perimetry and functional responses mapped using functional magnetic resonance imaging (fMRI), revealing robust measures of residual visual capacity in the ‘blind’ field for all stroke survivors. I also used a probabilistic atlas to link functional activity to defined anatomical regions as well as major white matter tracts from probabilistic tractography. Taken together, this information provides a useful platform for a personalized approach to therapy – guided by functional activity patterns in the post-stroke brain.

Building on the idea of restoring visual function, this thesis also explores how recovery in the blind field can address reading impairments caused by HVFD. By visually manipulating an image in a single hemifield with a low-pass spatial filter under a gaze contingent paradigm, I could functionally simulate hemianopia. This also allowed me to systematically degrade spatial information in the hemianopic field and make inferences about the extent of visual field recovery required via restitutive HVFD strategies to restore functional reading performance. Consequently, this experiment also acts as a starting point to explore effects of visual restoration on reading with HVFD and allows us to test new strategies in healthy controls, before translating to patient groups.

Finally, this thesis outlines potential future directions for this line of investigation. These ideas include the development of rehabilitative strategies guided by patient-specific information using cross-modal imaging and testing out different configurations of visual manipulation in the simulated hemianopia design.

Acknowledgements

I would like to express my deepest gratitude to Denis Schluppeck, Paul McGraw and Ben Webb, for their guidance and patience have made my PhD journey a cherished memory and a fruitful experience. I would like to extend my sincere appreciation to all who have participated in my research. Additionally, this endeavour would not be possible without the generous support from Fight for Sight who funded this project.

Finally, I would like to thank my parents for supporting me through my education and career choices, my loving girlfriend for motivating and encouraging me through difficult moments, and also my friends for believing in me.

Contents

1 Homonymous Hemianopia **12**

1.1 Overview . . . 12

1.2 Pathogenesis . . . 13

1.3 Prevalence and diagnosis . . . 16

1.4 Reading with HVFD . . . 20

1.5 Recovery and Rehabilitation . . . 23

1.5.1 Compensatory strategies . . . 23

1.5.2 Substitution strategies . . . 24

1.5.3 Restitutive strategies . . . 25

1.6 Residual visual capacity . . . 29

1.7 Thesis outline . . . 33

1.7.1 Cross-modal imaging better characterizes heterogeneity across stroke survivors . . . 33

1.7.2 Simulating hemianopia to investigate reading impairments . . . 36

2 Recruiting Stroke Survivors **38**

2.1 Overview . . . 38

2.2 Participants . . . 39

2.3 Vision Tests . . . 42

2.4 Measuring visual field defect 44
2.4.1 Static Perimetry 44
2.4.2 Kinetic Perimetry 51
2.4.3 Microperimetry 53
2.5 Spatial Neglect 57
2.6 Fixation Stability 59

3 Brain imaging pipeline 61

3.1 Overview 61
3.2 Stimulus Presentation 63
3.3 Participants 66
3.4 Imaging Protocol 67
3.4.1 Anatomical scans 67
3.4.2 Diffusion-weighted imaging (DWI) 68
3.4.3 Functional scans 71
3.5 General Preprocessing Steps 74

4 Mapping Functional Responses 76

4.1 Overview 76
4.2 Retinotopic maps 78
4.3 Population Receptive Field Mapping 84
4.3.1 Constructing the model 85
4.3.2 Assessing the model fit 90
4.3.3 Visual field coverage maps 92
4.4 Using a probabilistic atlas to define visual regions 96
4.5 Visual field maps reveal cortical responses in “blind” portions of visual field 98

5 Anatomy and White Matter Integrity 105

5.1 Overview 105

5.2 Lesion brain segmentation 107

5.3 Brain extraction on lesion datasets 109

5.4 Semi-automatic lesion segmentation using ITK-SNAP 111

5.4.1 Defining a lesion mask 111

5.4.2 Managing ventricles 117

5.5 Registering and normalizing the lesion mask to standard space 120

5.6 Probabilistic atlas 123

5.7 Anatomical results 126

5.8 T2-weighted images 129

5.9 Analysis of diffusion weighted data 130

5.10 Distortion correction and skull stripping 131

5.11 Fitting a tensor model 134

5.12 Probabilistic tractography 136

5.13 Diffusion-weighted imaging indicates tract-level damage . . . 138

6 Cross-modal insights 141

6.1 Overview 141

6.2 Mismatches between perimetry and imaging defined responses 142

6.2.1 Perimetry and anatomical MRI 142

6.2.2 Perimetry and visual responses in functional MRI . . . 143

6.2.3 Perimetry and diffusion weighted imaging /tractography 144

6.3 Potential sites for rehabilitation and optimal stimuli for perceptual learning 146

6.4 Conclusions 149

7 Simulated Hemianopia 150

7.1 Overview 150

7.2 Materials and methods 152

7.2.1 Participants 152

7.2.2 Reading stimuli 152

7.2.3 Eye tracking and gaze contingent viewing 154

7.2.4 Procedure 158

7.3 Raw eye movement traces 159

7.4 Adaptive velocity-based algorithm 161

7.4.1 Key parameters 161

7.4.2 Filtering and denoising 162

7.4.3 Velocity Threshold Estimation 164

7.4.4 Saccade detection 166

7.4.5 Glissade detection 168

7.4.6 Fixation detection 169

7.4.7 Manual data quality control 169

7.5 Dynamic Time Warping 171

7.6 Comparisons with patient population 176

7.7 Progressive blurring provides insight on reading with HVFD . 181

7.7.1 The effect of spatial filtering on hemianopic reading . 181

7.7.2 Median fixation duration while paragraph reading . . 188

7.8 Discussion 191

8 General conclusions 198

8.1 Overview 198

8.2 Summary of findings 199

8.3 Future directions 204

8.3.1 Using imaging to guide perceptual learning based training programs 204

8.3.2 Improve upon current analysis of the visual deficit and imaging data 208

8.3.3 Test different configurations of visual manipulations in the gaze contingent paradigm 210

8.4 Concluding remarks 212

Bibliography 213

List of Figures

1.1 Visual illustration of homonymous visual field defect (HVFD). 15
1.2 Visual illustration of macular sparing in homonymous visual field defect (HVFD). 15
1.3 Examples of visual fields testing for hemianopia. 18
1.4 Example of CT scan in right homonymous hemianopia. 19

2.1 Example of a field plot with high pattern defect and overall defect. 47
2.2 Definition of homonymous visual field loss with perimetry for both eyes. 48
2.3 Scatter plots of visual sensitivity as a function of eccentricity for perimetry results. 50
2.4 Kinetic perimetry example. 53
2.5 Microperimetry measurements across 4 stroke survivors. . . . 56
2.6 Example of successful stable gaze fixation during the mock session. 60

3.1 Example of the stimuli presented in the scanner. 65
3.2 Visualization of three diffusion tensors shapes 71

4.1 Pipeline for mapping residual visual function in stroke survivors using functional magnetic resonance imaging (fMRI). 77

4.2 Example of a correlation analysis on a single voxel with a high coherence value. 79
4.3 Correlation analysis results for both ring and wedge scans. . . 81
4.4 Correlation analysis results for ring and wedge scans overlaid on an inflated surface of the lesioned hemisphere . . 82
4.5 Flat maps of both lesioned and healthy hemispheres. 83
4.6 Visualization of pRF model prediction of a single voxel. 88
4.7 Example of a good fit between the predicted BOLD response and the measured time series. 89
4.8 Example of a pRF model represented in visual space. 90
4.9 Population receptive field analysis results. 91
4.10 Population receptive field analysis results overlaid on an inflated surface. 92
4.11 Population receptive field model representation in visual space. 94
4.12 Normalized and non-normalized visual field coverage maps from visually responsive regions in the lesioned hemisphere. . 95
4.13 Visual field maps derived from functional MRI and population receptive field analysis. 102
4.14 Quantifying and visualizing residual function from population receptive fields. 104

5.1 Pipeline for semi-automatic lesion segmentation. 108
5.2 Examples of skull-stripping high resolution anatomical images using FSL-Brain Extraction Tool (BET) and Optimized Brain Extraction for Pathological Brains (optiBET). 110
5.3 Example of lesion identification using ITK-SNAP. 114

5.4 Example of thresholding to isolate the lesioned tissue in subject. 115
5.5 Setting up for active contour segmentation. 116
5.6 Final contour shape of the lesioned tissue. 116
5.7 Example of lesion mask (created using ITK-SNAP pipeline) for subject-14326. 117
5.8 Process of creating the ventricle mask using ITK-SNAP. 119
5.9 Charaterizing the lesion on a standard brain (MNI template). 122
5.10 Location of cortical ROIs from L. Wang et al. (2015) atlas. . . 124
5.11 Example of lesion characterization of subject 11773. 125
5.12 Characterization and quantification of anatomical lesions across each participant with reference to perimetry results. . . 128
5.13 T1-weighted and T2-weighted images of the lesion. 129
5.14 Pipeline for diffusion tensor imaging analysis. 130
5.15 Calibration images acquired from the anterior and posterior phase directions. 132
5.16 Comparisons between skull stripping using BET for the T1-weighted image and diffusion-weighted image. 133
5.17 Example of FA map with standard RGB color map modulated using the underlying FA values. 135
5.18 White matter intactness, results from diffusion weighted imaging and analysis. 140

7.1 Response function of the 10th order Butterworth filter at various frequencies. 156
7.2 Example of gaze contingent blurring on the text stimuli. . . . 157

7.3 Samples of raw eye traces along the x-coordinate domain in an experiment trial for control, right simulated HVFD and left simulated HVFD. 160

7.4 Comparing unfiltered data against Savitzky-Golay filtered data. 164

7.5 Examples of velocity threshold estimation across participants with different levels of noise in their eye movement velocity profiles. 166

7.6 Detecting saccades using adaptive event detection algorithm. 168

7.7 Sample of eye traces on text image. 170

7.8 Using dynamic time warping to mark first and final fixation on a line. 175

7.9 Oculometric measures across simulated HVFD sides for both old and young adult groups, along with corresponding measurements from patients with HVFD. 179

7.10 Average median forward saccade amplitude and average median fixation duration across simulated HVFD sides for both old and young adult groups. 180

7.11 Oculometric measures from simulated hemianopic reading at different levels of spatial blurring (pooled across age groups). 186

7.12 Oculometric measures from simulated hemianopic reading at different levels of spatial blurring. 187

7.13 Average median fixation duration across paragraph sections for both left and right HVFD at different cut-off frequencies. . 190

8.1 Diagram of possible developments to investigate the relationship between restitutive training related improvements and spared functional/anatomical circuits. . . 207

8.2 Example of a new design to study visual restoration and reading performance. 211

List of Tables

2.1 Demographic and basic clinical information of participants. . 40
2.2 Results of optometric assessment for each participant (both eyes), describing the visual field defect, refractive status, distance visual acuity (VA),near addition and near visual acuity (VA) 43
2.3 Perimetry results (standard clinical scores). 49

4.1 Differences in population receptive field coverage in lesioned and healthy hemispheres. 101

7.1 Oculometric measures for control, right HVFD and left HVFD. 178
7.2 Statistical summary of mixed design repeated measures ANOVA. 185

Chapter 1

Homonymous Hemianopia

1.1 Overview

This chapter will introduce homonymous visual field defects (HVFD) that manifest post-stroke, discussing their pathology, prevalence, diagnosis and notable impairments. I will also discuss the strategies employed for rehabilitation and how residual visual capacity plays a role in recovery. I will then outline the project and experiments included in my PhD thesis in a brief “thesis outline”.

1.2 Pathogenesis

Homonymous visual field defects (HVFD) are a form of a visual impairment characterised by a complete loss of conscious vision in the contralateral visual field in both eyes, caused by postgeniculate damage to the visual system (J. L. Smith, 1962). This area of loss, also known as a scotoma, can range from an entire hemifield (hemianopia, sometimes referred to as hemianopsia) to a single visual field quadrant (quadrantanopia)[1] as illustrated in Figure 1.1.

Alternatively, hemianopia is also known as a complete homonymous hemianopia (HH), while quadrantanopia is classified as an incomplete HH (Goodwin, 2014). For incomplete HH, they are categorised into congruous or incongruous visual field defects, signifying the congruency of the pattern of defects between both eyes. The congruency of the defect has been believed to be directly determined by the location of the lesion but this remains a point of debate (Kedar et al., 2007). The scope of the thesis will only focus on congruous visual field defects (similar patterns of HVFD across both eyes).

The most common cause of HVFD is stroke (52%-70%), but it has also been reported in cases of traumatic brain injury (14%) and tumours (11%) (Goodwin, 2014; Zhang et al., 2006c). All reported cases found

---

[1] Although this nomenclature is widely accepted, other terms are also sometimes used.

lesions in the retrochiasmal visual pathway, involving damage to the optic tract, lateral geniculate nucleus (LGN), optic radiation, and/or occipital cortex (J. L. Smith, 1962; Zhang et al., 2006a). Lesion sites are located in the contralateral hemisphere, causing a loss of visual awareness in the corresponding visual field.

Stroke survivors with this condition typically have good ocular health, i.e structures in and around the eyes remain functional, but report that they are unable to see in one side of their field of vision. Depending on the location of the lesion, the representation of the macular region, which extends to the central 5-25° of visual field on the affected side, can be spared (Zhang et al., 2006b) (see Figure 1.2) — but in some cases it is lost.

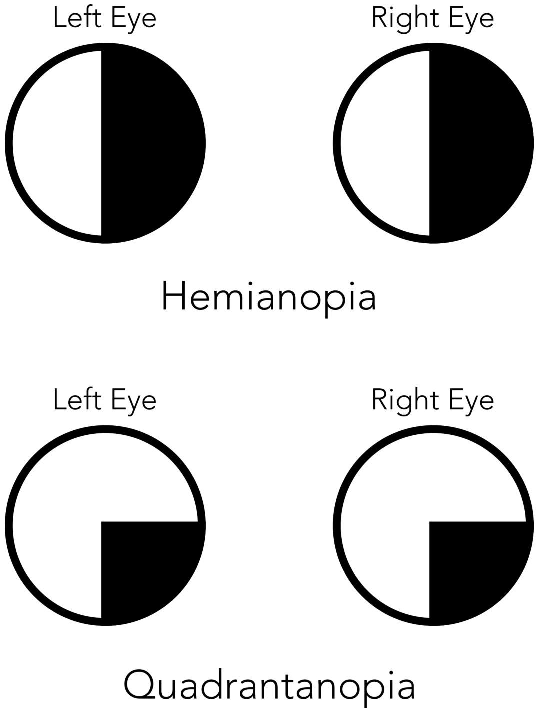

Figure 1.1: Visual illustration of homonymous visual field defect (HVFD). The black area depicts regions in which patients are unable to perceive visual information during a visual examination. In HVFD, both eyes will have a similar pattern of ‘blindness’, which could manifest in one half of the hemifield (hemianopia) or one quadrant of the visual field (quadrantanopia)

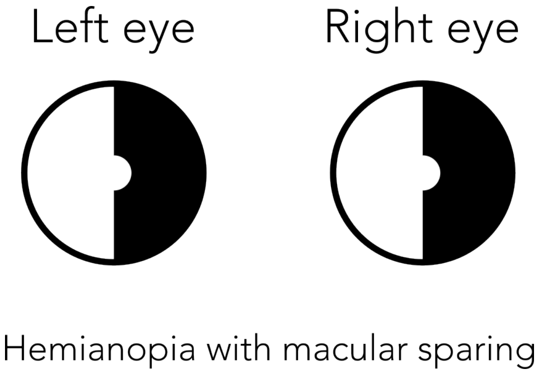

Figure 1.2: Visual illustration of macular sparing in homonymous visual field defect (HVFD). Macular sparing could extend to the central 5-25° of visual field on the affected side.

1.3 Prevalence and diagnosis

In the UK, approximately 110,000 cases of stroke are reported per year in England alone (Office, 2010). The literature shows that 13 - 49% of stroke survivors report visual field impairment after the stroke (Barker & Mullooly, 1997; Rowe et al., 2019; Rowe et al., 2013; Townend et al., 2007). The large variance in prevalence estimates reported across different studies could be attributed to how HVFD in stroke survivors are diagnosed.

The standard vision tests commonly used by the neurologists or neuro-ophthalmologists include Goldmann visual field testing, Humphrey visual field testing, or confrontation visual fields examination (Zhang et al., 2006b). If the perimetry tests reveal persistent field defects that are consistent across both eyes and ocular health is not compromised, HVFD is diagnosed. An example of these visual field tests can be seen in Figure 1.3. In some cases, the diagnosis is accompanied by a CT scan or magnetic resonance imaging (MRI) scan of the brain to confirm the lesion (Zhang et al., 2006b), as seen in Figure 1.4.

The evaluation of visual field defects is commonly conducted 1 to 6 months after the stroke (Zhang et al., 2006a), as the symptoms are less prominent compared with other stroke-related impairments, such as motor function loss, in most circumstances. Additionally it is often not routine practice for clinicians to perform a vision exam in their assessment in stroke survivors (Rowe, 2010), hence HVFD is often overlooked. This variable delay between the stroke onset and diagnosis of the visual impairment could be a key factor in the high variance in prevalence, especially when considering reports of spontaneous recovery post stroke (Cramer, 2008) within the first 3 months. In cases where clinicians do perform a vision exam, the widely utilised and easily conducted confrontation examination (Townend et al., 2007) greatly underestimate the prevalence of HVFD symptoms as compared automated perimetry (Johnson et al., 2011), which is more accurate and sensitive tool in assessing visual fields.

Other, non-visual, deficits are sometimes misidentified as vision loss. For example, patients with unilateral spatial neglect, a condition where the individual fails to respond to stimuli in the side contralateral to the lesioned hemisphere, may sometimes be misdiagnosed with HVFD (Walker et al., 1991). This is because in visual field tests (most commonly perimetry), failure to respond to the visual stimuli is interpreted as a visual defect instead of an attentional impairment. Hence, clinicians may require secondary tests to disentangle the relative effects of HVFD and unilateral spatial neglect. A commonly used test to identify spatial neglect is the line bisection task (Gammeri et al., 2020).

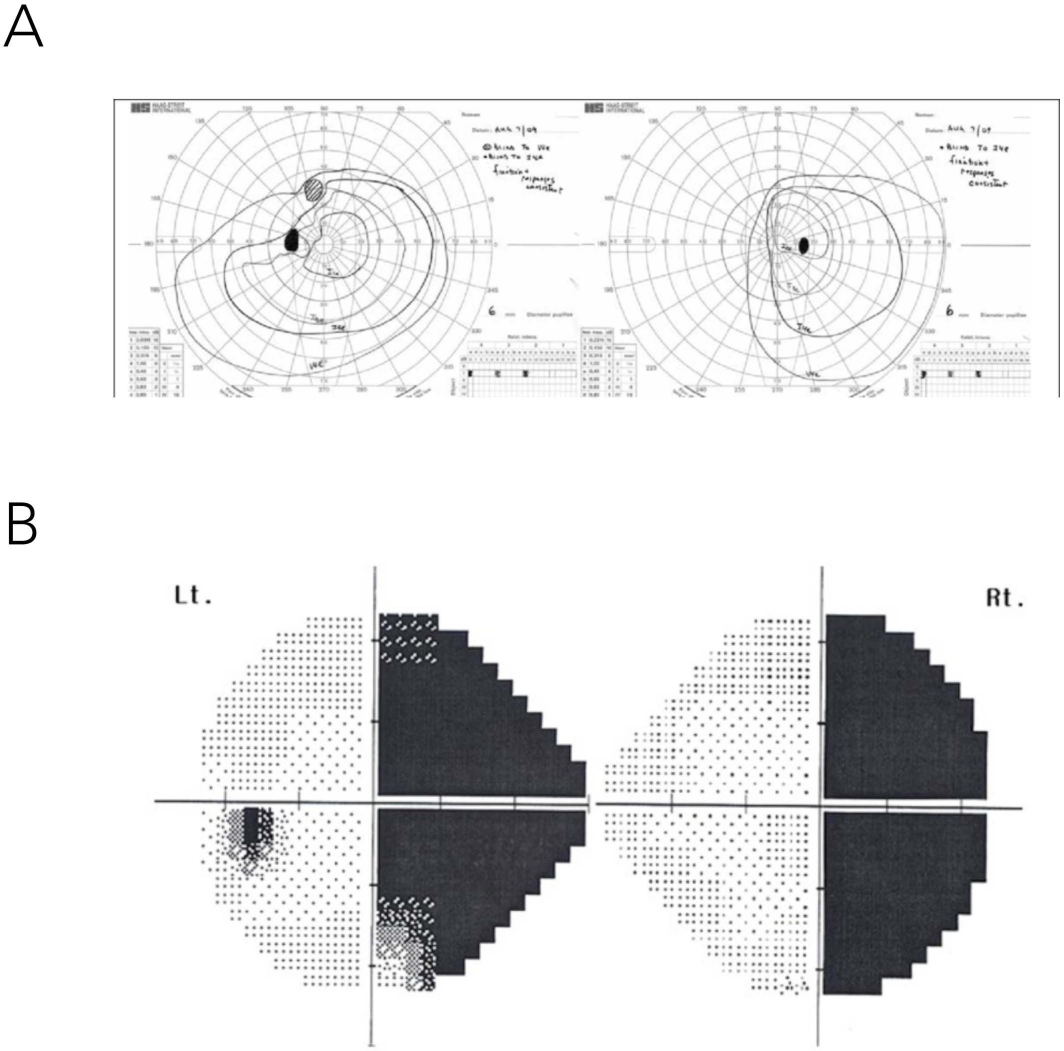

Figure 1.3: Examples of visual fields testing for hemianopia. The left-sided results represent the left eye and vice versa for the right-sided result (A) Goldmann visual fields test reveal incongruous left homonymous hemianopia, taken from Uppal et al. (2012). Note that in the Goldmann visual fields test the field assessment is flipped along the x-axis, whereby left is right and vice versa. (B) Humphreys visual fields test reveal complete right homonymous hemianopia, taken from Yeon et al. (2013). The different patterns in the fields test reflect different levels of visual sensitivity, where completely ‘black’ regions show no sensitivity to light.

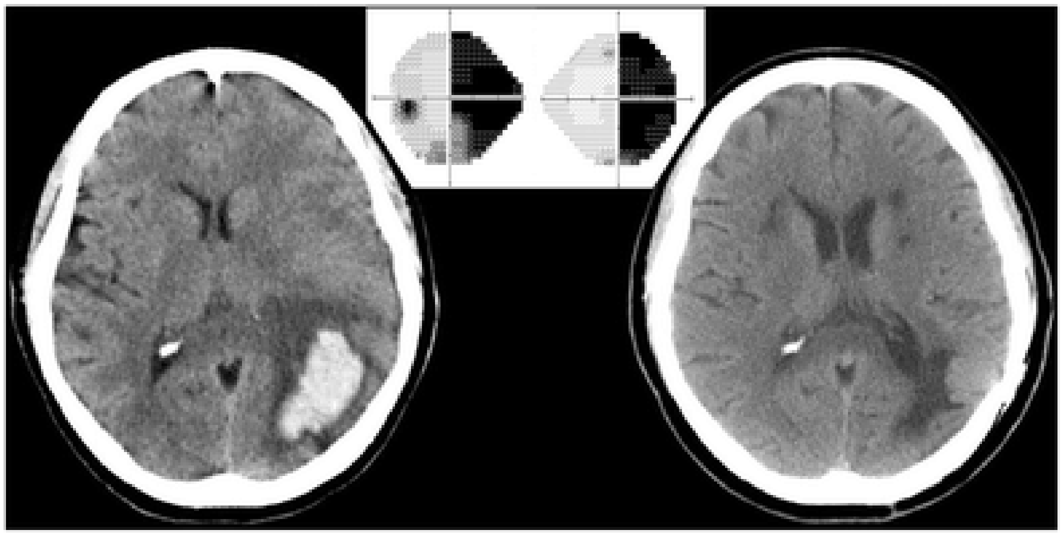

Figure 1.4: Example of CT scan revealing acute left hematoma resulting in a right homonymous hemianopia, taken from (Horton et al., 2017).

1.4 Reading with HVFD

HVFD has a dramatic impact on quality of life because it functionally impairs performance on many routine visual tasks (Papageorgiou et al., 2007). Individuals with this condition have trouble navigating unfamiliar and crowded environments and their ability to drive safely in traffic is compromised[2] (Bowers et al., 2014; Goodwin, 2014; Szlyk et al., 2005; Wood et al., 2011). However, one of the most prominent visual problems is a significant loss in reading ability (hemianopic dyslexia, Zihl (1995)).

Reading is a highly complex task with multiple levels of representation, ranging from low level orthographic, phonological and morphological processing to higher level lexical, semantic and syntactic representation (Schotter et al., 2012). However, it ultimately relies on the brain receiving the appropriate visual information through precise oculomotor control mechanisms that bring the area of highest acuity (fovea) to fixate on a region of text and then serially reposition it as reading progresses (Rayner, 1998).

Unsurprisingly, the loss of conscious vision in one half of the visual field has a severe impact on reading ability (Schuett et al., 2008a; Trauzettel-Klosinski & Brendler, 1998a; Zihl, 1995). A key component that

---

[2] In the UK, this would typically result in the license to drive being revoked.

is disrupted by stroke is the perceptual span – defined as the window of useful vision available during fixation (McConkie & Rayner, 1975). It is asymmetrical in shape, typically extending 3-4 letter spaces left of fixation and 14-15 letter spaces to the right of fixation (McConkie & Rayner, 1976; Rayner, 1998; Rayner et al., 2010; Schotter et al., 2012). Although visual information crucial for reading is imaged on the foveal region (up to 2° from fixation), readers often extract useful parafoveal (2-5°) information from the next word or two in the sequence. Despite poorer visual acuity in the parafoveal retina, it is a vital component in reading fluency as it provides a 'preview' of the next word (right of fixation) or the word before (left of fixation). This preview benefit has been shown to inform 'when' and 'where' the eyes should move, having a facilitatory effect on word processing during periods of stable fixation and regulating future eye movements to new areas of text (Drieghe et al., 2005; Kennedy, 2000; Morris et al., 1990; Paterson & Jordan, 2010; Pollatsek & Rayner, 1982; Rayner et al., 1982; Schotter et al., 2012; Williams et al., 2006). In hemianopic field loss, parafoveal processing is compromised, resulting in significantly slower reading speeds (Schuett, 2009; Schuett et al., 2008a; Trauzettel-Klosinski & Brendler, 1998a).

The side on which the HVFD (left or right hemifield) occurs differentially impacts eye movements during reading. This has been linked to the idea that the vision loss affects different regions of the perceptual span (Schuett et al., 2008a; Trauzettel-Klosinski & Brendler, 1998a; Zihl, 1995). For instance, individuals with left HVFD find it difficult to re-fixate to the new line of a paragraph during a return sweep, often requiring multiple saccades to find the start of the new line. In contrast, right HVFD affects eye movements in left-to-right reading more, leading to a larger number of smaller forward (rightwards) and regressive saccades (leftwards), more fixations which are usually longer in duration, ultimately resulting in much slower reading speeds.

1.5 Recovery and Rehabilitation

At present, there are no universally accepted, effective rehabilitation programs for HVFD. Several strategies have been developed in the past few decades, each accompanied with its own advantages and disadvantages (Das & Huxlin, 2010; Pollock et al., 2011). In some instances, patients experience a spontaneous recovery from HVFD within the early periods post-stroke (Cramer, 2008; Zhang et al., 2006a). This has been attributed to the resolution of inflammation and edema around the lesion along with the re-activation of partially damaged perilesional neural circuits (Poggel et al., 2001; Sabel, 1997). However, it has been observed that after a 6 month period post-stroke, almost no further improvement can be found (Zhang et al., 2006a).

1.5.1 Compensatory strategies

A common intervention strategy involved compensating for the deficit by training the eye to move the ‘seeing’ field towards the ‘blind’ field to mitigate the visual field defect. The training typically involves employing larger initial saccades into the hemianopic hemifield followed by a systematic search pattern to improve detection and reaction time to visual stimuli (Mannan et al., 2010; Nelles et al., 2001; Nelles et al., 2009; Roth et al., 2009; Zihl, 1995). This change in oculomotor strategy has been shown to shorten reaction time and improve saccadic localization to visual stimuli that appear in the ‘blind’ field. It is also inexpensive, quick to train and can be conducted at home which is a major benefit to most stroke survivors with this condition (Mannan et al., 2010). Although compensatory eye movement training does not change the size of the deficit in any significant manner (Pambakian et al., 2004), it remains as an important tool that improves visual search ability and has also demonstrated transfer effects to daily living activities[3].

1.5.2 Substitution strategies

Some treatment approaches for HVFD have involved optical devices such as mirrors, telescopes and most notably prisms to substitute the visual field as opposed to expanding them (Duszynski, 1955; Goodlaw, 1983; Peli, 2000). The total active visual field does not change but scenes from the ‘blind’ field are relocated into the ‘seeing’ field through such optical methods. This intervention has been shown to be an effective tool in improving mobility and navigating through obstacles in the environment (Bowers et al., 2014; Giorgi et al., 2009). New developments in prism designs (oblique peripheral prisms) allow for a larger field expansion - extending up to 30°, improving hazard detection when driving (Bowers et al., 2012; Houston et al., 2018; Peli et al., 2016). Training is required when first using prismatic devices, as it is important to avoid looking directly into

---

[3] Some strategies have also incorporated the training of head scanning movements to allow for larger gaze shifts to address driving ability and safety (Bowers et al., 2014; Wood et al., 2011).

the prism to avoid diplopia[4]. Challenges that come with wearing prism glasses involve difficulty descending stairs, glare and objects suddenly appearing through the prism (jack-in-the-box effect) (Giorgi et al., 2009). This intervention is also not well suited for supporting near-vision activities such as reading.

1.5.3 Restitutive strategies

Compensatory and substitution strategies have found substantial success in improving various aspects of daily living in stroke survivors with HFVD and often are used in conjunction with one another (Goodwin, 2014). Both strategies involve accepting the deficit and developing solutions around them, but what about programs that attempt to reverse the effects of the visual field loss or restitutive strategies?

Restitution is based on the concept of adult neuroplasticity, the generation of new neurons (neurogenesis) or formation of new connections and pathways in adult brains. Five decades of neurogenesis research has showcased the existence of neurogenesis in adult species, such as rodents (Altman & Das, 1965), birds (Nottebohm, 1989), nonhuman primates (Graziadei et al., 1980; Kornack & Rakic, 1999; Miller & Nowakowski,

---

[4] This is only an issue for monocular sector prisms; peripheral prisms are less affected by this visual confusion due to lower acuity at larger eccentricities (Cohen & Waiss, 1996; Peli, 2000).

1988) and most notably in humans too (Eriksson et al., 1998; Spalding et al., 2013). However, it is worth emphasizing that these observations do not necessarily extend beyond very specific neural populations. The implications drawn from these findings suggest that it might be possible to develop interventions that tap into the brain's potential for plasticity with the goal of recovering functionality in damaged brain regions (Fuchs & Flügge, 2014). For stroke-related injuries, physical rehabilitation is unequivocally recommended for patients with motor cortex damage, reporting relative success in clinical improvements (Hallett, 2002; Takeuchi & Izumi, 2013). However, for visual field loss caused by stroke damage, a reversal of visual field loss is often controversial and has even been opposed amongst clinicians (Cavanaugh et al., 2020; Horton et al., 2017).

Early restitutive strategies involved using computer-based training programs (formally known as visual restitution training - VRT) to repeatedly stimulate along the borders of the blind field to enlarge the effective visual field (Kasten et al., 2000; Kasten & Sabel, 1995; Kasten et al., 1998; Poggel et al., 2010). Reports claimed that VRT significantly improved detection accuracy in the 'blind' field and shifted the absolute visual field border by an average of 5° of visual angle. However, as highlighted by Horton (2005), as both the therapy and training-related changes were measured using the same method (and software), there was a potential confound of visual learning effects. The visual field improvements were also not reproducible when tighter fixation control was implemented during performance tests (Reinhard et al., 2005). The most recent work on VRT showed some modest improvement in field enlargement and control for eye movements using microperimetry, but only in a study with a relatively small sample size (Marshall et al., 2010).

A different approach to restitution lies in the phenomenon known as 'blindsight', where individuals are able to detect, localise or discriminate visual stimuli in the hemifield with an apparently complete visual loss (Cowey, 2010; Sanders et al., 1974). Since its initial discovery, there have been multiple reports of residual visual capacity in cortically blind individuals (Barbur et al., 1993; Silvanto et al., 2008; Silvanto et al., 2009; Walker et al., 2000; Weiskrantz et al., 1995). If the damaged cortex still retains the capacity to respond to visual targets, repeated stimulation (via training) of specific visual stimuli could induce functional reorganisation in the "blind" field (Huxlin et al., 2009; Sahraie et al., 2006). This technique has been widely used in a range of visual deficits not related to stroke, such as amblyopia and age-related macular degeneration (Astle et al., 2015; Astle et al., 2011) and is emerging as an effective tool in rehabilitation.

To treat HVFD, different laboratories have implemented perceptual retraining using visual stimuli that are selective for different visual channels, including broadband spatial and temporal frequency patterns and stimuli optimised for motion perception (Barbot et al., 2020; Casco et al., 2018; Huxlin et al., 2009; Pleger et al., 2003; Sahraie et al., 2006). Even after controlling for unstable fixation, they were able to establish clinically significant improvements at training locations. However the effectiveness of perceptual retraining in treating HVFD following stroke appears limited, as improvements tend to vary substantially across individuals. A recent clinical trial using a motion discrimination task for training highlighted this problem, showing no improvements over controls in visual field measures in a large cohort of stroke survivors (Cavanaugh et al., 2020).

1.6 Residual visual capacity

Why is it the case that not all individuals benefit from this restitutive or restorative approach to HVFD? To address this question, it is important to explore the mechanisms behind restoring visual function in the blind field, and what this means in terms of identifying residual visual capacity in cortically blind patients. Broadly speaking, functional recovery in the "blind" field has been attributed to two possible mechanisms (Das & Huxlin, 2010):

- strengthening of alternative visual pathways or
- functional reorganisation of the spared cortex.

The classic view of the visual analysis suggests sequential processing and refinement of signals: inputs received from the retina travel through the optic tract to an intermediate relay at the lateral geniculate nucleus (LGN) located in the thalamus, and ultimately to the primary visual cortex (V1) and higher cortical regions where more complex visual processing begins. However with the discovery of 'blindsight', the idea of alternative visual pathways became a popular topic of investigation. Famously, it was observed that patient G.Y. was able to discriminate motion stimuli presented in the 'blind' field (Weiskrantz et al., 1991). Although V1 was irrevocably damaged in one hemisphere, some level of visual awareness was retained in the 'blind' field. Imaging studies that investigated this phenomenon found that it was possible for visual signals to reach the extrastriate area MT/V5, which is sensitive to motion stimuli, by bypassing V1 entirely (Barbur et al., 1993; Bridge et al., 2008; Goebel et al., 2001; Holliday et al., 1997). Although MT/V5 primarily receives inputs from V1 through hierarchical feedforward connections from lower cortical regions, MT/V5 has also been found to receive projections that are independent of V1, and travel directly from the LGN (Sincich et al., 2004), the medial subdivision of the inferior pulvinar (PIm) (Warner et al., 2015) or from the superior colliculus through the pulvinar (Berman & Wurtz, 2010). Macaque studies have shown that these connections, if preserved, could mediate blindsight after receiving a V1 lesion in adulthood (Schmid et al., 2010; Warner et al., 2015). Using diffusion weighted imaging, Ajina et al. (2015) demonstrated that all patients in their sample with V1 damage, that were also capable of blindsight, showed an intact connection between the LGN and MT/V5.

Besides alternative visual pathways, the presence of spared cortices alongside the lesion site has been suggested as the basis for residual visual function in the blind field. In some cases, small 'islands' of spared V1 are identified through visual perimetry, behavioural experiments and functional magnetic resonance imaging (fMRI) (Dilks et al., 2007; Fendrich et al., 1992; Morland et al., 2004; Radoeva et al., 2008; Wessinger et al., 1999) and play an important role in functional recovery. The idea of neuroplasticity in adult humans remains controversial: some adult animal studies of the visual systems appear to demonstrate high degrees of plasticity (Calford et al., 2000; Kaas et al., 1990), but these results are in contrast to findings that show limited potential for any functional reorganization (Horton & Hocking, 1998; Smirnakis et al., 2005).

Interestingly however, by using high resolution imaging measurements to capture functional and structural changes during a plasticity period, Keck et al. (2008) demonstrated that when the lesion site was subjected to visual input, the initially unresponsive region regained responsiveness after 2 months, and this effect correlated with newly generated dendritic spines which persisted for extended periods of time. There is also an influential theory that functional reorganization in adult striate cortex is mediated by axonal sprouting of long-range horizontal connections mediated by pyramidal neurons (Darian-Smith & Gilbert, 1994).

Overall, the supporting evidence for restitutive approaches to therapy remains weak, but this may be because the most appropriate areas of the field are not targeted for each patient. A major issue in rehabilitating HVFD is the heterogeneity across individuals, where there is variability in lesion size, location, time since lesion, and most importantly the pattern of residual visual capacity. This heterogeneity presents a genuine barrier to restitutive strategies. Some restitutive approaches build upon previously established models of visual restoration, using specific channels of visual stimuli or training in locations near the border of the scotoma, and have achieved variable success in the patient population. As this method involves a large time commitment from the patient, it is important to be precise. The potential for recovery may be limited to individuals with intact cortical structures or alternative visual pathways that could support some level of visual reorganization.

Recent work by Barbot et al. (2021) showed strong evidence that it is possible to achieve clinically significant improvements in the blind field via training, if we can identify spared perilesional V1 regions in cortically blind patients. The training involved repetitive stimulation near the border of the scotoma, using both static orientation and global motion stimuli. They found that all patients were able to recover performance levels similar to the intact field, and the improvements were correlated with amount of spared V1 coverage of the blind field. However, the author highlights that although spared V1 regions are vital, they are not able to rule out the possibility that intact extrastriate areas also contribute to recovery.

It is clear that this approach to recovery shows great potential and invites room for further development and refinement. We now know that it is possible to induce training-related recovery in cortically blind patients and it is linked closely to surviving anatomical and functional circuits. If therapy could be better guided by anatomical evidence and functional activity patterns in the brain, it may improve rehabilitation approaches by delineating the visual field locations or brain structures with the best chance of functional recovery.

1.7 Thesis outline

1.7.1 Cross-modal imaging better characterizes heterogeneity across stroke survivors

The thesis will investigate HVFD using individualised anatomical and functional biomarkers to see how they link to perimetric measures of the visual field. A combination of cross-modal imaging data provides a powerful source of information to characterize the anatomy of the lesion and visual capacity of individual stroke survivors with HVFD and supports a personalized medicine approach to stroke intervention. This approach could potentially help address the marked variability in individual responses to rehabilitation strategies and generate new outcome measures for treatment.

At the outset of my thesis work, I had formed a plan for using this approach in a group of 10-12 stroke survivors. Initial visual fields testing were conducted for all participants using standardised static perimetry along with a full set of optometric measures. Anatomical MRI data were collected to measure the extent of injury caused by stroke, allowing me to quantify the lesioned and spared cortex in the occipital lobe. To determine the functional integrity of spared visual brain networks, fMRI responses to supra-threshold (retinotopic) visual stimuli presented at sequential points in visual space will be measured. This will allow the use of population receptive field (pRF) mapping to reconstruct a representation of visual space across different cortical areas of the visual brain. By estimating the centres and sizes of population receptive fields, I can then construct a coverage map of the visual field, allowing me to estimate the extent of ‘neural’ responses to visual input inside the scotomatous field defined by perimetry (Dumoulin & Wandell, 2008; Papanikolaou et al., 2014). To identify spared white matter fibres connecting brain areas in visual cortex within the lesioned hemisphere (and between hemispheres), I also acquired diffusion weighted imaging data (DWI) which I analysed with computational tractography to map out a set of identified tracts underpinning inter- and intra-hemisphere connectivity in occipital, temporal and parietal cortex (Leh et al., 2006; Puig et al., 2017).

This cross-modal approach will help shed new light on possible targets for rehabilitation in homonymous visual field loss. Higher-resolution definitions of the patient-specific patterns of residual visual field coverage and cortical integrity across stroke survivors could ultimately improve diagnosis and understanding of the disorder (Millington et al., 2017). While recovery of additional visual field – lost topographic information by damage in early visual areas (Donoghue, 1995; Karmarkar & Dan, 2006) – is unlikely (Horton et al., 2017; Wandell & Smirnakis, 2009), loss maps for higher-level regions that preferentially code e.g. colour, motion, objects or faces may be less affected (J. L. Chen et al., 2011). In that case, subjects may be able to ‘learn’ how to exploit this information in the residual field to support some visual behaviours.

Perhaps the mixed evidence for plasticity in adult humans – in the context of rehabilitation, is indicative of the fact that there are a combination of parameters that must be fulfilled in tandem in order to support adult plasticity, that we are still unaware of. Take for example the study that investigated plasticity in juvenile and adult barn owls (Brainard & Knudsen, 1998). As developing barn owls have a sensitive period where experience greatly shapes their sound localization behaviour, they were able to use optical prisms that displaced vision to alter the auditory space map in the owl's brain. Large adaptive changes in the auditory maps can be observed in juvenile barn owls but only negligible effects in adult barn owls, similar to findings in human samples (Wandell & Smirnakis, 2009). However, the same lab group have demonstrated that if adult barn owls are allowed to hunt for food (a natural and critical behaviour found in wild barn owls) as oppose to being fed during the prism adaption period, they were able to observe larger plasticity in adult barn owls (Bergan et al., 2005). This seems to suggest that in the adult population, it is not enough that the underlying circuitry can support plasticity, but it must also be accompanied with behaviourally relevant actions.

Hence it is vital that we establish tools that are more precise in identifying surviving circuits in individuals with HVFD, so that we can build behaviourally relevant training programs that target specific regions in the brain.

1.7.2 Simulating hemianopia to investigate reading impairments

Building on the previous idea, the thesis also explores how the recovery of visual function in the blind field can address one of the prevailing impairments of HVFD, namely reading fluency. As recent restitutive strategies with HVFD patients have been able to demonstrate perilesional recovery of luminance detection thresholds in the blind field (Barbot et al., 2021), it is important to investigate how this recovery can improve or restore some of the lost visual span for reading. To address this question, I employed a gaze contingent paradigm where the degree of spatial blurring in one hemifield was manipulated to simulate hemianopic loss (and potential recovery) and measure how this changes oculomotor behaviour during text reading. In conditions with high levels of blurring in the simulated field, visual information fundamental to text recognition and comprehension is no longer available (Kwon & Legge, 2012).

We argue that this method can be used in individuals with normal visual function to functionally simulate the effects of vision loss in each hemifield. By manipulating the degree of blurring, we systematically control access to spatial information in one hemifield and measure how this changes both the pattern of eye movements and reading speed. Because reading ability changes with age (Laubrock et al., 2006), two groups of observers – one with younger participants, another with older participants - closer in age to the risk group for ischaemic strokes (England, 2018) were recruited for this study. Findings from this experiment will open up the possibility of using participants with normal visual function to help identify the most promising strategies for HVFD, before translation to patient groups.

Chapter 2

Recruiting Stroke Survivors

2.1 Overview

This chapter will describe the stroke survivors recruited for this study, detailing our methods of recruitment and provide relevant clinical information about our participants. Here I discuss the visual assessments conducted for the project, which includes a comprehensive visual test battery, static perimetry, kinetic perimetry and microperimetry. This chapter will also discuss the assessment of spatial neglect – a potential confound in investigating visual field deficits, and assessing participant’s ability to maintain fixation stability (which will be important later on in the brain scanner, see Chapter 3).

2.2 Participants

Data was collected for 4 stroke survivors with HVFD (6 were recruited in total but 2 were excluded from the final analysis as they were not eligible to enter the MRI). A summary of demographic information can be found in Table 2.1. Participants were recruited through local communities (Nottingham Stroke Research Partnership Group, Nottingham Stroke Club) and advertising to stroke-related organisations (Stroke Association, DifferentStrokes). The inclusion criteria for participation in the study were: (1) Full informed consent, (2) showing symptoms of homonymous visual defect, (3) no evidence of retinal or optic nerve pathology, (4) no manifest strabismus, (5) good ocular motility, (6) absence of spatial neglect. All experiments were performed with ethical approval from the School of Psychology ethics committee (F944/F1055R) and all participants gave written, informed consent.

Table 2.1: Demographic and basic clinical information of participants.

Participant ID	Sex	Age / years (at the time of scanning)	Visual Field Defect	Affected side of visual field	Years since stroke	Presence of spatial neglect
11773	F	33	hemianopia	right	5	No
13978	M	73	quadrantanopia	left	1	No
14196	F	60	hemianopia	right	25	No
14326	M	71	quadrantanopia	left	3	No

Brief Description from Participant debriefs

11773: Experienced a stroke in their late 20s. Reported a dense hemianopia in the right visual field. Also reported difficulties with every-day tasks.

13798: Experienced a stroke early August 2018 and after some level of initial spontaneous recovery, was left with distorted vision in the lower left quadrant of the visual field. Reported difficulty in reading the newspaper/books, used a ruler as a guide to help find the next line of text. This is also the only participant who reported rare visual hallucinations in the ‘blind’ field, but only when extremely tired.

14196: Experienced a stroke about 25 years ago. Reports total dense visual loss in the right visual field. Also affected by aphasia.

14326: Experienced a stroke July 2016 and reports visual field loss in lower left quadrant. Was able to regain driver’s licence after follow-up measurements of their visual impairment.

2.3 Vision Tests

A test battery measuring basic visual function and standard ocular health was conducted by a registered optometrist, independent of the university. This included determining (1) existing spectacle prescription, (2) logMAR (Logarithm of the Minimum Angle of Resolution) visual acuity at distance and near, (3) cover test for ocular alignment, (4) ocular motility, (5) refraction, (6) and an assessment of external (slit-lamp biomicroscopy) and internal ocular health (indirect and direct ophthalmoscopy). The test results for each participant can be found in Table 2.2.

Table 2.2: Results of optometric assessment for each participant (both eyes), describing the visual field defect, refractive status, distance visual acuity (VA),near addition and near visual acuity (VA)

Participant	Visual Field Defect	Eye	Refractive Status	Distance VA (logMAR)	Near Addition	Near VA
11773	Hemianopia	R	-3.25	-	-	-
11773	Hemianopia	L	-3.25	-	-	-
13978	Quadrantanopia	R	+1/-0.75 @100	-0.06	2.25	0.6
13978	Quadrantanopia	L	+1.25/-0.5 @62.5	-0.08	2.25	1.0
14196	Hemianopia	R	+2.5/-0.75 @25	-0.10	2.00	0.5
14196	Hemianopia	L	+2.75/-0.25 @175	-0.20	2.25	0.1
14326	Quadrantanopia	R	+1.5/-2.00 @115	0.10	2.50	0.3
14326	Quadrantanopia	L	+1.5/-2.00 @75	0.0	2.50	0.1

2.4 Measuring visual field defect

2.4.1 Static Perimetry

Since the invention of automated perimetry in the 1970s (Johnson et al., 2011; Phelps, 1978), the technique has been commonly used for diagnosing visual field loss, in conditions such as glaucoma (Susanna Jr & Vessani, 2009), age-related macular degeneration (Luu et al., 2013) and notably homonymous hemianopia (Huber, 1992; J. L. Smith, 1962; Zhang et al., 2006a). As it remains the gold standard for objective and clinical visual fields testing, we collected static perimetry data across all participants on both eyes, using a standard automated perimeter (M700 Medmont Automated Perimeter) - operated by a registered optometrist who is independent from the university. Medmount perimetry has been shown to correlate highly with Humphrey perimeters and is established as a reliable test for clinical and research purposes (Landers, 2003).

During field testing, a spatially adaptive probe was used, extending out to 50° of visual angle. This allows an initial test pattern of points to be acquired, with additional points added automatically in the region of any suspect field defect. Because of the adaptive algorithm, the number of samples tested depended on the integrity of the participants' visual field and (for our participants) ranged between 39 and 168 measurement points per eye. For a particular measurement point, the light intensity required was compared with the age normal value for the participant. When the difference was larger than 6 dB, the neighbouring measurement points were automatically added for testing. This method allows for a quick delineation of the visual field using thresholds inside the age normal range (or the edge of the perimeter display).

It is worth noting that although this method allows for a large area of the visual field to be covered quickly, subtle defects (or small areas of residual vision) may be missed between test points. One test run (monocular) took around 8 minutes (longer with increased severity of the visual field loss). For participant 11773, static perimetry was acquired by a different registered optometrist at a different time, using a central 30-2 test on a Humphrey Field Analyzer. Unfortunately, this participant had a subsequent stroke that precluded a re-test under the same conditions as the other participants.

To provide a measure of the defect, the *pattern defect* and *overall defect* for each participant was reported. The *pattern defect* provides a measure of depth of the sensitivity loss and clustering of the defect using spatial correlation. If the defect is distributed randomly across the visual field, the pattern defect will be small; whereas a more localised defect would lead to a higher pattern defect. The *overall defect* provides a measure of the defect standardized to the individual's age range. This is done by measuring the individual's hill of vision (HoV), which is a three dimensional representation that captures the sensitivity to light across the visual field[1]. Then the mean difference between the individual's HoV and the age-normal HoV produces the *overall defect* score. Figure 2.1 shows an example of a field plot with high *pattern defect* and *overall defect*.

The static perimetry data revealed homonymous visual field defects across all four stroke survivors, two with complete right sided hemianopia with no apparent macular sparing (Figure 2.2), two with partial or complete lower left field quadrantanopia (Figure 2.2). Note that participant 14326 (quadrantanopia) shows some macular sparing. Both the estimated pattern defect and mean deviations were consistent across both eyes in all participants, as seen in Table 2.3. Sensitivity measurements across eccentricities - separated between the two hemifields provide a more detailed description of the depth of the defect as seen in Figure 2.3.

---

[1] The name derives from the fact that the spatial pattern reassembles a 'hill' as a sensitivity is higher at the centre compared to the periphery.

Right Eye

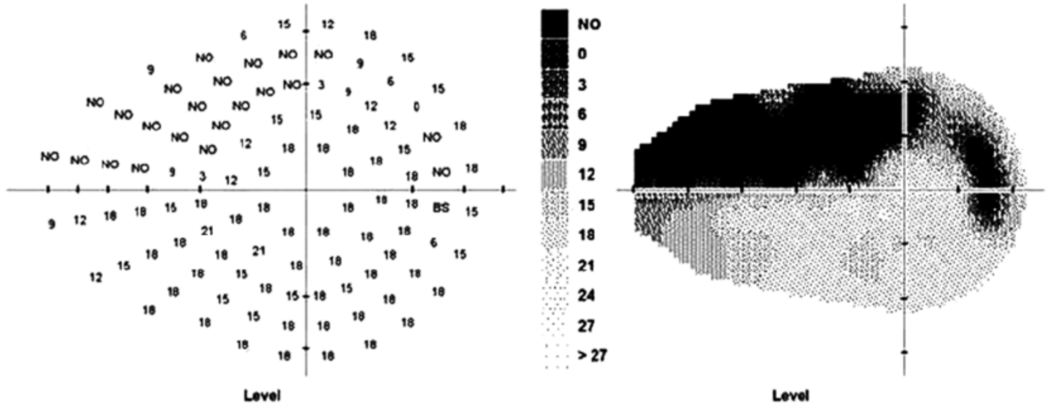

Pattern defect	9.17 ***
Overall Defect	- 5.28***

Figure 2.1: Example of a field plot with high pattern defect and overall defect, taken from Nayak and Dharwadkar (2014). The test was conducted on the right eye using the Glaucoma Test configuration, where sample points are placed within the central 30° field and has an extension to 50° on the nasal horizontal meridian.

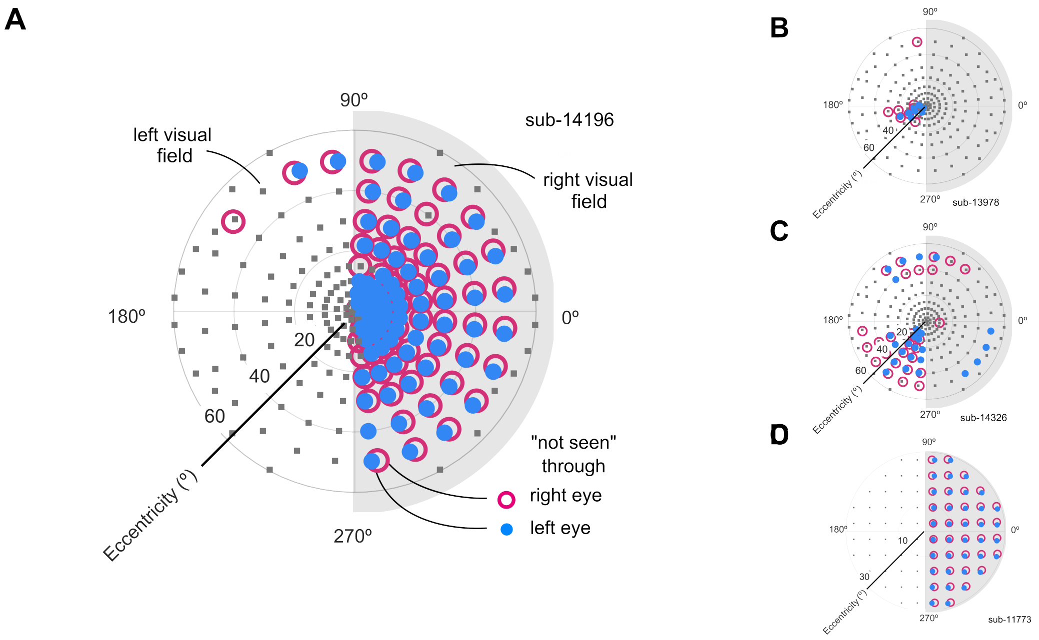

Figure 2.2: Definition of homonymous visual field loss with perimetry for both eyes. (A) Visual field definition by standard perimetry for participant 14196. Test locations (gray squares) were equally spaced across the left and right portion (light gray shading) visual field. Locations at which the participant did not respond to stimuli are shown for both monocular tests (red open symbols, tested through right eye [OD], close blue symbols, tested through left eye [OS]). There is a tight correspondence between the two sets of measurements, indicating a homonymous visual field defect. (B, C, D) Perimetry results for the other participants in our study in the same convention as (A). Note that for participant 11773 perimetry was performed with slightly different parameters and only extended to 30º eccentricity.

Table 2.3: Perimetry results (standard clinical scores).

Participant ID	Visual Field Defect	Pattern Defect		Overall Defect	
		Left Eye	Right Eye	Left Eye	Right Eye
11773	Hemianopia	17.42	18.71	-20.31	-14.59
13978	Quadrantanopia	7.34	9.11	0.04	-0.12
14196	Hemianopia	22.01	21.22	3.89	3.74
14326	Quadrantanopia	12.39	11.02	2.53	2.71

Statistical summary of static perimetry results. The pattern defect is based on spatial correlation, measuring the clustering and depth of the defect. The overall defect, taken as the mean difference between the age normal hill of vision (HoV) and each participant's HoV.

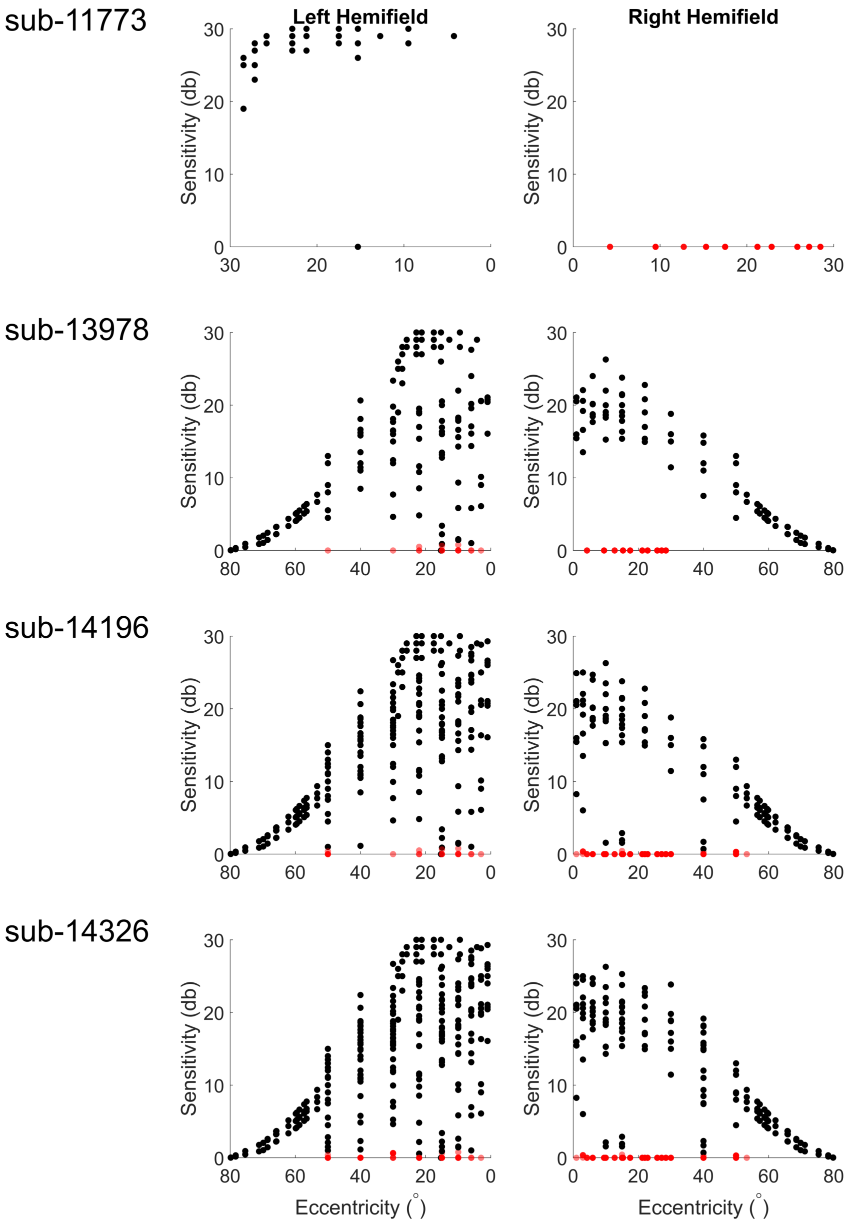

Figure 2.3: Scatter plots show sensitivity (db) as a function of eccentricity (regardless of polar angle) for all test points in perimetry, separately for left and right hemifields. Red symbols represent test points that fall below threshold for vision (adjusted for age) and correspond to points in the scotoma. They are all at 0 dB (and points at the same eccentricity may be overplotted here). Note that perimetry for sub-11773 covered a more central region of test points only.

2.4.2 Kinetic Perimetry

Static perimetry maintains the advantage of detecting small changes in sensitivity with high accuracy, but a sparse test grid is commonly used as a representative sampling of the visual field to avoid long test times, trading off spatial resolution as a result. This means that small scotomas may be unaccounted for if they fall within the spaces of the test points.

In some instances, kinetic perimetry has been used to measure the extent of the visual field defect in HVFD (Hess & Pointer, 1989; Moss et al., 2014; Pambakian et al., 2004). With kinetic perimetry, sensitivity thresholds are determined by moving stimuli of various sizes and light intensity, starting from the 'blind' field towards the 'seeing' field. The patient will indicate the exact moment that they are aware of the stimuli and the examiner will mark the boundary point on a representative map of the visual field. This allows for a fast and efficient procedure to measure sensitivity thresholds across the visual field with higher spatial resolution as compared to static perimetry. Kinetic perimetry also allows for a better measurement of the extent of the visual field deficit as testing points typically begin far out in the periphery. As we were attempting to build a comprehensive characterization of the visual field deficit, we explored options for collecting kinetic perimetry data. However, because kinetic perimetry is rarely used in clinical practice, we were only able to access a manual kinetic perimetry using a Goldmann perimeter as opposed to a semi-automated kinetic perimetry.

Kinetic perimetry results for both eyes were collected on participant 13978, revealing similar results to static perimetry, as seen in Figure 2.4. Although this presents a separate measure of visual perimetry, pilot testing revealed several methodological issues.

The major issue is that manual kinetic perimetry results are highly dependent on the examiner's ability to maintain a constant speed when moving the stimulus across the visual field (Trauzettel-Klosinski & Brendler, 1998b), a slight change in speed may distort the boundaries of the scotoma. There is also no consensus or standard method of conducting kinetic perimetry across clinics, making it difficult to compare across results (Trauzettel-Klosinski & Reinhard, 1998). If the topic of study is investigating the deficit in the peripheral field (functional impairments related to driving and navigating a complex environment), kinetic perimetry would be more advantageous. Because our current study only focused on the central 10° of the visual field, relevant to reading impairments, we concluded that kinetic perimetry did not offer any additional insight into the visual field deficit. We therefore did not include it in subsequent analyses.

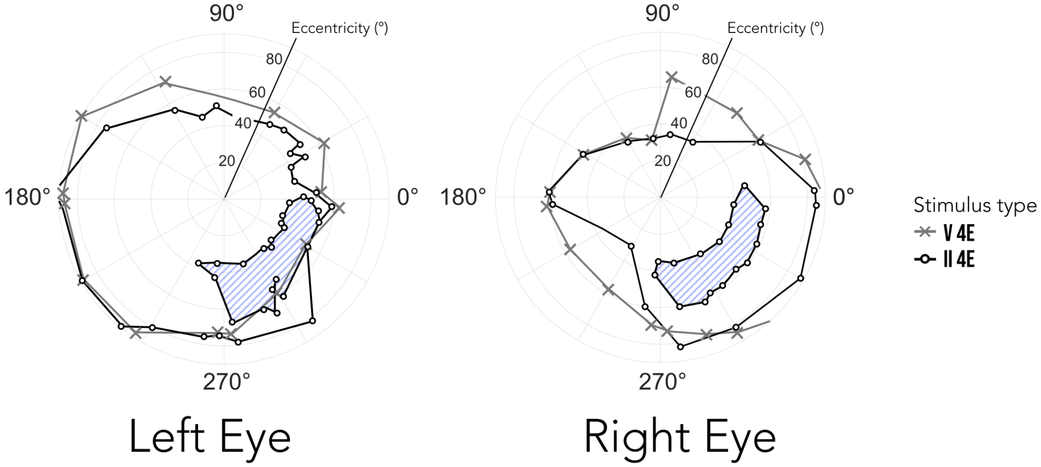

Figure 2.4: Kinetic perimetry results reveal quadrantanopia in the left hemifield for participant 13978. Note that results are flipped across the x-axis due to the setup of the machine. Two stimulus types were used to measure light sensitivity across the visual field, II 4E and V 4E (Roman numeral denotes the Goldmann stimulus size, ie. V, followed by the stimulus intensity, ie. 4E). The blue region indicates a partial visual field deficit.

2.4.3 Microperimetry

We used microperimetry to ensure that our field defect measurements from static perimetry were reliable and repeatable. Microperimetry offers a more stringent assessment of visual field integrity as it is gaze contingent, relocating the stimuli when the eye moves, allowing precise assessment of retinal sensitivities at specific retinal locations. This technique measures retinal sensitivity using the minimum light intensity that patients can perceive when small increments in luminance are used to stimulate discrete locations on the retina. Retinal sensitivity estimates for a particular test point also have a high spatial accuracy of up to half a degree (Markowitz & Reyes, 2013), providing a more accurate measure of the borders of the scotoma. Microperimetry also affords an accurate measure of fixation stability. Fixations are continuously recorded throughout the test and fixation stability estimated using a metric called the Bivariate Contour Ellipse Area (BCEA) (Markowitz & Reyes, 2013; Steinman, 1965), which is widely used to report fixation stability (Crossland et al., 2004).

Microperimetry data were collected separately for each eye using a MAIA-2 (iCare, Finland) device. The MAIA has been widely used for clinical trials and diagnosis, with robust repeatability, reliability and intersession agreement (Charng et al., 2020; Chew et al., 2019; Molina-Martín et al., 2016; Roh et al., 2019; Wong et al., 2017). The measurements were performed with a natural pupil in a dim room. Sensitivity was measured using the full threshold 4-2 expert test, with a custom grid of 41 points covering the central 20° of visual angle. For participant 11773 we used a 37-point stimulus grid which spans 10° instead, but as noted elsewhere, a subsequent stroke in this participant prevented us from acquiring visual field maps with exactly matched sampling points. Test locations were spaced at 2° over the central 10° of the visual field. The stimulus size was Goldmann III, background luminance was 4 asb (or 1.27 cd/m^2) and maximum luminance was 1000 asb (318.3 cd/m^2) with a 36 dB dynamic range. A red circle, with a size of 1°, was used as a fixation target. The BCEA was calculated using an ellipse area that contained 63% of fixation points.

Microperimetry measurements across 4 stroke survivors can be seen in Figure 2.5. The results showed a consistent pattern of the visual field defect similar to static perimetry. Three of the four participants had excellent fixation stability: participants 11773, 14196 and 14326 showed relatively small BCEA values, ranging from $0.4^{\circ 2}$ - $1.7^{\circ 2}$, whereas participant 13978 had a large BCEA (left eye: $17.9^{\circ 2}$, right eye: $26.9^{\circ 2}$) indicating more unstable fixation. For reference, BCEA estimates in healthy participants were previously found to be on average $0.80^{\circ 2}$ (min = 0.03, max = 3.90, SD = 0.68) (Morales et al., 2016).

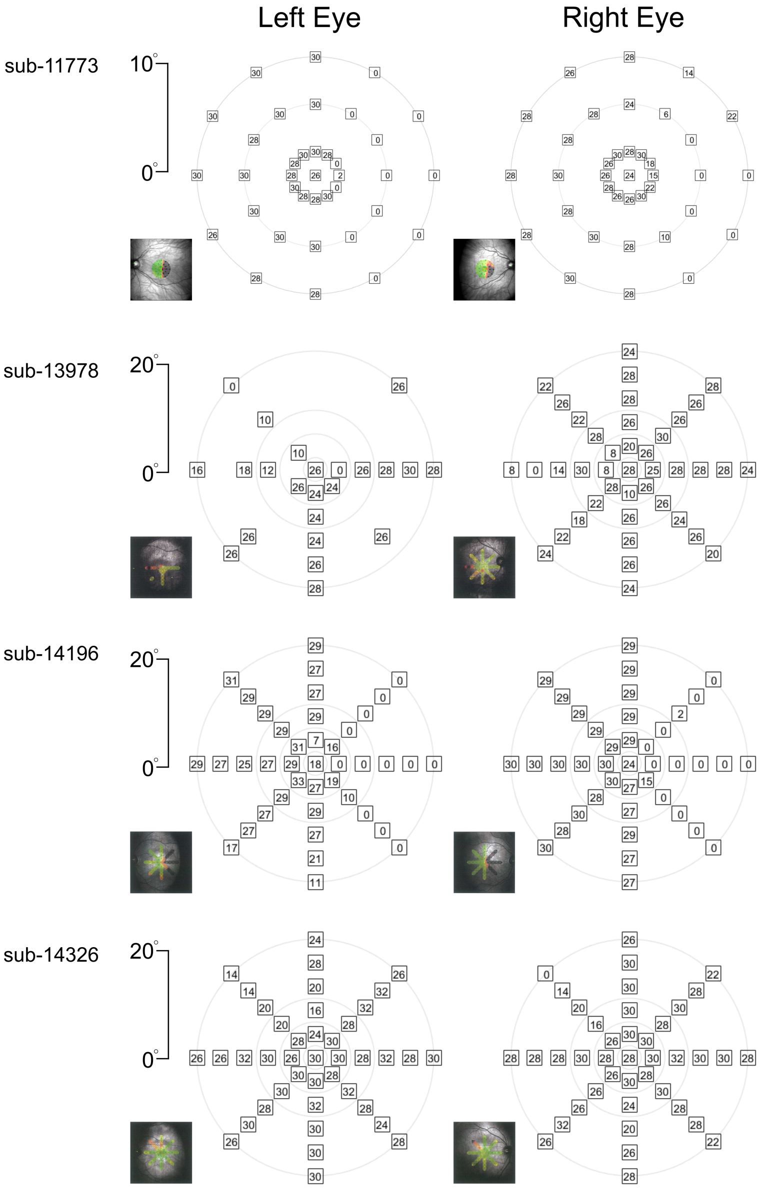

Figure 2.5: Microperimetry measurements across 4 stroke survivors. The measurements across the sample points represent the retinal sensitivity (db). All stroke survivors were measured using a 41-point stimulus grid which spans 20° with the exception of participant 11773 which uses a 37-point stimulus grid which spans 10°. Note that for participant 13978, fixation stability was an issue. Even with gaze-contingent microperimetry, acquiring robust data was challenging. For participant 14326, robust macular sparing was apparent in both standard and microperimetry.

2.5 Spatial Neglect

One potential confound of measuring vision loss is spatial neglect. Unilateral spatial neglect (USN) is a condition where attention is impaired in one side of space from the individual's point of view. It is commonly associated with stroke and is caused by damage to the parietal lobe (Shinoura et al., 2009; Vuilleumier, 2013). Spatial neglect manifests itself by a failure of participants to respond to stimuli in the contralesional side. USN is often mistaken or misdiagnosed as homonymous hemianopia, as patients fail to detect the stimulus while maintaining fixation during a standard perimetry test (Walker et al., 1991). Although the symptoms are similar, patients with USN only fail to detect or respond to the stimuli but their visual fields are typically unaffected.

However it should be noted that in some cases, stroke survivors could have both HVFD and unilateral spatial neglect (Girotti et al., 1983; Karnath & Hartje, 1987; Saj et al., 2010). It is important to disentangle both HVFD and USN as the impairments although symptomatically similar, are fundamentally different, showing different patterns of functional imaging responses (Watanabe et al., 2006) and require separate intervention strategies (Gammeri et al., 2020).

In the study, it was assessed that participant passed the conventional sub-test of the behavioural inattention test, BIT C (Halligan et al., 1991), which consists of 6 assessments: Line Crossing test, Letter Cancellation test, Star Cancellation test, Figure and Shape Copying test, Line Bisection test, Representational Drawing test. This set is commonly used to show an absence of spatial neglect and is able to differentiate between patients with both HVFD and USN against USN alone (Halligan et al., 1990). All stroke survivors recruited for this study passed the BIT C and did not show any signs of spatial neglect.

2.6 Fixation Stability

Because our brain mapping protocol relied on standard retinotopy stimuli to map visual field responses in the brain (see Chapter 3 & 4 for more details), it was vital that participants were able to maintain stable gaze fixation throughout the scanning session. Hence, all participants were trained with the stimulus presentation prior to the scanning session to ensure that they understood the requirements of the task. Briefly, the task involved responding to the colour change in the fixation cross placed in the centre of the screen.

While performing this task, a set of dynamic high contrast stimuli moved across the screen in various configurations (see Chapter 3) which participants were told to ignore and only fixate on the fixation cross. Participants repeated the training until stable gaze fixation was achieved. Figure 2.6 shows an example of successful stable gaze fixation during the mock session.

We initially piloted the use of an eye tracking system while scanning, which is a more reliable way of ensuring data quality and allows for gaze correction. However, this proved difficult to set up with patients as the reliability of the eye tracker signal for detecting the participant's pupil varied substantially, both across participants as well as throughout each test session. In our setup, this was mainly due to the constraints of the mirror assembly in the scanner, the distance of the BOLD screen to the scanner and most notably the position of the participant's eye level within the head coil. As participants were required to position their heads for optimal coverage in the head coil, there was limited flexibility to angle their head (pitch) and obtain eye positions for the eye tracker to reliably record eye movements. Although we have had some success in recording eye movements throughout the entire scan session (in our pilot runs), we decided to omit this step during our scanning protocol with stroke survivors in favour of patient comfort and acquiring data with the other imaging modalities. Hence, we relied on the two separate measures to ensure fixation stability, (i) recording eye movements in the out-of-scanner mock session with the same stimulus, (ii) the BCEA score from microperimetry.

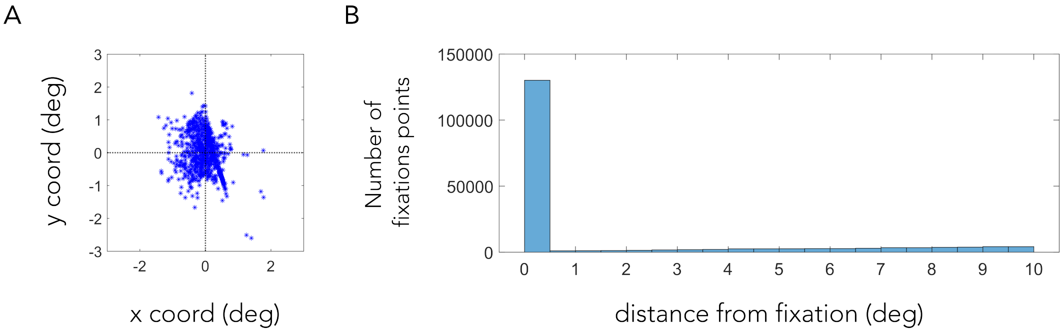

Figure 2.6: Example of successful stable gaze fixation during the mock session. (A) Scatter plot of fixation points throughout the mock session. (B) Histogram of distance of fixation points from centre.

Chapter 3

Brain imaging pipeline

3.1 Overview

It is important to establish a pipeline for scanning that maximises the amount of useful data about the lesion (gray matter and white matter) and visual field loss (function) within a relatively short time frame. As the ultimate goal is to develop a rehabilitation program that is accessible for stroke survivors with sight loss, the scanning pipeline has to overcome some practical constraints. I was aiming to build a multi-modal approach which required multiple imaging protocols that (if done inefficiently) could take a long time. In most cases, it is not realistic to scan stroke survivors for long hours as they are typically older and generally do not feel comfortable staying in the scanner for too long. Moreover, early pilot studies in our lab indicated that scans towards the end of the session suffered more from participant motion in the scanner and failure to fixate to the centre of the screen, resulting in noisier imaging data.

After some pilot testing, we converged on a pipeline that included acquisition of *T1-weighted*, *T2-weighted anatomical images*, *T2*-weighted (BOLD) images*, a B_0 *map* and *diffusion weighted images* that did not go beyond 90 minutes including setup. We found this to be a good balance between collecting meaningful imaging data without sacrificing data quality and patient comfort.

This chapter will discuss the details of the scanning pipeline used in this project, including the stimulus presentation, imaging protocol and preprocessing steps.

3.2 Stimulus Presentation

To elicit robust visual responses in the brain, we presented stimuli commonly used in standard retinotopy mapping studies, also known as phase-encoded retinotopy (DeYoe et al., 1996; Dumoulin et al., 2003; Dumoulin & Wandell, 2008). We used the implementation in a custom software, MGL (Gardner et al., 2018) to present sets of rotating wedges, expanding/contracting rings and moving bars of high-contrast, moving checkerboard stimuli, as seen in Figure 3.1. These stimuli are designed to activate cortical regions representing specific locations of the visual field in a systematic temporal order. Information from the functional magnetic resonance imaging (fMRI) signal can then be used to reconstruct — for each voxel — the visual field locations that drive its fMRI response. Participants viewed the stimuli on a BOLDscreen32 (CRS Ltd., Rochester, Kent) at the back of the bore through a mirror mounted on the head coil. The viewing distance to the screen was 119 cm, the screen resolution is 1440 × 1080 pixels with a refresh rate of 100 Hz. The screen spans out to +/- 6 degrees of visual angle vertically and out to +/- 8 degrees of visual angle horizontally.

The first stimulus is a bar stimulus that swept across the screen in 3 separate directions: horizontally, vertically and diagonally. As this bar aperture swept across the mean luminance grey background across the screen (total period per sweep, 24s), it revealed the high-contrast checkerboard pattern (where black and white elements drifted at 7.5° per second). Each block consisted of 5 such (sweeps) cycles and two repeated scans were acquired, one with time-reversed order of sweep directions for each bar movement type (horizontal, vertical and diagonal). The decision to opt for shorter scans and multiple repeats was deliberate, as we wanted to minimize potential data loss if a scan had to be discarded or if a participant's attention tended to drop off significantly during longer scans (e.g. potentially falling asleep or fixating away from the centre). Additionally, removing as much of the unwanted variability in data acquisition should increase the signal-to-noise ratio in our data.

The second type of stimulus was a 'wedge' stimulus (a 90° sector of a circle) which periodically rotates around the screen, in either a clockwise or counterclockwise direction for the duration of a scan. The third type of stimulus was a 'ring' stimulus (an annulus) which expanded or contracted in eccentricity (minimum radius of 0.5° and maximum radius of 11.25°). The number of cycles per scan and scan repeats were kept the same as for the bar stimulus.

To help participants maintain fixation and attention during stimulus presentation, we used a simple fixation dimming task (two-interval forced choice): participants had to indicate by button press, which of two intervals contained a darker fixation cross. Difficulty of the task was adjusted by changing the brightness difference of the fixation cross between the intervals in line with a 2-down, 1-up staircase. Participants were trained with the stimulus presentation prior to the scanning session (see Chapter 2 for more details) to ensure that they understood the requirements of the task (maintain gaze stability and respond to the color change of the fixation cross).

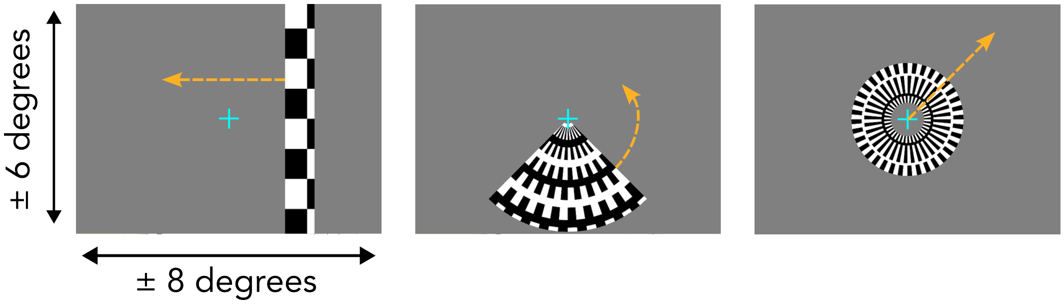

Figure 3.1: Example of the stimuli presented in the scanner. The stimuli involves a high-contrast moving checkerboard pattern with several different configurations; a moving bar (left), a rotating wedge (middle), and an expanding/contracting ring (right). The fixation cross periodically changed in brightness between intervals and participants were instructed to indicate which interval was darker in a two-interval forced choice task. The screen spans 6 degrees of visual angle in height and 8 degrees of visual angle in width.

3.3 Participants

Participants were required to read through the information sheet and a consent form, which detailed scanner safety protocols and the potential risks involved. They were asked to complete both a consent form (ethics) and a safety screening form (issued by the Sir Peter Mansfield Imaging centre) before entering the scanner. Because it is common for stroke survivors to have undergone prior surgeries before participating in further research studies, it was particularly important to establish that they did not have any implants or medical devices that could pose an MR safety risk. During MR data acquisition, participants were in a head-first, supine position and viewed the display through an angled one-mirror setup. Participants were debriefed after the scanning and because they had expressed a keen interest in knowing more about the functional imaging results, were also provided with a copy of some preliminary analysis results (from the retinotopy) in a information “test” pack. The preliminary nature of those results were explained clearly.

3.4 Imaging Protocol

Magnetic resonance imaging (MRI) data were acquired using a 32-channel head coil on a 3T Phillips Achieva MR system at the Sir Peter Mansfield Imaging Centre (Nottingham, United Kingdom). In our scanning protocol, we acquired anatomical scans, functional scans and diffusion weighted data.

3.4.1 Anatomical scans

Anatomical scans were acquired via two imaging protocols: T1-weighted images and T2-weighted images. The T1-weighted and T2-weighted images are commonly used in clinical practices to visualise the brain anatomy and assess for any pathologies. T1-weighted scans are based on the longitudinal relaxation of a tissue's net magnetisation vector (Huettel et al., 2004). The different contrasts in the scans are a result of tissue types taking varying time to realign to the external magnetic field (B_0). Fat has a different T1 time constant to water which results in it appearing of a different brightness in the reconstructed images, depending on the exact choice of imaging parameters. T2-weighted scans conversely reflect the loss of phase coherence in the transverse plans. T2 contrast imaging generally uses a longer repetition and echo time (TR and TE) to minimize any T1 relaxation effects. With T2 scans, water usually appears 'brighter' and fat appears 'darker'. Due to these properties, T1 scans which emphasize differences in gray and white matter are suitable for characterising brain anatomy (white matter) while T2 scans often help with detailing any underlying pathologies (damaged tissues tend to develop edemas which have increased water content). These two protocols allow us to comprehensively capture the extent of the lesion or any existing pathologies in the post-stroke brain.

Anatomical scans were acquired using a 3D magnetization-prepared rapid gradient echo (MPRAGE) sequence, which provides high tissue contrast and spatial resolution in a short time frame (J. Wang et al., 2014). The T1-weighted images were acquired using a sensitivity-encoded (SENSE) factor of 3 with an echo time (TE) of 3.7 ms, a repetition time (TR) of 8.13 ms, a flip angle of 8° with a field-of-view (FOV) of 160 x 256 x 256 mm3. To aid visualisation of lesions, we also acquired T2-weighted images with high inplane resolution (axial, 0.45 mm inplane voxel size, 3 mm slice thickness, 1 mm gap. The parameters for those scans were TE: 88.9 ms, TR: 3,381 ms and flip angle: 90°, resulting in images with a matrix size of $512 \times 512 \times 36$.

3.4.2 Diffusion-weighted imaging (DWI)

Diffusion-weighted imaging (DWI) is an MR-based acquisition method which provides a measure of the diffusivity of water, via the attenuation of T2 signal loss caused by random thermal movements of molecules in water – Brownian motion. In brain regions where water has a high degree of random motion - high diffusivity, such as the cerebrospinal fluid (CSF), this leads to higher spin dephasing and hence larger signal loss. However in regions with less diffusivity, such as grey matter or more importantly white matter tracts, there will be less signal loss. The details of diffusion weighted imaging sequences are beyond the scope of this chapter, but for a more in depth review, see Huisman (2010).

By applying sensitising gradients in different directions, DWI is able to capture the directionality and shape of water across brain structures: this version of diffusion weighted imaging is often referred to as diffusion tensor imaging (DTI). By fitting a diffusion tensor (ellipsoid shape) to the diffusions profile at each voxel, measures that are thought to reflect microstructural properties can be inferred. The fractional anisotropy (FA), how strongly directional the diffusion pattern is, is an example of such a measure and can be seen in Figure 3.2. FA values range between 0 – reflecting a perfectly spherical (isotropic) diffusion profile and 1 – reflecting a maximally anisotropic pattern, a long cylinder with a small diameter. The orientation and shape of the ellipsoid corresponding to the diffusion tensor also provides information on the directionality of the main directions of diffusivity (vectors in 3d space). In healthy, normal white matter tracts, water tends to diffuse primarily parallel to the long axis of the tract with little in the perpendicular direction. Hence, FA provides an indirect measure of the white matter integrity; healthy tracts will have higher FA scores compared to damaged tracts. This along with the directionality of the surviving tracts will assist in building a comprehensive profile of the damage to the visual pathway (and potential mechanism behind any residual vision).

Diffusion weighted data were acquired at 2 mm isotropic resolution, using a single-shot, echo-planar sequence with a TE of 57 ms and TR of 8,217 ms. Diffusion weighting was applied in 60 directions for b = 1000 s/mm^2 and one volume was acquired for b = 0 s/mm^2 (b-value determines the measurement sensitivity of diffusion and changes the contrast across regions, for examples of scans at different b-values, see Graessner (2011)). As the changing magnetic field in the MRI causes eddy currents which result in artefacts in the images, we acquired two calibration images with reversed phase-encoding directions. This is to allow for distortion correction using FSL's topup (Andersson et al., 2003; S. M. Smith et al., 2004), which infers the underlying field inhomogeneities by combining information from images acquired under the two regimes with opposite polarities. The fieldmaps inferred with this methods could then be used to counter distortions in acquired data.

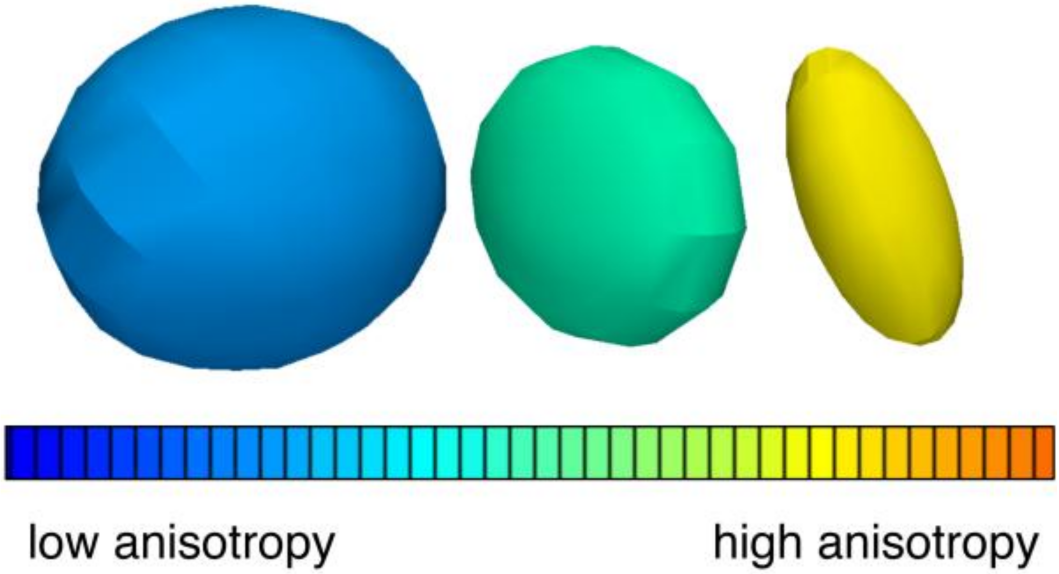

Figure 3.2: Visualization of three diffusion tensors shapes illustrating different levels of fractional anisotropy along with orientation, taken from O'Donnell and Westin (2011).

3.4.3 Functional scans

To measure functional responses in the brain using MRI, we used the blood-oxygenation-level-dependent (BOLD) contrast, which acts as an indirect measure of neural activity. The BOLD contrast is sensitive to the regional concentration of deoxyhemoglobin (Ogawa et al., 1990) and a positive BOLD signal reflects a localised decrease in deoxygenated blood. There is a cascade of events following an increase in neural activity, which ultimately also lead to a change in cerebral blood flow (CBF) and blood volume (CBV). The process that links changes in neural activity and resulting haemodynamic changes is known as neurovascular coupling.

Briefly, an increase in localised neural activity with a concomitant increase in metabolic demand leads to a brief increase in the proportion of deoxyhaemoglobin, which is only present briefly and may reflect an "initial dip" in the haemodynamic response. Following this, however, there is a much larger increase in the proportion of oxyhaemoglobin, which results in a decrease in local field inhomogeneities, and therefore a longer T2* time constant, which manifests itself as increased signal amplitudes compared to baseline at the same echo time (TE). This change in BOLD signal (across time and space) is captured by the so-called hemodynamic response function: often described as a delaying and blurring of the neural response in time but also captures the spatial extent of the BOLD signal corresponding to localised neural activity. Importantly, the spatiotemporal properties of this signal indirectly reflect neural activity and allow us to measure functional responses of the brain robustly and with millimetre spatial precision, albeit at the cost of some delay in time. For a more detailed review of this process, refer to Logothetis
(2003).

In our study, functional MRI data were acquired with a close to axial slice prescription which covered most of the head from frontal to occipital cortex, maximising the coverage over the important brain regions. Our protocol used 2D gradient echo EPI, a commonly used pulse sequence with high temporal resolution, able to rapidly acquire a 2D images quickly by switching the magnetic gradients back and forth after a single radiofrequency pulse (J. Chen & Cohen-Adad, 2019; Hennel, 1997; Mansfield, 1977). The images were acquired using moderate SENSE acceleration factor of 2 and a short TE of 35ms, which allowed for a good combination of temporal resolution, reliable image quality by suppressing susceptibility artefacts, and good BOLD sensitivity (Schmidt et al., 2005; Weiger et al., 2002). 24 slices were acquired at 3mm isotropic resolution with a TR of 1500ms. The flip angle was set to 75°, matched closely to the Ernst angle (Ernst & Anderson, 1966).

3.5 General Preprocessing Steps

Imaging data were analysed using a combination of FSL (Jenkinson et al., 2012) and custom written software, mrTools (Gardner et al., 2018), running in Matlab R2016b (MathWorks, 2016). FMRI data were corrected for motion (Nestares & Heeger, 2000) within and across scans using tricubic interpolation. Each fMRI scan was also linearly detrended and temporally high-pass filtered with a cut-off frequency of 0.01 Hz to remove signal drift (A. M. Smith et al., 1999). The first 8 frames of each functional scan were discarded to avoid transient changes at the beginning of scans.

Initially, the gray and white matter segmentation was carried out using FreeSurfer v6.0 (http://freesurfer.net/fswiki/FreeSurferWiki, Fischl (2012)). The T1-weighted images for all subjects were processed using the command '*recon-all*', including all alignment, segmentation and labelling steps. The command '*recon-all*' performs all of the FreeSurfer preprocessing steps using the T1-weighted anatomical images. Models of the boundary between white matter and cortical gray matter as well as the pial surface are constructed from a template and then refined based on the participant-specific anatomical image. In one processing step, the cortical surface is reconstructed into a mesh of vertices that allows further analysis and use for visualisation of data on the cortical surface. We found, however, that FreeSurfer segmentations were adversely affected by stroke lesions, even when lesion masks were used to constrain the reconstruction.

To address this, we used an approach that relies less on reconstruction of cortical surfaces, but more on information from a probabilistic atlas and volume-based analysis methods. Chapter 5 will address this issue in further detail. The preprocessing for diffusion data will also be discussed later in Chapter 5.

Chapter 4

Mapping Functional Responses

4.1 Overview

To be able to exploit residual visual function for rehabilitative purposes, it is important to identify the presence of any surviving cortex in stroke survivors that still respond to visual stimuli in the blind field. Ideally this process should be relatively quick, efficient and data-driven. This chapter will cover the methodology we used for analysing the functional scans acquired from stroke survivors with homonymous visual field deficits (HVFD). A visual summary of this pipeline can be seen in Figure 4.1. The detailed results from the analysis will be presented in the subsequent chapter, Chapter 6.

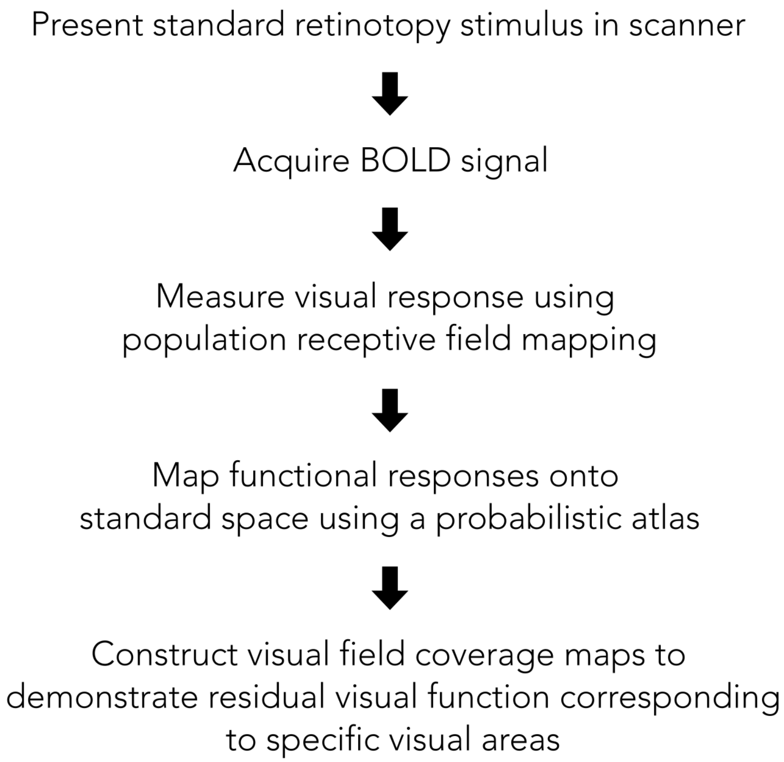

Figure 4.1: Pipeline for mapping residual visual function in stroke survivors using functional magnetic resonance imaging (fMRI).

4.2 Retinotopic maps

Many visually responsive areas in the brain are retinotopically organised (DeYoe et al., 1996). This 1-to-1 mapping between visual (retinal) space and locations on the cortical surface allows us to derive which visual field locations drive the responses in each voxel by combining the data acquired from the phase-encoded retinotopic stimuli.

The standard analysis of retinotopy often follows these steps: first, times series data across stimulus runs for both directions are averaged (ie, ring: contracting & expanding, wedges: clockwise & counterclockwise) by time-shifting both scans and time-reversing one. The idea of this step is that any residual haemodynamic lag is cancelled out because they are equal and opposite in those two scans. This then accounts for the hemodynamic lag of the BOLD signal. As the stimuli systematically sweeps across the screen, the times series data for each voxel with a limited "receptive field" responding to visual stimuli should reflect a periodic pattern, which often appears close to sinusoidal (but whose shape depends on the duty cycle of the stimulus and the "receptive field" of the voxel).

Next, a correlation analysis is performed by considering the signal in the Fourier domain. The power of the time series signal at the frequency of the stimulus and the signal's phase at that frequency provide important information. We can use the *phase* to infer the timing - and therefore spatial placement - of the stimulus that drove responses in that voxel. The correlation measures with the stimulus frequency and the *amplitude* of the signal provide a measure of signal reliability and amount of relative BOLD response, respectively. The correlation (sometimes called *coherence* value), can be used to filter for reliable voxels. Figure 4.2 shows an example of a correlation analysis on a single voxel with a high coherence value and large percent signal amplitude, indicating a very clear cortical response to the visual stimulus.

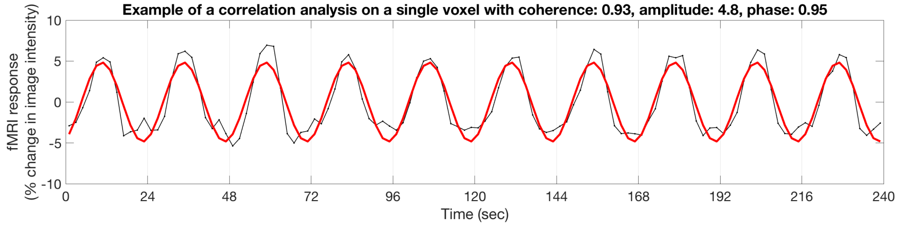

Figure 4.2: Example of a correlation analysis on a single voxel with a high coherence value. The black line is the measured time series data while the red line represents the model fit of the harmonic function. As the coherence is high, the signal is assumed to be reliable and provide information about the phase in which the voxel is sensitive to. The phase corresponds to either polar angle (wedge scans) or the eccentricity (ring scans).

The time series analysis is performed for every voxel in the dataset and the resulting correlation, phase and amplitude statistics are often displayed as false colour maps, superimposed on anatomical images. Figure 4.3 shows the results of the correlation analysis for the ring and wedge scans for participant 11773. These results show an eccentricity and polar angle map of the visual field. The BOLD signal is superimposed on a high resolution anatomical scan. Alignment between the BOLD data and anatomical images was done using mrAlign (Nestares & Heeger, 2000) to provide a clearer visualization of the functional response with respect to anatomical landmarks.

Participant 11773 had a complete right hemifield hemianopia as result of a lesion in the left visual cortex. Although perimetry results (refer to Chapter 2) confirmed the hemianopic field loss, the retinotopy results across both ring and wedge scans can be seen to produce a residual visual response (though with less coverage compared to the healthy right hemisphere). This can also be seen in Figure 4.4, where we overlaid the results on an inflated surface of the lesioned hemisphere (left hemisphere) for a better view.

Typically, the results from retinotopy analyses are then used to segment different visual areas using the polar map representation acquired with the wedge scans (Wandell et al., 2007). An example of this can be seen in a flat map of the right hemisphere (healthy hemisphere) of participant 11773 in Figure 4.5. A flat map is constructed using the mesh of vertices acquired from segmentation of the grey matter, white matter and pial surface during the preprocessing step. In this representation vertices are connected to other vertices and 3 connected vertices form a triangular face. The vertices and faces form a two-dimensional surface that is embedded in three dimensions. This methodology allows us to ‘flatten’ the mesh and have a look at the data in a more easily understandable visual format.

However, in cortical hemispheres affected by stroke, incomplete visual responses across the polar angle maps make it difficult to outline and define visual areas as the common landmarks are difficult to identify or locate. The initial step of outlining the visual areas usually starts by identifying V1, which is located in the calcarine sulcus; however, as seen in the flatmaps in Figure 4.5, there are no visual responses in that region. To identify the visual areas in which residual visual function was found, we therefore took a different approach, which is addressed in a later section of the chapter.

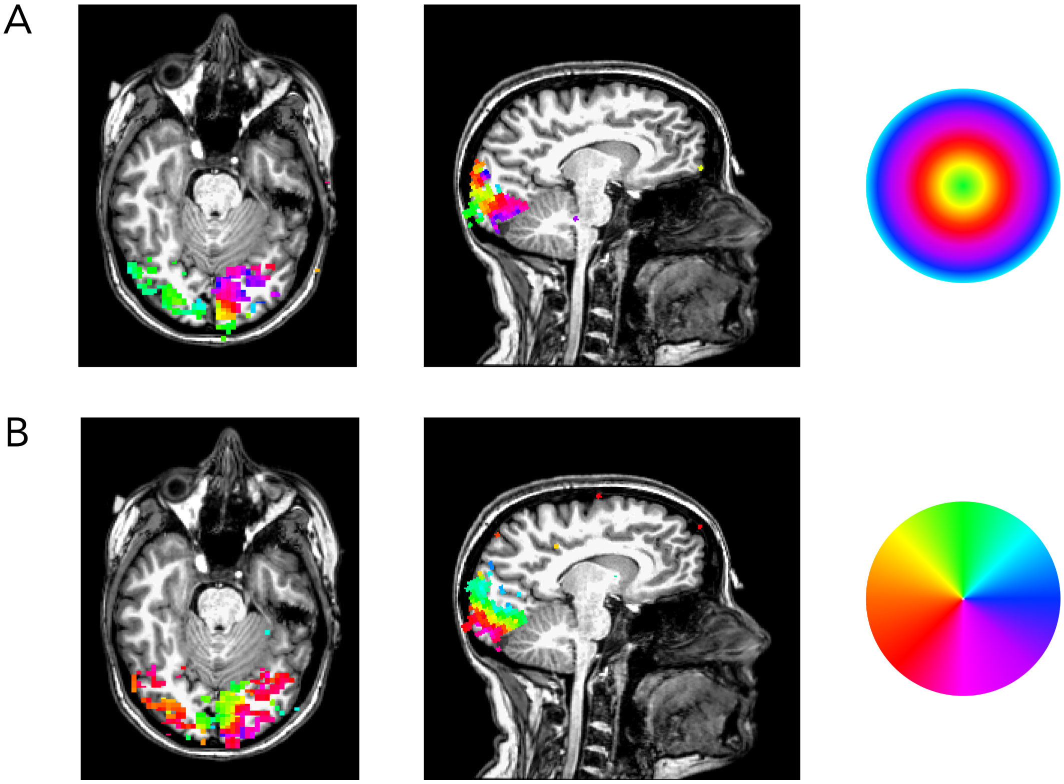

Figure 4.3: Correlation analysis results for both ring (A) and wedge (B) scans in both axial and sagittal view for participant 11773. Participant 11773 has a complete right hemifield hemianopia so the healthy reference for comparisons would be the right hemisphere (depicted in the right side in axial view). The results are overlaid on a high resolution T1-image registered with the BOLD data. A coherence threshold of 0.4 was used to filter out noisy voxels. The colors represent the phase values of each respective scan (A: eccentricity, B:polar angle). For the ring scans (A) we can see a radial pattern emerge starting from the occipital pole, reflecting visual response to different levels of eccentricity. For the wedge scans (B), the color shift in 'wedge' like patterns as it travels longitudinally across the visual cortex, reflecting the change in polar angle.

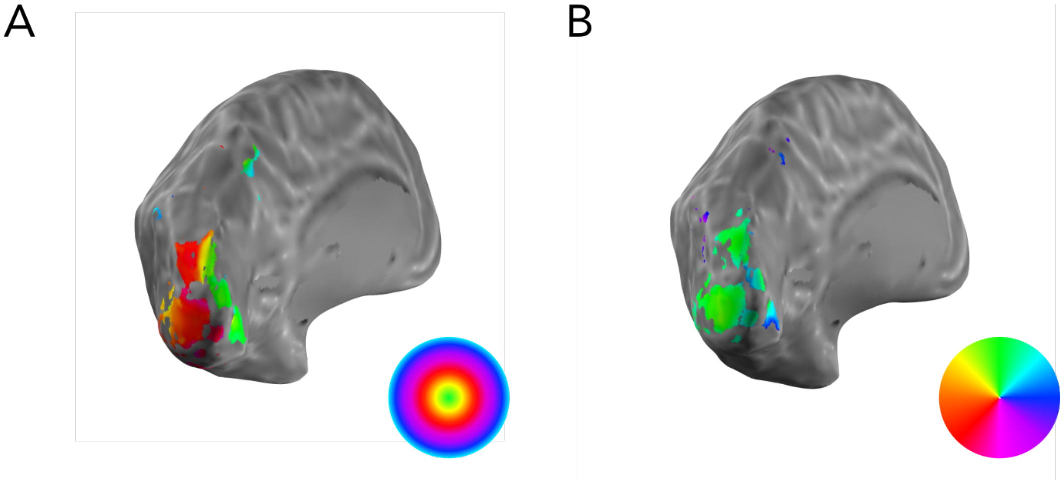

Figure 4.4: Correlation analysis results for ring (A) and wedge (B) scans for participant 11773, overlaid on an inflated surface of the lesioned hemisphere (left hemisphere).

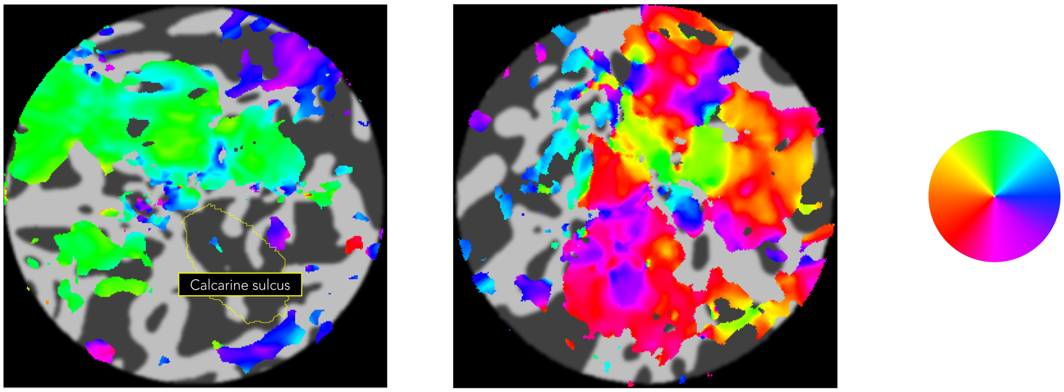

Left hemisphere
(lesioned hemisphere)

Right hemisphere
(healthy hemisphere)

Figure 4.5: Flat maps of both lesioned (left) and healthy (right) hemispheres of participant 11773. This is the polar map representation from the wedge scan, which allows us to define visual areas by looking at ‘reversals’. As we move away from V1 (either in the dorsal or ventral direction) into higher visual areas (V2, V3), we can observe a phase reversal where the visual field representation ends at the upper/lower vertical meridian (ventral: green to yellow, dorsal: red to pink). This is largely observable in the healthy hemisphere (right) although there seems to be some ipsilateral visual field representation. However for the lesioned hemisphere (left) no obvious phase reversals can be observed due to the lack of visual response from some regions. Alternative methods include using an initial landmark to guide delineation of the visual regions, but this was also not possible (no visual representation near the calcarine sulcus).

4.3 Population Receptive Field Mapping

Classic retinotopic maps provide a good overview of the retinotopic organisation in the visual areas and their corresponding visual field location, highlighting any abnormalities or visual field losses. However, standard Fourier-based methods only provide voxel-wise information about the visual field locations that are best at eliciting a response (using the polar angle and eccentricity measures, and associated amplitude and correlations). The method cannot take into account the receptive field coverage of the underlying neuronal population at a particular voxel.

Population receptive field (pRF) analysis – a technique developed by Dumoulin and Wandell (2008), addresses these issues by using a simple linear model to estimate not only the optimal visual field location, but also other aspects such as the extent (size) of the population receptive field. The initial model has also been extended to estimate surround suppression (Zuiderbaan et al., 2012), contrast normalization, and other features of the cortical response to visual stimuli (Aqil et al., 2020).

The underlying idea of the pRF approach is that a particular voxel (in our case the size of $3mm^3$) reflects the responses of many neurons and therefore corresponds to a range of visual field locations covering an extended area of the visual field. The receptive fields of individual neurons also vary in size across visual areas; receptive field sizes are observed to be larger as we move from primary visual cortex (V1) to V2, V3 and V4

(A. Smith et al., 2001; Tootell et al., 1997).

4.3.1 Constructing the model

The pRF model is constructed by using a 2D circularly symmetric Gaussian to describe the population receptive field to each voxel. Together with a description of how the stimulus evolved over space and time, this can be used to predict the fMRI times series signal. The Gaussian model represents the combined receptive field of the population of neurons that result in the BOLD time series response observed in a voxel. In our version, it is defined by three parameters x_0, y_0 and σ, where [x_0, y_0] represent the centre of the Gaussian pRF and σ represents the standard deviation (spatial spread), as seen in the following formula:

$$(x, y) = \exp -\left(\frac{(x - x_0)^2 + (y - y_0)^2)}{2\sigma^2}\right)$$

The original Gaussian model introduced by Dumoulin and Wandell (2008) uses a circularly symmetric shape defined by these 3 parameters, but other labs have experimented with allowing other shapes, such as an elliptical using two parameters, σ_1 and σ_2 to define the long and short axis of the elliptical shape. (The circularly symmetric RFs can be thought of as a special case, where $\sigma_1 = \sigma_2$, both axis are equal and the shape is circular). Although there is some evidence that the elliptical shape is able to better capture the differential neuronal population across visual areas (Merkel et al., 2018, 2020; Silson et al., 2018), replications of these implementation found that the best model fit was not very different from the original circular shape (Greene et al., 2014; Lerma-Usabiaga et al., 2021; Zeidman et al., 2018). For parsimony, we therefore opted for the circular Gaussian model for our analysis.

We then define the effective stimulus as $s(x, y, t)$, representing the aperture that sweeps across the screen and reveals the checkerboard pattern in various configurations. The *predicted pRF response* is first calculated by using the multiplication of the Gaussian pRF and effective stimulus at each time point, as seen below:

$$r(t) = \sum_{x,y} s(x, y, t)g(x, y)$$

To account for the temporal delay and haemodynamics, this response is then convolved with the standard hemodynamic response function (HRF, $h(t)$) (Boynton et al., 1996; Friston et al., 1998) to acquire the predicted BOLD response:

$$p(t) = r(t) * h(t)$$

A visualization of how we arrive at the predicted pRF response for a single voxel can be seen in Figure 4.6. For each voxel in our retinotopy

scans, we used the measured time series and predicted BOLD response to compute the best-fit parameters [x_0, y_0, σ] using non-linear least-squares. This is done by minimizing the residual sum of squares (RSS) between the predicted BOLD response and measured BOLD response, where β is a scale factor to account for the arbitrary units in the fMRI
signal:

$$RSS = \sum_t (y(t) - p(t)\beta)^2$$

This process is then repeated for each voxel to find the best fit parameters of the pRF x_0, y_0 and σ. Figure 4.7 shows an example of a good fit between the predicted BOLD response and the measured times series, providing information about the size and location of the population receptive field of a particular voxel. A visualization of how this voxel is represented in visual space can be seen in Figure 4.8, using the pRF estimates [x_0, y_0, σ].

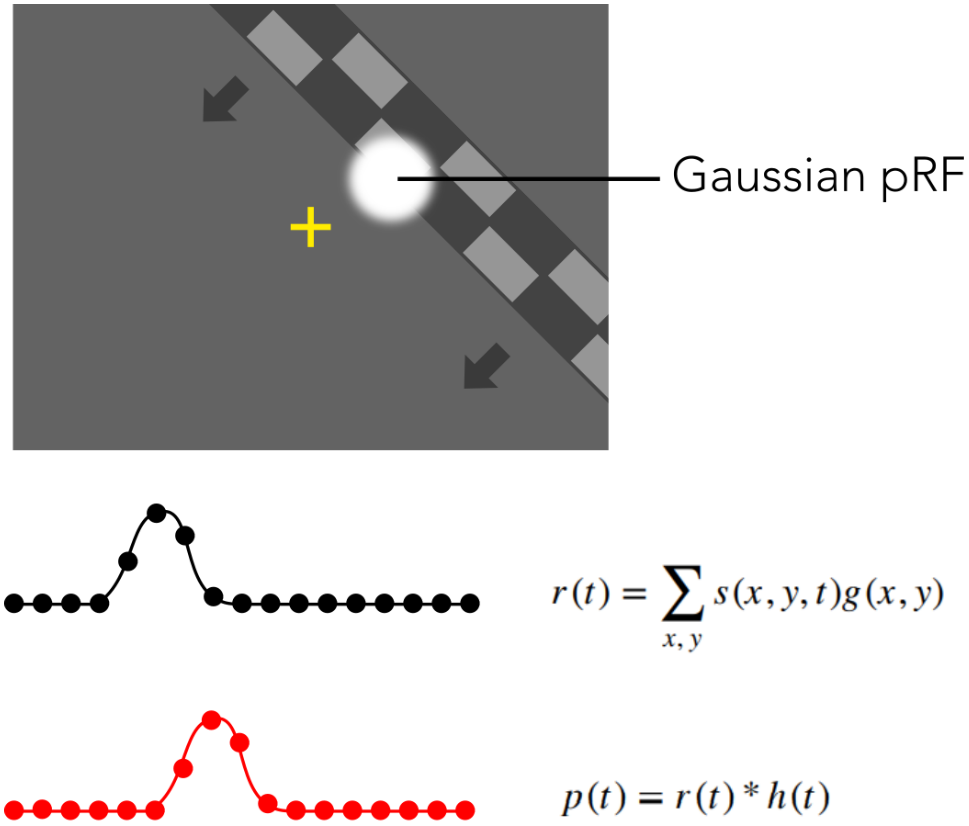

Figure 4.6: Visualization of pRF model prediction of a single voxel. (Top) Graphical representation of Gaussian pRF during a bar stimulus presentation, the bar aperture reveals the checkerboard pattern as it sweeps across the screen, stimulating a visual response from the voxel. The black dotted line (middle) is the example of a predicted pRF response using the multiplication of the effective stimulus location and the Gaussian pRF. The red dotted line (bottom) is an example of the predicted BOLD time series response after convolving with the predicted pRF response with the hemodynamic response function (HRF), resulting in a 'lag' in the time series data.

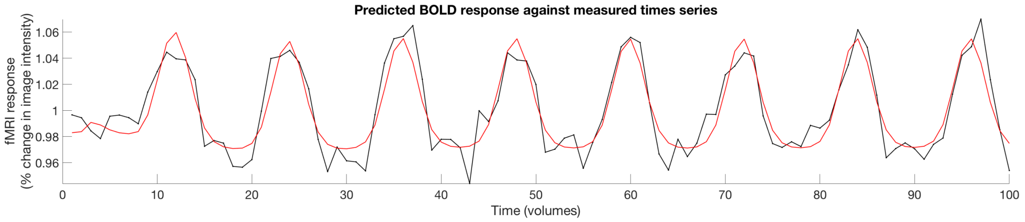

Figure 4.7: Example of a good fit between the predicted BOLD response and the measured time series. The black represents the measured time series data while the red line is our predicted BOLD response using the population receptive field model and effective stimulus frequency.

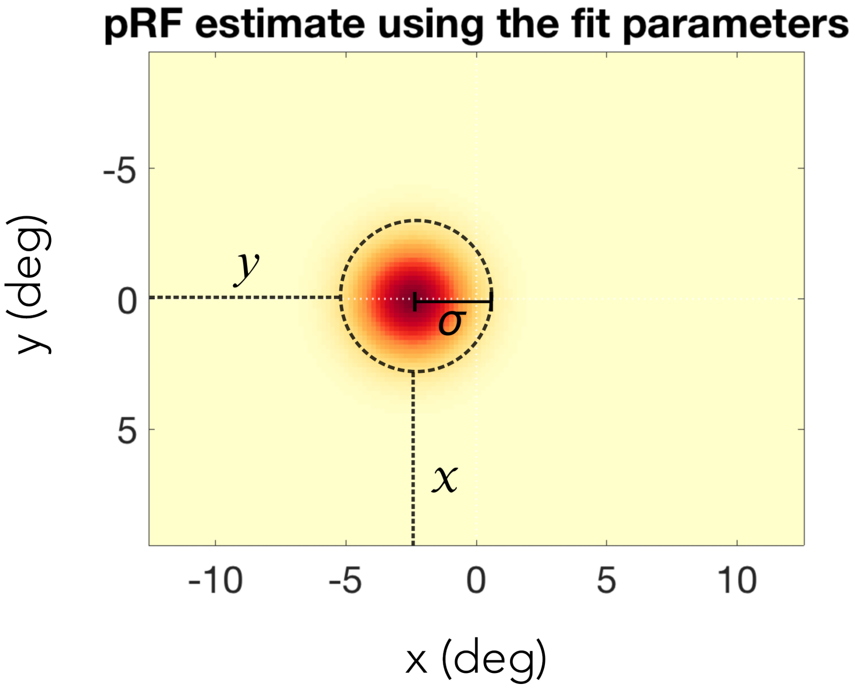

Figure 4.8: Example of a pRF model represented in visual space, using the fit parameters defined by the pRF estimate. $[x_0, y_0]$ represent the centre of the pRF location and σ represents the size of the pRF.

4.3.2 Assessing the model fit

The quality of the fit was assessed using r^2, the coefficient of determination, which provides information about the variance accounted for by the model. A threshold value of r^2 for "reliable" voxel estimates in the visual areas was determined by reference to a non-visually responsive area in the brain. Across each participant, we selected a small region of interest (ROI) in the prefrontal cortex and determined the value of 3 SD above the mean r^2 to act as the threshold. This approach is similar to that described in Papanikolaou et al. (2014). Both Figure 4.9 and Figure 4.10

shows an example of the thresholded r^2 maps from the pRF analysis for participants 11773 overlaid on high resolution anatomical images and an inflated surface respectively. It appears that there are some voxels located in the lesioned hemisphere that still respond reliably to visual stimuli after thresholding against the non-visually responsive area.

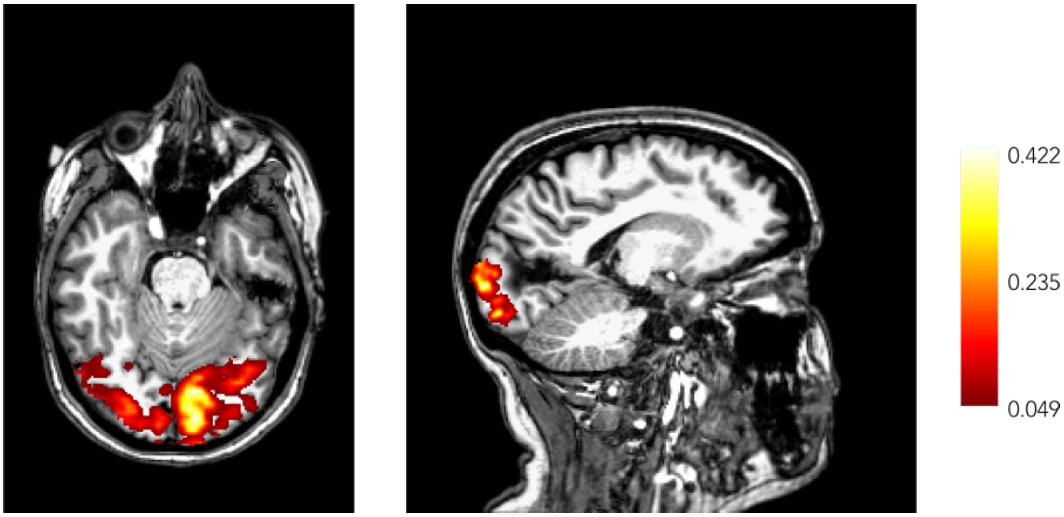

Figure 4.9: Population receptive field (pRF) analysis results in both axial and sagittal view of participant 11773. The coefficient of determination, r^2 for each voxel is overlaid on the high resolution anatomical images for visualization purposes. r^2 values of voxels are thresholded against a non-visually responsive area in the brain (prefrontal cortex), using a value of 3 SD above the mean r^2 of the non-visually responsive region. The color bar represents the r^2 value of the voxels, ranging from low (red) to high (white). Note that participant 11773 has a lesion in the left hemisphere (depicted in the left hand side in the image) and diagnosed with right HVFD. However there are still some responses to visual stimuli located in the lesioned hemisphere.

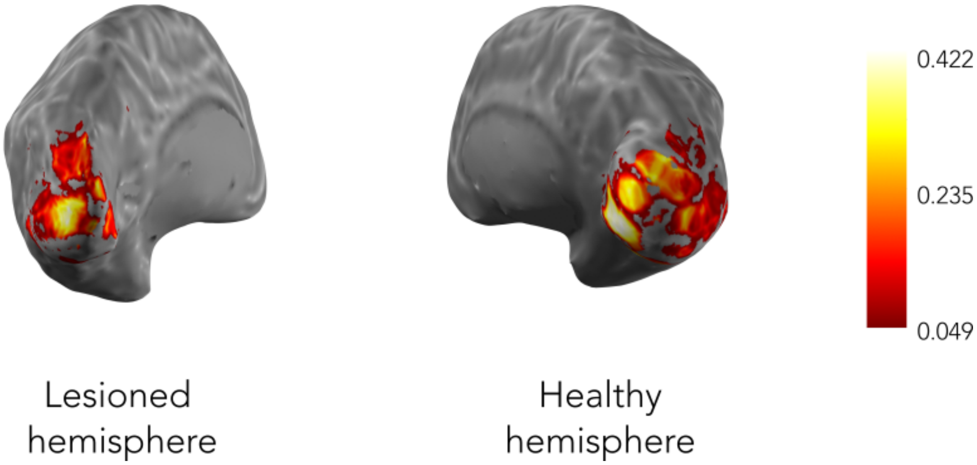

Figure 4.10: Population receptive field (pRF) analysis results of both hemispheres of participant 11773. The coefficient of determination, r^2 for each voxel is overlaid on an inflated surface. The color bar represents the r^2 value of the voxels, ranging from low (red) to high (white).

4.3.3 Visual field coverage maps

Once we established where the functional, responsive voxels were located in visual cortex, including the lesioned hemisphere, we used the information from the pRF model to visualize the corresponding representations in visual space. As introduced above, the pRF model is defined by three parameters x_0, y_0 and σ in visual space, which allows the visualization of the size and location of the pRFs. Figure 4.11 shows an example of the pRF centers and sizes represented in visual space, using a small region of interest (ROI) selected in the lesioned hemisphere.

Using a method described in Papanikolaou et al. (2014), the pRF estimates can be represented using visual field coverage maps, highlighting visual field locations that are being driven by activity from responsive voxels, as seen in Figure 4.12. This is done by first creating a mesh-grid with rows and columns representing polar angles (0 - 360°) and eccentricities (0 - 10°) in visual space, using Matlab R2016b (MathWorks, Natick, MA). The *mesh-grid* is then converted into cartesian coordinates (*pol2cart*), allowing us to apply the fit parameters onto the *mesh-grid*. Each pRF model will be separately represented onto a *mesh-grid* in, fitting a 2D Gaussian shape where the [x_0, y_0] defines the location of the Gaussian model and the σ defines the Gaussian amplitude. The Gaussian model is then weighted by the response amplitude of the voxel. The maximum pRF amplitude across all pRFs is then taken for each visual field location, producing the visual coverage maps. For the normalized map, the fitted Gaussian model is normalized to 1. For the non-normalized map, the color map is plotted with the maximum color value taken at the median pRF amplitude across all pRFs, which allows the maps to maintain sensitivity to weaker responses across visual field locations.

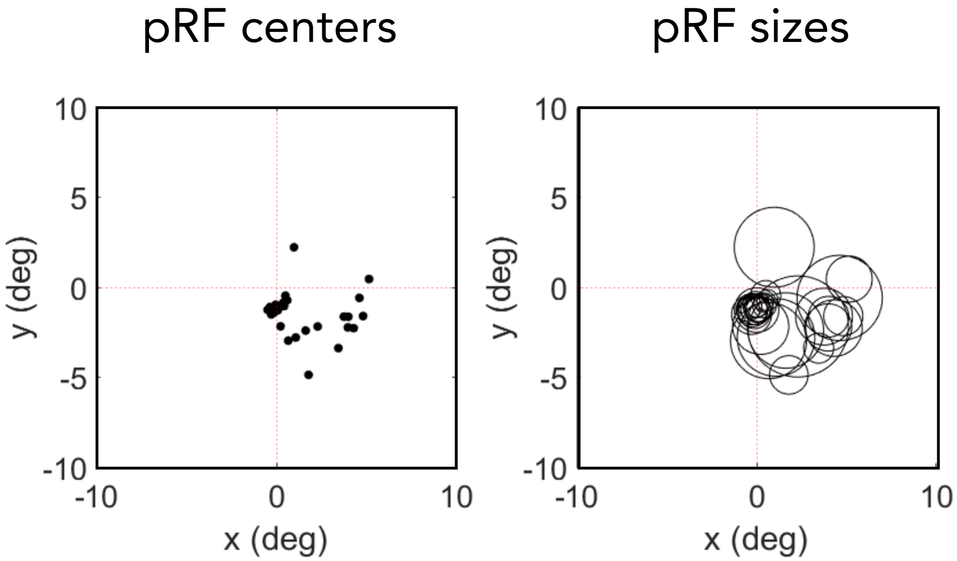

Figure 4.11: pRF model representation in visual space, data taken from participant 11773 who has right HVFD. We selected a small ROI from the voxels located in the lesioned (left) hemisphere with reliable pRF model fits for visualization purposes. Using the pRF voxel estimates, we represented the pRF center (left) locations using $[x_0, y_0]$ and the pRF sizes (right) using σ. Although perimetry results show no visual function in the right hemifield, the pRF analysis reveals regions in the lesion hemisphere that still respond to visual stimuli, most notably in the lower right quadrant.

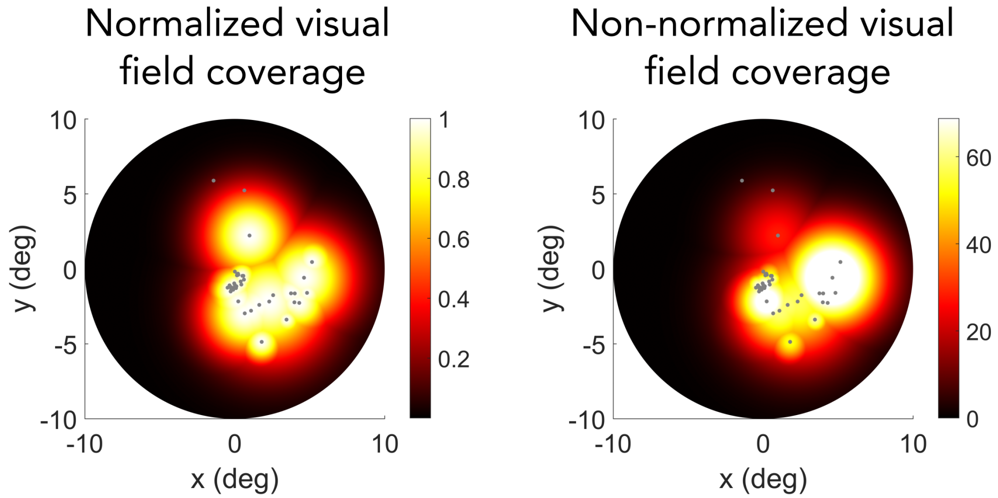

Figure 4.12: Normalized and non-normalized visual field coverage maps constructed from a small ROI selected from visually responsive regions in the lesioned hemisphere. The pRF centers across each pRF model is plotted as gray dots.For the normalized map, the fitted Gaussian model is normalized to 1. For the non-normalized map, the color map is plotted with the maximum color value taken at the median pRF amplitude across all pRFs, which allows the maps to maintain sensitivity to weaker responses across visual field locations.

4.4 Using a probabilistic atlas to define visual regions

Cortical damage due to stroke can affect image segmentation with tools optimized for neurologically normal brains (Lutkenhoff et al., 2014). In particular, reconstruction of the gray matter and white matter surfaces, inflation and flattening of lesioned hemispheres with freesurfer or caret may not be routinely possible. To allow the same analysis steps for intact and lesioned hemispheres, we therefore used a volume-based approach to relate anatomical lesions and residual functional responses to the known layout of visual areas.

We first registered data from fMRI space to the individual's T1 anatomy scan (mrAlign, Nestares and Heeger (2000)) and the anatomy scans into MNI152 space (12 dof, FLIRT, Jenkinson et al. (2012)) (see Chapter 5 for a more detailed explanation of the anatomical lesion segmentation and normalization process). To allow comparisons across imaging modalities, we used the 1mm isotropic standard MNI space as a common target for final visualisations and data summaries. For example, statistical maps derived from BOLD fMRI (pRF maps) were super-sampled from $3mm^3$ into this $1mm^3$ space. This was particularly important, as it allowed us to map fMRI responses, anatomical lesion quantification and other derived measures, eg. from the pRF analysis, to be characterized by the same probabilistic atlas (viz L. Wang et al. (2015)). We used the maximum probability maps derived from the volume based analysis of the L. Wang et al. (2015) atlas to characterize the different visual regions (see Chapter

5 for an explanation of how we organized cortical ROIs defined by the atlas).

4.5 Visual field maps reveal cortical responses in “blind” portions of visual field

To identify any residual functional activity in the regions of cortex corresponding to visual field defects, we mapped the pRF centres $[x_0, y_0]$ from the lesioned hemisphere onto the corresponding static perimetry results as seen in Figure 4.13. In the visualization of the anatomical results (see Chapter 5 for more details), we grouped the pRF models into cortical territories (*early visual, ventral, lateral occipital* and *dorsal* regions. The L. Wang et al. (2015) atlas also included a frontal region of interest, but no pRF model fits exceeded the threshold for reliable responses.

To quantify the visual capacity in the ‘blind’ region, we took into account the extent of each voxel pRF (circular region in visual space, centered at $[x_0, y_0]$ with radius σ) and measured the number of pRFs that intersected with the scotoma. As the absolute count of reliable pRFs can also be affected by changes in signal-to-noise-ratio of the BOLD signal across participants, we compared these counts to those in the non-lesioned hemisphere. By flipping the ‘blind’ region in the perimetry across the vertical meridian (y-axis) and measuring the number of intersecting pRFs for the non-lesioned hemisphere, we therefore obtained a directly comparable count (within participant and unaffected by changes in pRF fit quality across ROIs; Figure 4.14). The scatter plots in Figure 4.14 show the number of pRFs intersecting with the blind field in the lesioned hemisphere compared to those in the non-lesioned hemisphere. ROIs that fall close to the diagonal line in these plots represent similar pRF counts in the stroke and healthy hemisphere —- indicating unaffected levels of visual response for that region. Points that fall well below the diagonal identify ROIs whose response was substantially reduced in the lesioned hemisphere.

We used a non-parametric statistical test to quantify differences in the distribution of pRF responses overlapping with scotoma and corresponding portion in the intact visual field. For each ROI in each participant, we obtained the distributions of r^2 values and compared them using a Kolmogorov-Smirnov test. Only pRF responses from uniquely identified functional voxels were used for this test. Table 4.1 shows the D statistic and corresponding p-values. The null hypothesis, H_0, for this test is that r^2 values in the healthy and stroke ROIs come from the same distribution. For nearly all ROIs, the distributions in healthy and stroke hemispheres were significantly different from each other based on this test. For some ROIs, notably outside early visual cortex, there were no pRFs that overlapped with either the scotoma or the corresponding region in the intact visual field. This could be due to less consistent alignment of these regions across participants (and with the probabilistic atlas).

In both participant 11773 (hemianopia) and participant 14326 (quadrantanopia), we were able to identify ROIs that had near normal counts of reliable pRFs, indicating visual activity in the 'blind' region of the visual field. Interestingly, such responses were more prominent in *early visual* and *lateral occipital* regions of the lesioned hemisphere. Overall, participant 14196 (hemianopia) showed a smaller extent of functional activity within the ‘blind’ region, as seen in Figure 4.13c and 4.14a. Participant 13978 (quadrantanopia) showed little evidence for any residual function in regions corresponding to the scotoma.

To demonstrate how these spared cortical regions are represented in the visual field, we constructed the normalized and non-normalized visual field coverage maps (Papanikolaou et al., 2014) for three selected ROIs (*V3, LO1, IPS0*) in participant 11773 . These regions showed a high number of pRFs represented within the scotoma. (These ROIs fell close to the diagonal line in the scatter plot in Figure 4.14b). The visual field coverage maps derived from pRFs in these regions showed residual functional activity in the right, lower quadrant of the hemifield within the scotoma. This consistency across visual field coverage maps, derived from different regions, adds supporting evidence for some common residual processing of information from these regions of the visual field.

Table 4.1: Differences in population receptive field coverage in lesioned and healthy hemispheres.

ROI	11773		13978		14196		14326	
	D	*p*	*D*	*p*	*D*	*p*	*D*	*p*
V1v	0.568	$< 1e^{-8}$	0.627	$< 1e^{-8}$	0.659	$< 1e^{-8}$	0.341	$< 1e^{-8}$
V1d	0.587	$< 1e^{-8}$	0.396	$< 1e^{-8}$	0.73	$< 1e^{-8}$	0.419	$< 1e^{-8}$
V2v	0.777	$< 1e^{-8}$	0.546	$< 1e^{-8}$	0.859	$< 1e^{-8}$	0.546	**N.S.**
V2d	0.377	$< 1e^{-8}$	0.316	$< 1e^{-8}$	0.73	$< 1e^{-8}$	0.206	$< 1e^{-8}$
V3v	0.806	$< 1e^{-8}$	0.888	$< 1e^{-8}$	0.916	$< 1e^{-8}$	0.842	$< 1e^{-8}$
V3d	0.352	$< 1e^{-8}$	0.536	**N.S.**	0.783	$< 1e^{-8}$	0.13	< 0.01
hV4	0.709	$< 1e^{-8}$	1.000	< 0.01	0.788	$< 1e^{-8}$	1.000	< 0.01
VO1	0.862	$< 1e^{-8}$	0.763	$< 1e^{-5}$	0.826	$< 1e^{-8}$	-	-
VO2	0.410	$< 1e^{-8}$	0.784	$< 1e^{-8}$	0.676	$< 1e^{-8}$	0.907	$< 1e^{-8}$
PHC1	0.38	< 0.01	0.969	$< 1e^{-8}$	0.352	**N.S.**	-	-
PHC2	0.862	$< 1e^{-8}$	-	-	0.641	$< 1e^{-8}$	0.597	$< 1e^{-5}$
hMT	0.526	$< 1e^{-8}$	1.000	$< 1e^{-8}$	0.594	$< 1e^{-5}$	0.652	< 0.01
LO1	0.213	$< 1e^{-8}$	0.636	$< 1e^{-8}$	0.626	$< 1e^{-8}$	0.732	$< 1e^{-8}$
LO2	0.271	$< 1e^{-8}$	0.966	$< 1e^{-8}$	0.451	$< 1e^{-8}$	-	-
V3a	0.207	$< 1e^{-8}$	0.622	$< 1e^{-8}$	0.902	$< 1e^{-8}$	0.623	$< 1e^{-8}$
V3b	0.152	< 0.01	0.515	< 0.01	0.789	$< 1e^{-8}$	0.585	< 0.01
IPS0	0.143	$< 1e^{-5}$	0.305	< 0.01	0.379	$< 1e^{-8}$	0.932	$< 1e^{-8}$
IPS1	0.211	$< 1e^{-5}$	0.750	$< 1e^{-5}$	0.444	$< 1e^{-5}$	0.929	$< 1e^{-8}$
IPS2	0.675	$< 1e^{-8}$	-	-	-	-	-	-
IPS3	0.608	< 0.01	-	-	-	-	-	-
IPS4	0.750	**N.S.**	-	-	-	-	-	-
SPL1	0.500	**N.S.**	-	-	-	-	-	-
FEF	1.000	**N.S.**	-	-	-	-	-	-

Statistical summary of regions of interest whose pRF responses overlap with scotoma (voxels from lesioned hemisphere) or corresponding portion in intact visual field from intact hemisphere). We compared the distributions of r^2 values of the healthy and stroke ROIs using a Kolmogorov-Smirnov test. Only pRF responses from uniquely identified functional voxels were used. *Rows*, regions of interest identified from probabilistic atlas. *Columns*, *D* statistic and corresponding p-values for each ROI in each participant. The null hypothesis, H_0, for this test is that r^2 values in the healthy/stroke ROIs come from the same distribution. N.S., not significant at α = 0.01. Dashes denote ROIs for which there were no overlapping pRF responses in either the healthy or stroke hemispheres.

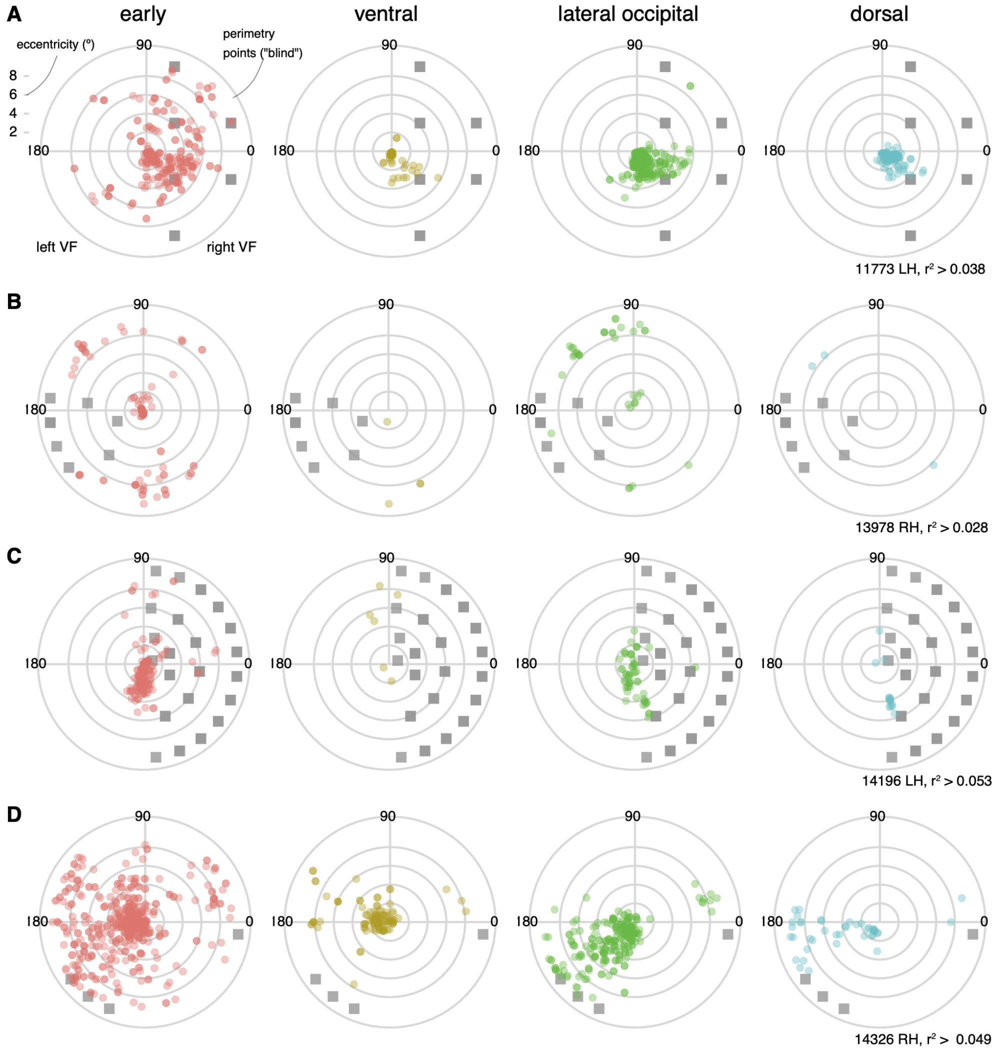

Figure 4.13: Visual field maps derived from functional MRI and population receptive field (pRF) analysis. (A, B, C, D) Population receptive field (pRF) centres are plotted in polar coordinates for each participant to show the voxel representations in the visual field containing the scotoma. Note that in this plot, we only consider the centers of the pRFs that exceed an r^2 threshold determined in a control region. The scatter plot of pRF centers (colored symbols) is overlaid on the scotoma definition from perimetry (gray squares). Data for the ispi-lesional visual field (from the unaffected hemisphere are not shown in light gray symbols). Note that for participant 13978, fixation stability was an issue (and even with gaze-contingent microperimetry, acquiring robust data was challenging). For participant 14326, robust macular sparing was apparent in both standard and microperimetry. Despite this, the fMRI measurements still reveal a different pattern of loss (cf Table 4.1, and Figure 2.3, 2.5).

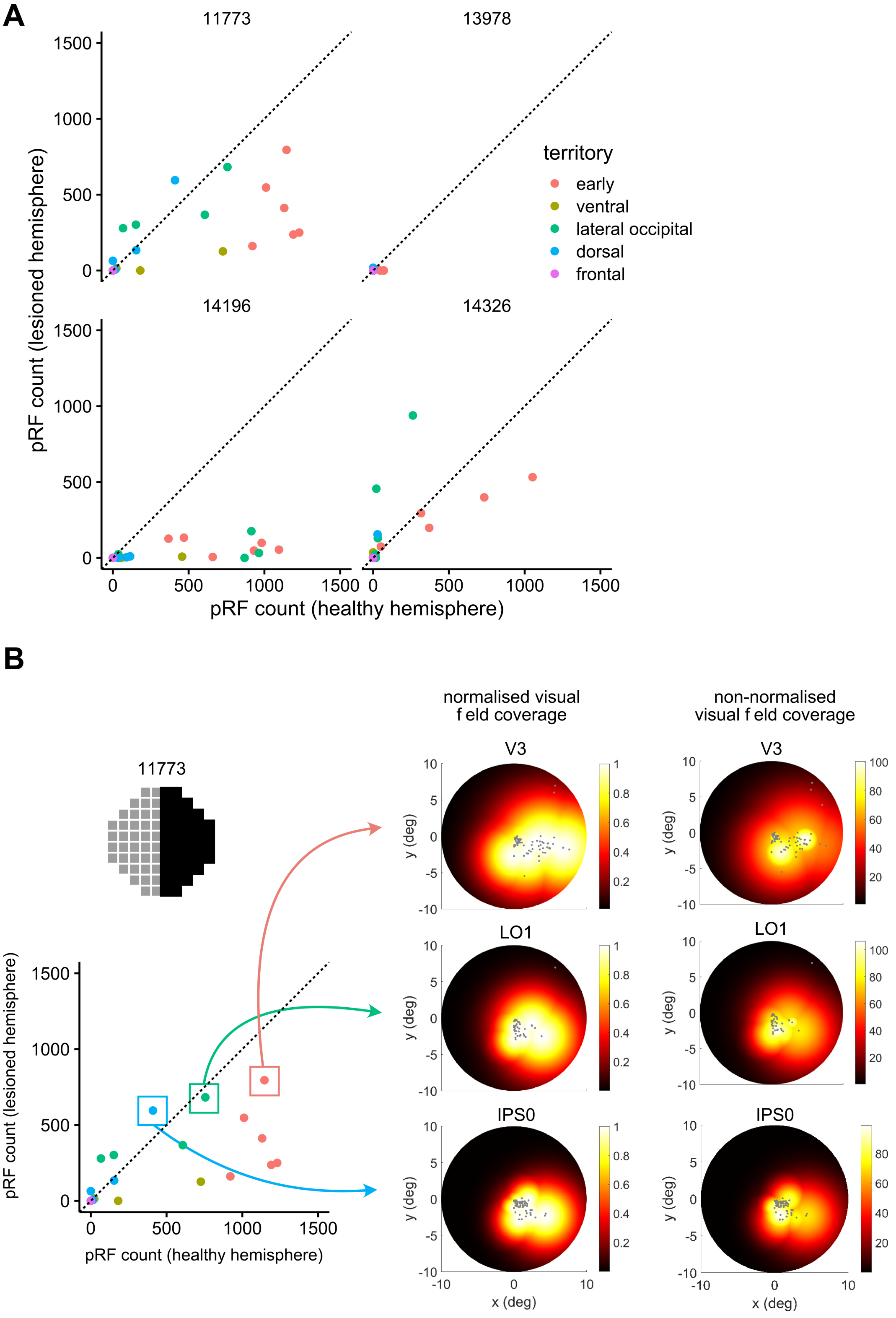
A
11773
13978
14196
14326
1500
1000
500
0
pRF count (lesioned hemisphere)
pRF count (healthy hemisphere)
territory
● early
● ventral
● lateral occipital
● dorsal
● frontal
B
11773
normalised visual field coverage
non-normalised visual field coverage
V3
LO1
IPS0
y (deg)
x (deg)
10
5
0
-5
-10
1
0.8
0.6
0.4
0.2
100
80
60
40
20

Figure 4.14: Quantifying and visualizing residual function from population receptive fields (pRF) (A) Comparing population receptive field (pRF) results between the lesioned and healthy hemisphere for all participants. For each ROI, the number of pRFs (approximated as circles with radius σ) that intersect with the convex hull of the scotoma was calculated. As a control, pRFs intersecting with the scotoma flipped into the non-affected field were counted – this corrects for changes in size of ROIs as well as the ability of the pRF model to fit responses in higher visual areas. Counts related to voxels in 1mm standard space, so equivalent units are mm^3. (B) Three ROIs (for more detail on how we identify cortical areas, see Chapter 5) with high pRF counts in the stroke hemisphere; the pRFs corresponding to voxels in this regions were used to construct normalized and non-normalized visual field coverage maps (Papanikolaou et al., 2014). The domain of the color map used for the non-normalized versions here spanned zero to the maximum pRF amplitude over all voxels. The visual field coverage maps across all three identified subregions show consistent coverage across the lower quadrant.

Chapter 5

Anatomy and White Matter Integrity

5.1 Overview

This chapter will address the analysis of anatomical and diffusion weighted images, which provide important information about intactness of gray and white matter in the lesioned hemispheres. For the anatomical weighted images, I discuss the use of a semi-automatic lesion segmentation process, which circumvents the issues that arise from segmenting abnormal brain structures with conventional skull stripping algorithms. I go on to detail the process of normalizing the images into standard space and mapping regions using a probabilistic atlas, allowing for reproducible and objective measure of lesion size and location.

For the diffusion weighted images, I outline the preprocessing steps which correct for distortions in the images. Using the diffusion tensor model and probabilistic tractography, I was able to quantify the underlying microstructure across the lesioned and healthy hemisphere for all participants.

5.2 Lesion brain segmentation

HVFD is typically caused by damage to the post-geniculate visual pathway, which involves the optic radiations, optic tracts and occipital lobe (Fujino et al., 1986; Goodwin, 2014; J. L. Smith, 1962; Zhang et al., 2006a). Although occipital lobe lesions occur in a lot of HVFD cases (Zhang et al., 2006a), the prognosis is rarely specified to particular visual areas or even differentiating between damage to striate and extrastriate cortices. It is well established that cortical subdivisions of visual areas are functionally distinct from one another (DeYoe et al., 1996), which highlights the importance of a more detailed measurement of the stroke damage and the distinct visual areas that are affected. This line of investigation could provide us with a better understanding of the pattern of damage associated with the visual field defect and presence of any residual visual function.

Anatomical localization of lesions in patients with HVFD is difficult because skull stripping algorithms, registration or normalization tools are usually used under the assumption that the brain structures are healthy and normal. The presence of severe pathology in the brain could lead to these automatic algorithms incorrectly classifying structures, resulting in distorted and warped brain volumes. Moreover, lesion sizes and locations vary across patients with HVFD, (Papanikolaou et al., 2014), which further exacerbates any errors that may arise from comparing lesioned brains to healthy template brains. Hence, it is important to establish a segmentation pipeline that allows for abnormal brain structures to be correctly classified and addresses the homogeneity across lesion sizes and locations.

I have established a semi-automatic process that strikes a good balance between data quality and flexibility when it comes to segmenting the lesions in our dataset. A visualization of this pipeline can be seen in Figure 5.1.

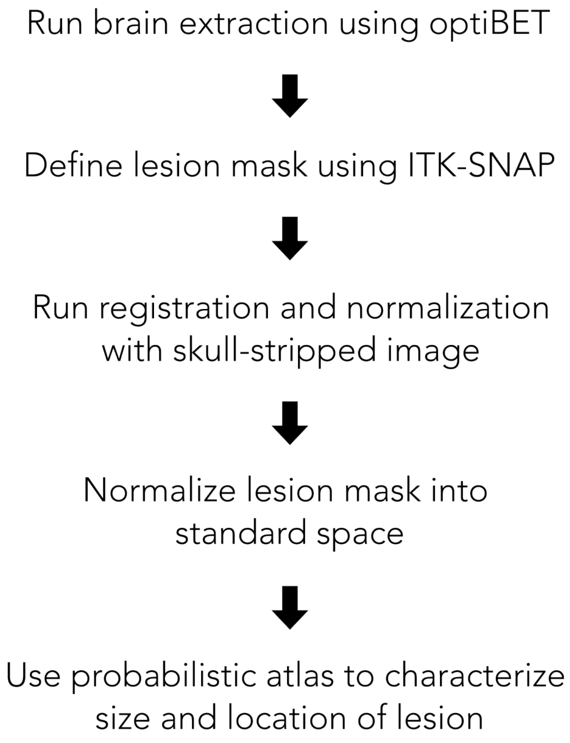

Figure 5.1: Pipeline for semi-automatic lesion segmentation .

5.3 Brain extraction on lesion datasets

Initial pilot testing using conventional skull-stripping algorithms (FSL toolbox, BET, S. M. Smith (2002)) on lesion datasets resulted in distorted and warped outputs. The algorithm is unable to correctly estimate the skull and scalp surfaces in cases where the lesion is close to the skull, as seen in Figure 5.2a. This was the case even when using some of the custom options available with that tool. However, with the use of Optimized Brain Extraction for Pathological Brains (optiBET) (Lutkenhoff et al., 2014) – a tool that wraps bet and is optimized for lesioned brains, I was able to effectively remove non-brain tissue from the high resolution anatomical images. Examples can be seen in Figure 5.2b.

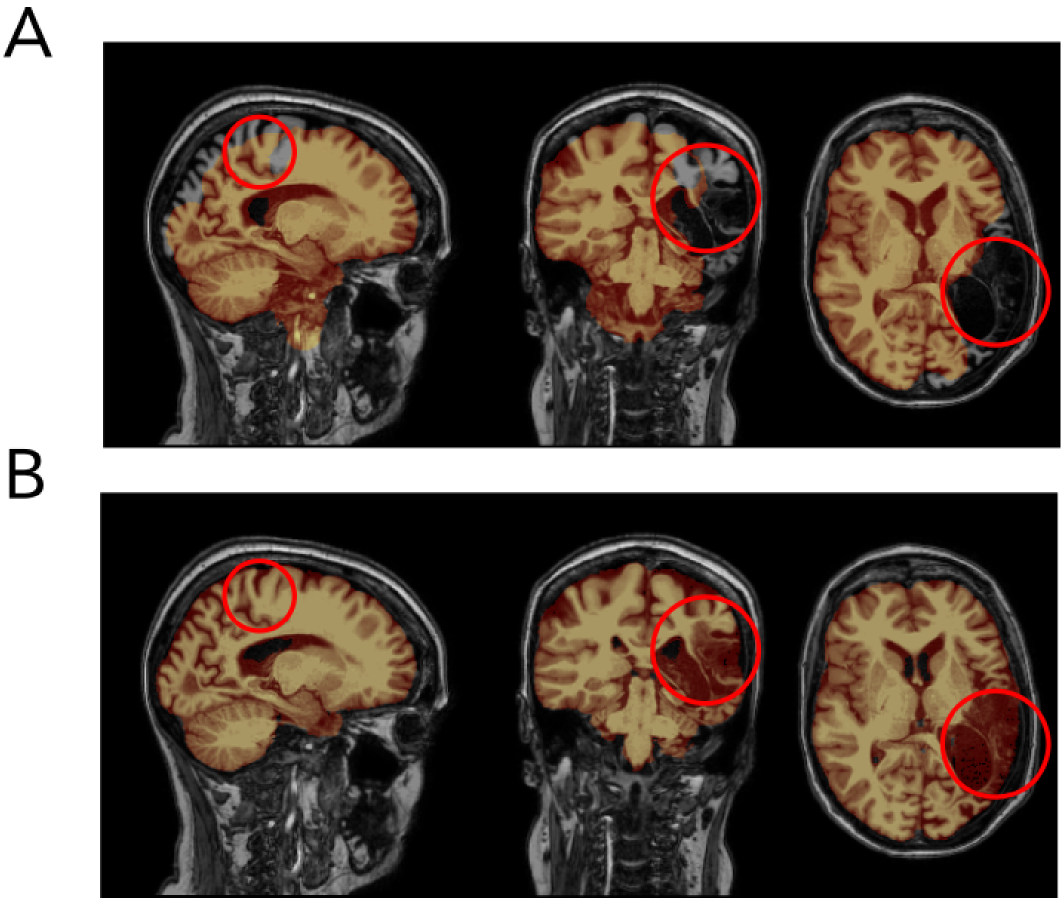

Figure 5.2: Examples of skull-stripping high resolution anatomical images of subject-14196 using (A) FSL-Brain Extraction Tool (BET) and (B) Optimized Brain Extraction for Pathological Brains (optiBET). (A) Failed attempt at skull stripping the lesioned brain using BET. Lesions located near the skull lead to distorted and warped brain masks (red circle). (B) *optiBET* accurately skull-strips brain despite the lesion (red circle), producing optimal brain masks. Note that the gaps in the brain mask are easily dealt with in a later processing step (using the *'-fillh'* command in FSL to fill up the gaps).

5.4 Semi-automatic lesion segmentation using ITK-SNAP

5.4.1 Defining a lesion mask

A stroke-related lesion is an area of tissue in the brain that has been damaged, typically resulting in a heterogeneous cavity filled with cerebospinal fluid (CSF) surrounded by the damaged tissue. Segmentation of lesioned brains is difficult as common segmentation tools (FSL toolbox, FLIRT, Jenkinson et al. (2012)) may perform sub-optimally or completely fail in cases where lesions are very large or near the skull. Abnormal brain structures also present a problem to these tools (ventricles are enlarged as result of the injury, Dalton et al. (2002)). To improve performance of these tools, a lesion mask (a region of interest, ROI, defining where the lesion is in 3D space) is required as it informs the normalization algorithm that this region should not be considered during processing. The lesion mask also allows us to quantify the size and location of the lesion, allowing for statistical analysis. However, the damaged tissue surrounding the lesion may appear very similar to grey matter in T1-weighted images which makes manual identification of the lesion also challenging. Although manually tracing lesions is the gold standard of lesion segmentation for T1-weighted images, it is difficult and labour intensive, and highly dependent on the expertise of the tracer (Fiez et al., 2000; Liew et al., 2018).

Using a semi-automated segmentation tool allows for automated algorithms to segment the data with support of expert inputs guiding more ‘tricky’ anatomies. ITK-SNAP (Version 3.8.0; Yushkevich et al. (2016)) is a software application used to segment 3D brain structures and for image visualisation. It is a powerful tool for lesion characterization as it allows for semi-automatic segmentation using active contour methods. To demonstrate the effectiveness of this tool, I will briefly outline the step-by-step process of identifying the lesion in subject-13978 (Figure 5.3).

Initial visual inspection reveals the lesion to be in the right hemisphere near the occipital lobe. Firstly, to isolate the lesion in the T1-weighted anatomy images, I set an upper and lower threshold of the image intensity values, as lesioned tissues appear darker than non-lesioned tissue. The objective is to get the lesioned tissue to appear ‘white’ while non-lesioned tissue to appear ‘blue’ in the tool as seen in Figure 5.4. Next, seed points are placed along regions colored in white (lesioned tissue) to prepare for active contour segmentation as seen in Figure 5.5. The active contour method (also known as snakes) is a computer vision tool that allows for feature extraction by detecting the edges forming the boundary given some sample points (Acton, 2009). ITK-SNAP uses a 3D active contour method (Caselles et al., 1995; Zhu & Yuille, 1996) that involves iteratively evolving a structure of interest represented by one or more contours (for a more in depth explanation, see Yushkevich et al. (2006)). Essentially, a few spherical seed points (contours) progressively grow (given particular constraints) at each evolution step, which eventually merges into a single contour and allows us to outline and segment a 3D structure (imaging inflating a balloon until it fills up a 3D cavity).

To avoid the 3D segmentation from growing ‘spindle-like’ shapes in the final contour shape, the smoothing (curvature) factor of the contour evolution differential equation was set to 0.8, which prevents the contour from growing into the sulci in the brain. Now the segmentation process is iteratively advanced in steps until the contour has successfully outlined the lesioned tissue. The healthy hemisphere can be used as a visual frame of reference. A final 3D structure is visually inspected to ensure that the lesion is well segmented. An example of the final contour shape of the lesioned tissue in subject-13978 can be seen in Figure 5.6.

In some cases, the contour may incorrectly capture sections of the skull, ‘spilling out’ of the tissue, as seen in Figure 5.7a. Using the *fslmaths* command, we can remove any unwanted spillage by multiplying the mask with the (logical) brain mask created earlier using *optiBET*, effectively thresholding voxels outside the brain, as seen in Figure 5.7b.

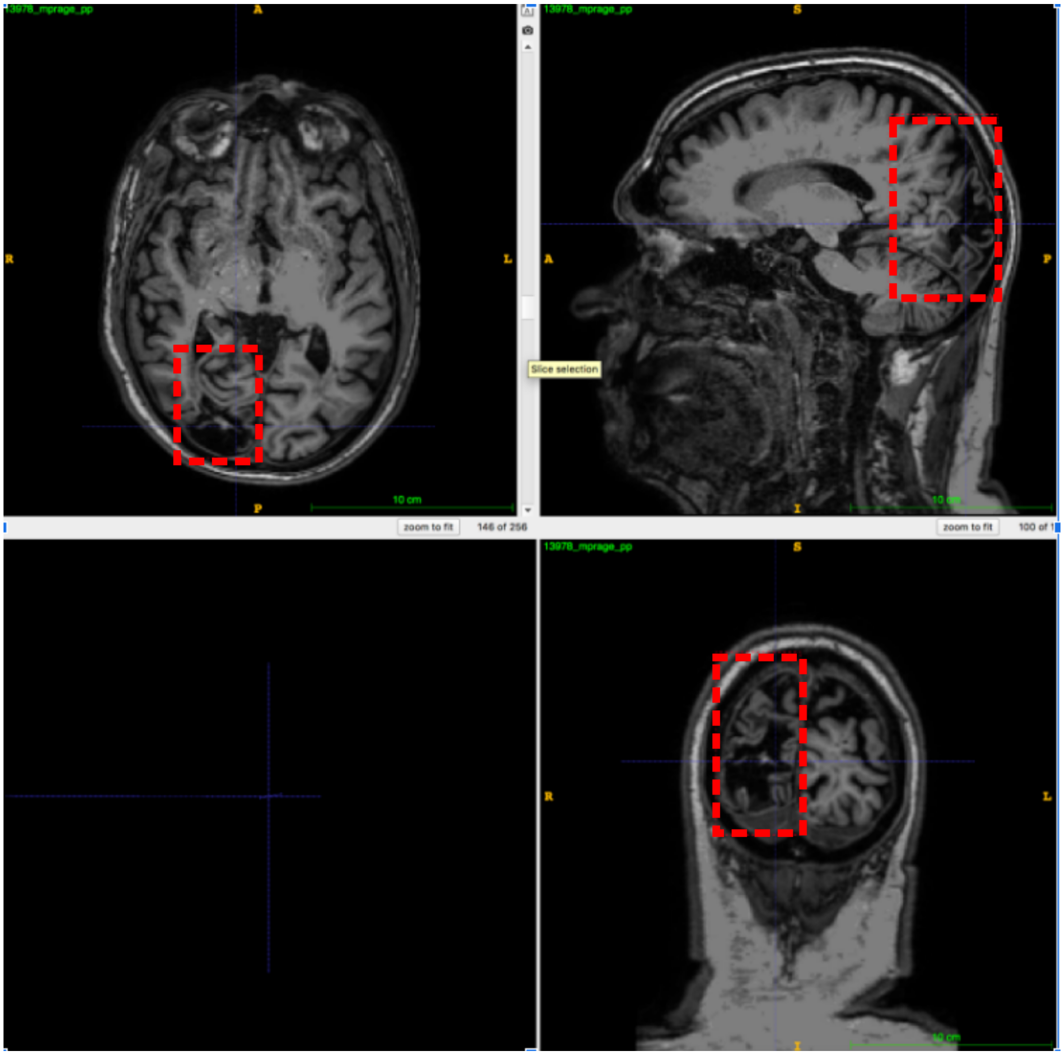

Figure 5.3: Example of lesion identification for subject 13978 using ITK-SNAP. Here we display axial, sagittal and coronal T1-weighted anatomical images of the lesion roughly marked by the red boxes. The lesion visually appears to be in the right hemisphere (left-right orientations are flipped in image) in the occipital lobe.

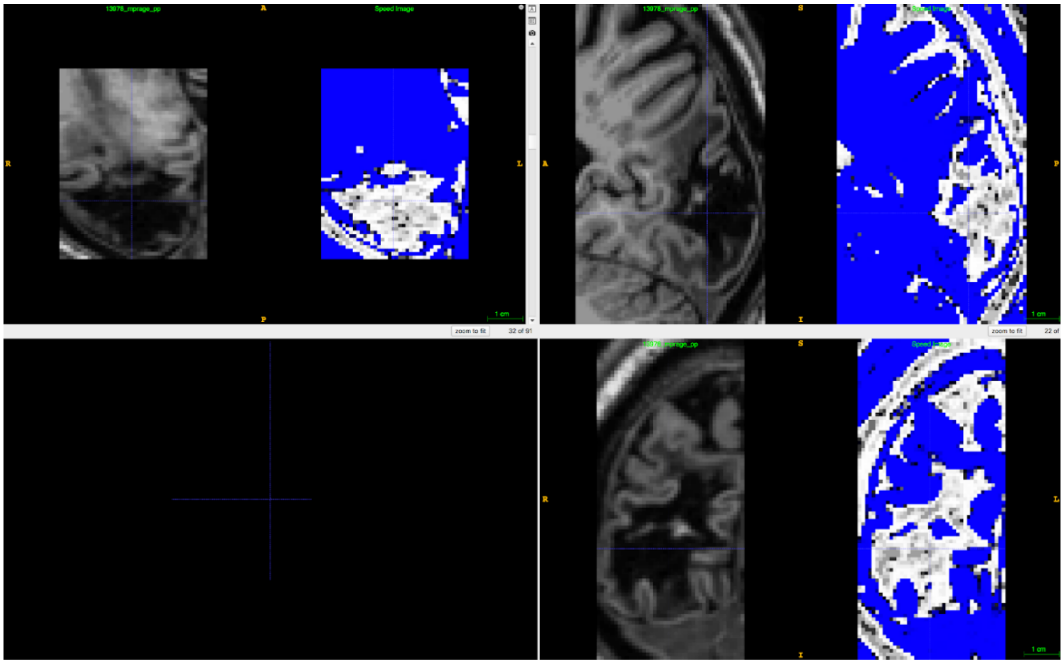

Figure 5.4: Example of thresholding to isolate the lesioned tissue in subject 13978. Here we see that the lesioned tissue correctly appears ‘white’ while the non-lesioned tissue appears ‘blue’ in the tool. Note that some parts of the ventricle appear ‘white’ but should not be considered as the lesion and this will be addressed in a later section.

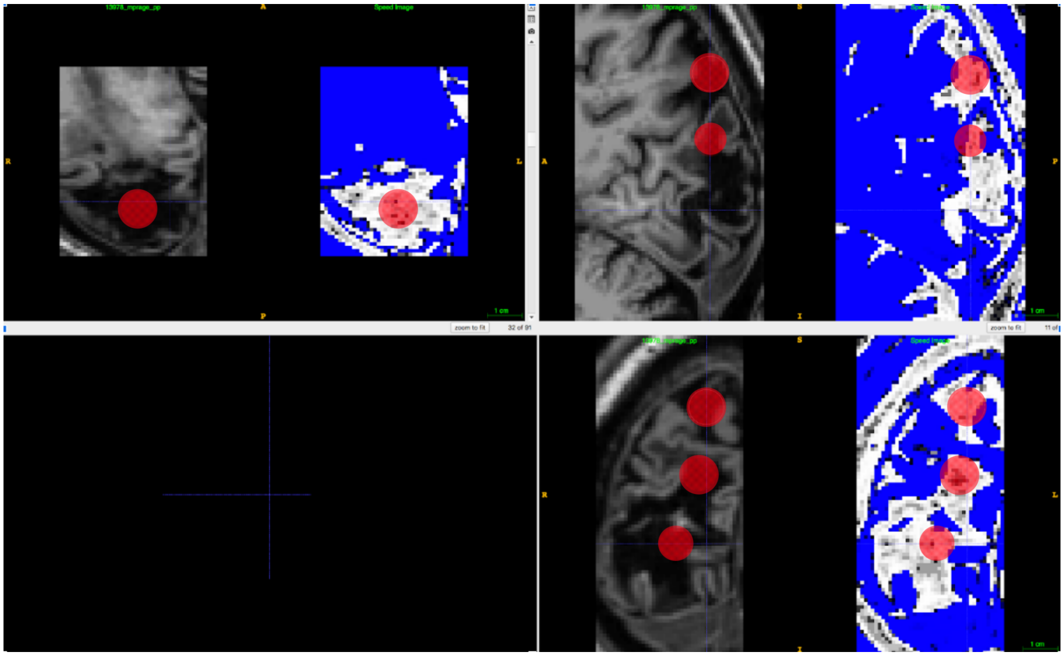

Figure 5.5: Seed points (red bubbles) are placed along regions colored in white (lesioned tissue) to prepare for active contour segmentation.

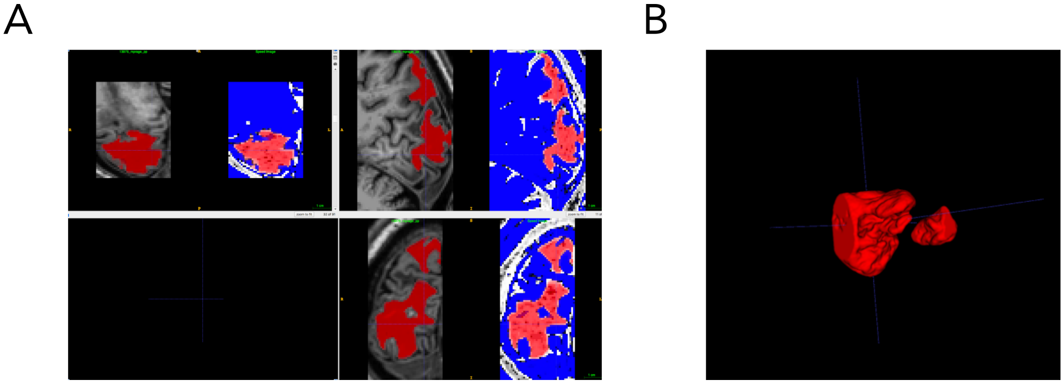

Figure 5.6: Final contour shape of the lesioned tissue. Using a smoothing (curvature) factor of 0.8 in the contour evolution differential equation, we iteratively ‘grow’ the seed points (bubbles) until they outline the lesioned regions. (A) 2D view (axial, sagittal and coronal) of the final contour shape, note that that multiple seed points (bubbles) tend to merge into a single contour if possible. (B) 3D view of the final contour shape, segementating two regions of lesioned tissue.

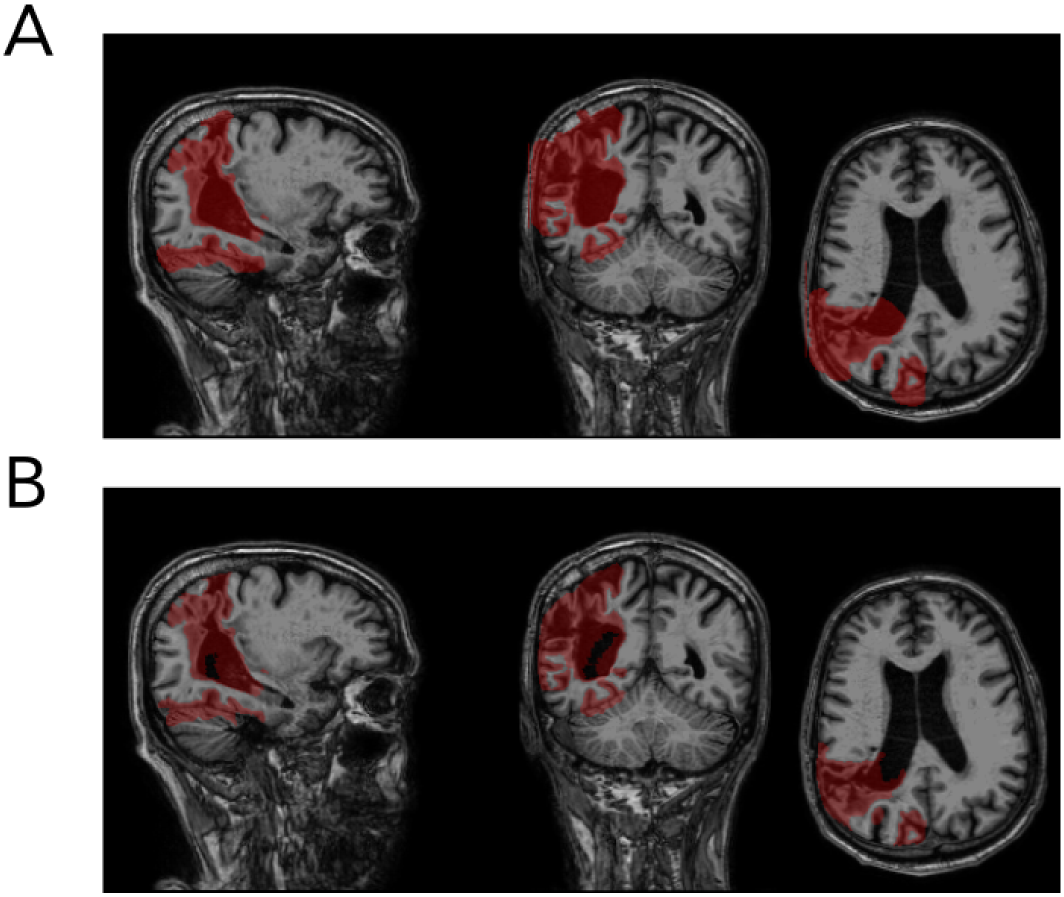

Figure 5.7: Example of lesion mask (created using ITK-SNAP pipeline) for subject-14326. (A) Some sections of the lesion mask are incorrectly capturing sections of the skull, ‘spilling out’ of the tissue. (B) Using *fslmaths* along with the brain masks created using *optiBET*, any of spillage of the lesion mask towards the skull is threshold out.

5.4.2 Managing ventricles

Lesion sites that are adjacent or connected to ventricles make it difficult to correctly segment the lesion, as image intensities across the ventricle and lesion cavities are often similar (Qian et al., 2017). Adding to the challenge, ventricles tend to enlarge as a result of the stroke (Dalton et al., 2002). Hence, it is important to use the ventricle from the healthy hemisphere to correctly adjust for the actual size of the ventricle in the lesioned hemisphere. This allows a more precise characterization of the lesion mask.

Using the previously detailed process of segmenting the lesion mask with ITK-SNAP, we can establish a ventricle mask in the healthy hemisphere, as seen in Figure 5.8a. The ventricle mask is then flipped across the x-axis, mapping it onto the lesioned hemisphere, using the FSL command, *fslswapdim*. In most cases, the flipped ventricle mask is not correctly aligned on the lesioned hemisphere as the brain is typically not aligned exactly parallel to the sagittal axis, as seen in Figure 5.8b. To address this issue, we used the *nudge* function from FSLeyes to correctly position the flipped ventricle mask into a suitable position in 3D space. To ensure correct positioning of the ventricle mask on the lesioned hemisphere, a visual inspection of the final position is carried out across all 3 planes. Figure 5.8c shows the final position of the ventricle mask, which appropriately captures the ventricle in the lesion hemisphere.

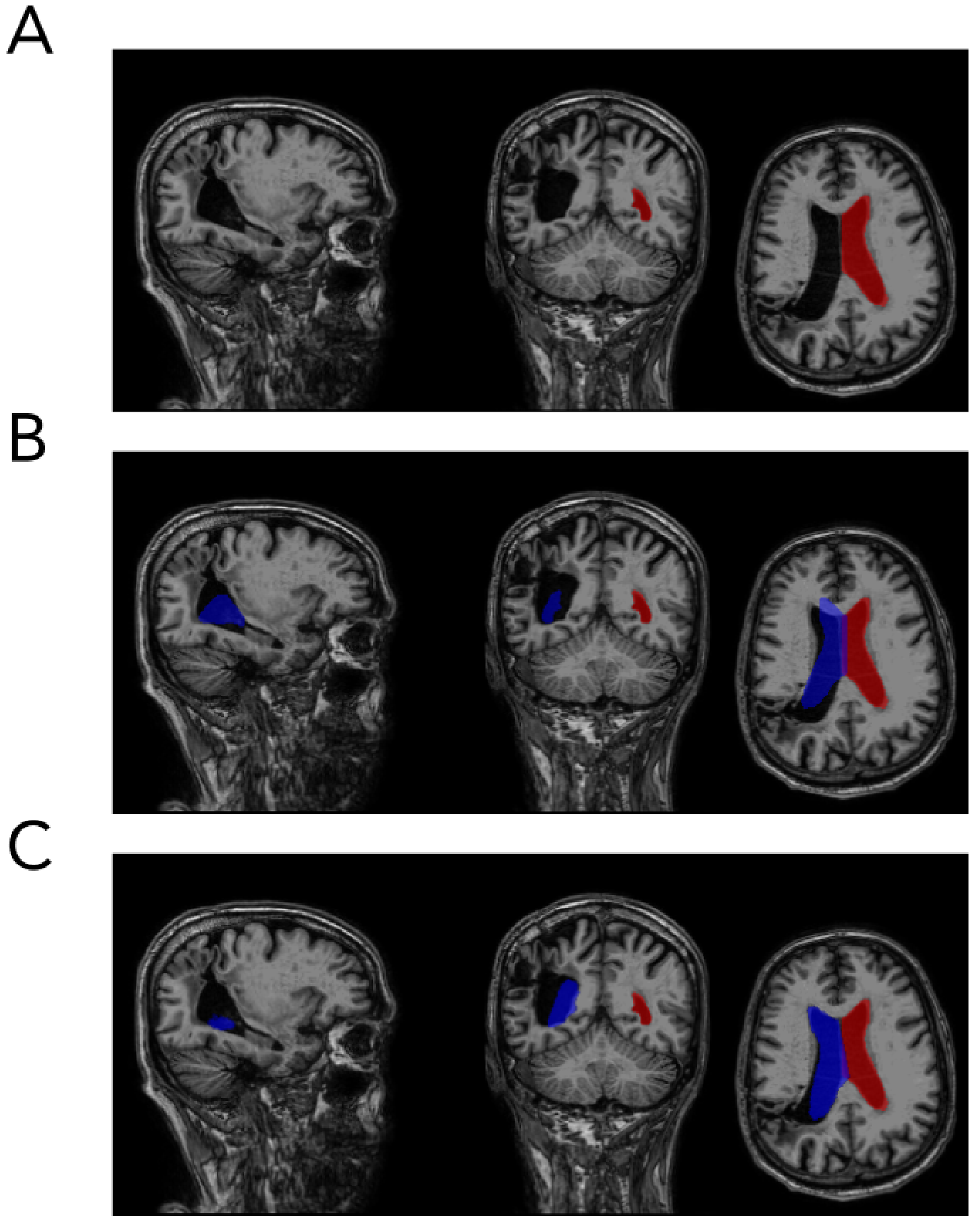

Figure 5.8: Process of creating the ventricle mask using ITK-SNAP for subject-14326. (A) Using the previously detailed process of segmenting the lesion mask with ITK-SNAP, we establish a ventricle mask (red). (B) The ventricle mask (red) is then flipped across the x-axis in attempt to map onto the lesioned hemisphere, using *fslswapdim*. Note that the flipped ventricle (blue) is not correctly aligned to the lesion hemisphere as the brain is not aligned exactly parallel to the saggital axis. (C) Using the *nudge* function from FSLeyes to position the flipped ventricle mask (blue), the mask now correctly captures the ventricle in the lesion hemisphere.

5.5 Registering and normalizing the lesion mask to standard space

Figure 5.9a illustrates the overlap between the flipped ventricle mask and lesion mask and shows the importance of segmenting the 'healthy' parts of the ventricle out of the lesion (using *fslmaths*), leaving a more precise and reliable characterization of the lesion as seen in Figure 5.9b. As a final measure, I used the *erode* and *dilate* function in FSL to smooth and prevent any gaps within the mask. I also removed any clusters from the lesion mask that are smaller than 10 voxels.

The normalization procedure is carried out using a custom script (*lesion_norm_fsl.sh*, Patterson (2019)), which normalizes the image into standard space using 2 inputs: (i) the T1-weighted anatomical image; (ii) the lesion mask. The following commands are found in the FSL toolbox (Jenkinson et al., 2012). The pipeline begins with a version of *fsl_anat*, which allows for the use of *optiBET* instead of BET in the skullstripping phase and includes the lesion mask in the preprocessing steps. Firstly, both images (brain and lesion mask) are reoriented to standard MNI orientation (*fslreorient2std*) and cropped (*robustfov*). To correct for radiofrequency field (RF) inhomogeneities, a bias-field correction is performed using FAST. Both images are then registered to standard MNI152 space (12 degrees of freedom, FLIRT) using affine transformation with nearest neighbour interpolation. A visual inspection of the images was performed to ensure that the normalization process was successful. Figure 5.9c shows an example of a lesion mask overlaid onto the lesioned brain in MNI space, accurately capturing the lesion in standard space.

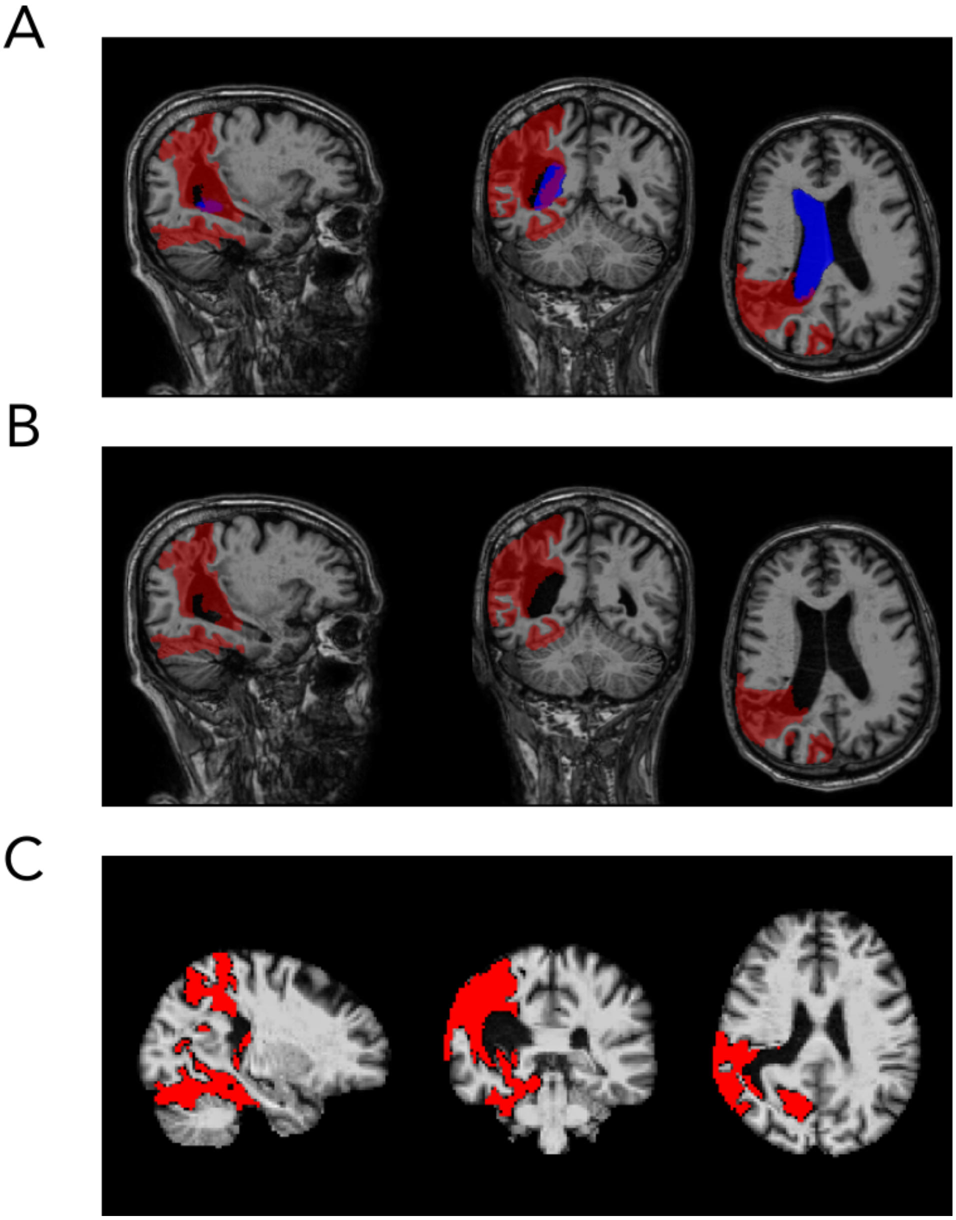

Figure 5.9: Charaterizing the lesion on a standard brain (MNI template) for subject-14326. (A) Note that there is an overlap between the lesion mask (red) and the flipped ventricle mask (blue). (B) Using *fslmaths*, we threshold out the ventricle (with reference to the healthy hemisphere) from the lesion mask, resulting in a more precise and reliable characterization of the lesion. (C) Example of the lesion mask represented in standard space after normalization.

5.6 Probabilistic atlas

To characterise how the stroke lesion affected different visual regions in the brain, we used a probabilistic atlas, in particular, the volume-based, maximum probability maps of the L. Wang et al. (2015) atlas. This atlas defines 25 cortical ROIs in visually responsive areas. This allowed us to quantify lesions by computing the percentage overlap between the lesion definitions in individual participants and the 25 cortical ROIs. To aid visualisation, we grouped the ROIs into 5 cortical territories: *early visual* (V1v, V1d, V2v, V2d, V3v, V3d), *ventral* (hV4, VO1, VO2, PHC1, PHC2), *lateral occipital* (MST, hMT, LO1, LO2, V3a, V3b), *dorsal* (IPS1, IPS2, IPS3, IPS4, IPS5, SPL1) and *frontal* (FEF), as seen in Figure 5.10.

By measuring the overlap between the defined lesion mask (see section 5.4) and cortical ROIs from L. Wang et al. (2015) atlas, we could define a reproducible and objective measure of the lesion size and location — a participant-specific lesion fingerprint. As both images were transformed into standard space, we calculated the proportion of voxels defined as a lesion against the total voxels defined by each of the 25 cortical ROIs, where 0% would indicate total sparing of cortex in the corresponding region of interest, and 100% would indicate a complete loss, as seen in Figure 5.11.

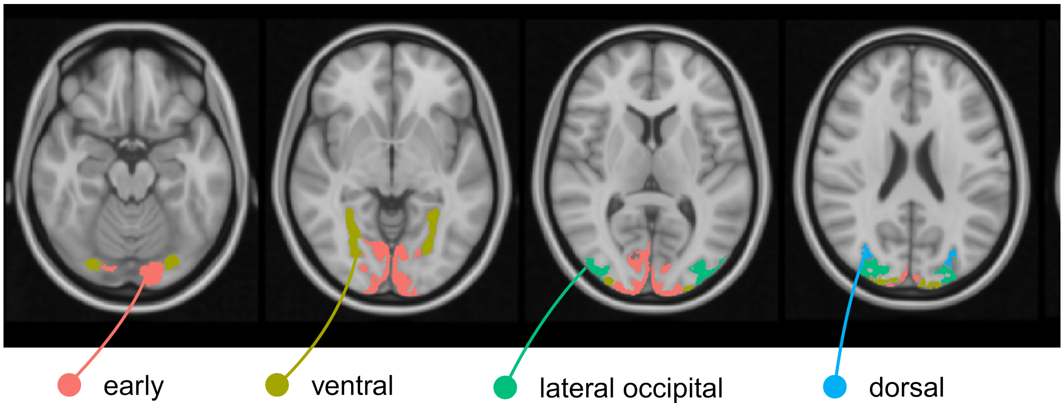

Figure 5.10: Location of cortical ROIs from L. Wang et al. (2015) atlas. The location of the four cortical territories (colours) comprising 25 ROIs are shown on axial slices of the MNI152 brain (gray). Note that the L. Wang et al. (2015) atlas also included labels for frontal eye fields (FEF), but none of the participants showed damage in that region.

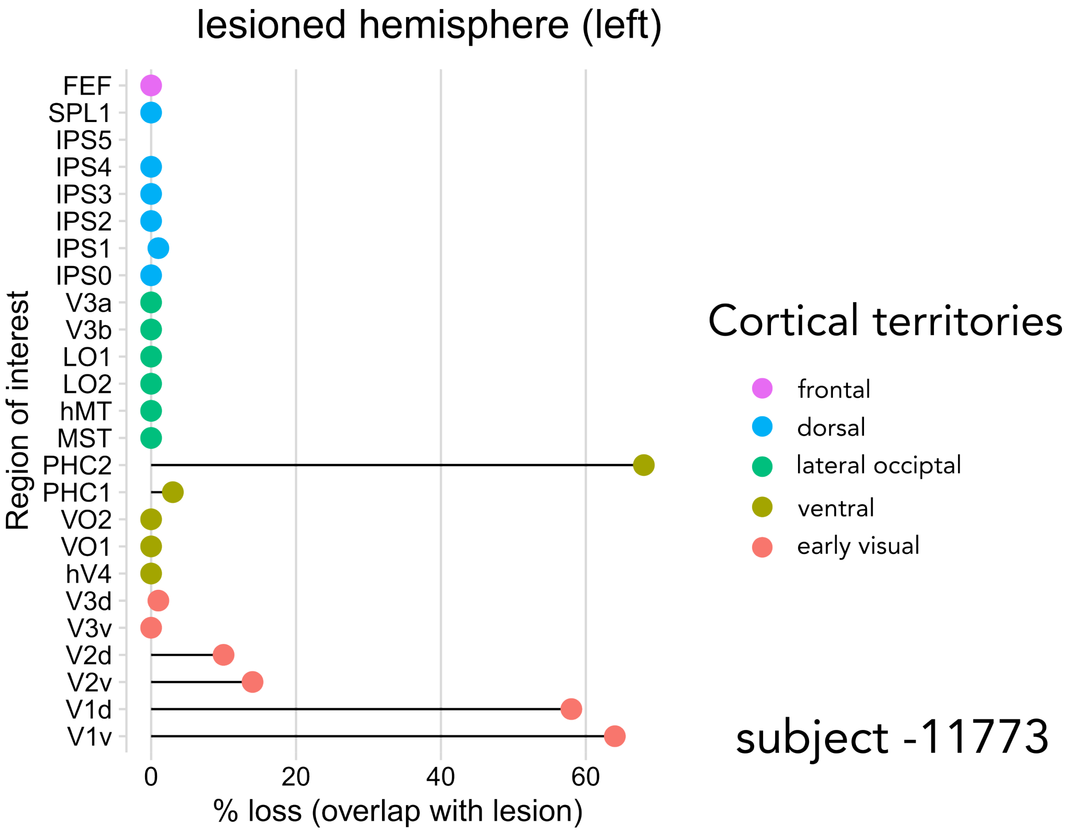

Figure 5.11: Example of lesion characterization of subject 11773. To quantify lesions with respect to known visual areas, we transformed the lesion masks in participant space into MNI space and computed percentage overlap with the regions of interest defined in the probabilistic atlas of L. Wang et al. (2015). Each row (dot) in the dotplot shows percentage loss for an ROI (V1 bottom, to FEF, top), by calculating the proportion of voxels defined as a lesion against the total number of voxels for a given ROI. To aid visualisation, we grouped ROIs into cortical territories: early visual (red), ventral (dark yellow), lateral occipital (green), dorsal (blue). The figure only depicts the lesioned hemisphere (left hemipshere).

5.7 Anatomical results

Figure 5.12 provides a comparison across the lesion characteristics with reference to the perimetry results (5.12a). Both the anatomically defined lesion masks and the T1-weighted anatomical images across all participants can be seen in Figure 5.12b. The dot plots in Figure 5.12c indicate the proportion of these areas lost, 0% indicating total sparing of cortex in the corresponding region of interest, and 100% indicating complete loss.

Lesion size is not a good indicator of visual field loss. All participants showed damage to early and ventral regions, but the extent and pattern of the damage varied widely across participants. For example, participant 11773 – with hemianopia had stroke lesions that were only co-located with early visual areas (Figure 5.12c). Conversely, participant 13978 – with quadrantanopia and an ostensibly smaller visual field loss, showed a much larger anatomical lesion.

Homonymous visual field defects are typically characterized by damage to the early visual cortex (V1-V3). We observed this pattern in three of the four participants (11773, 13978 and 14196). In one participant (14326), the lesion site was dominated by *lateral occipital* regions.

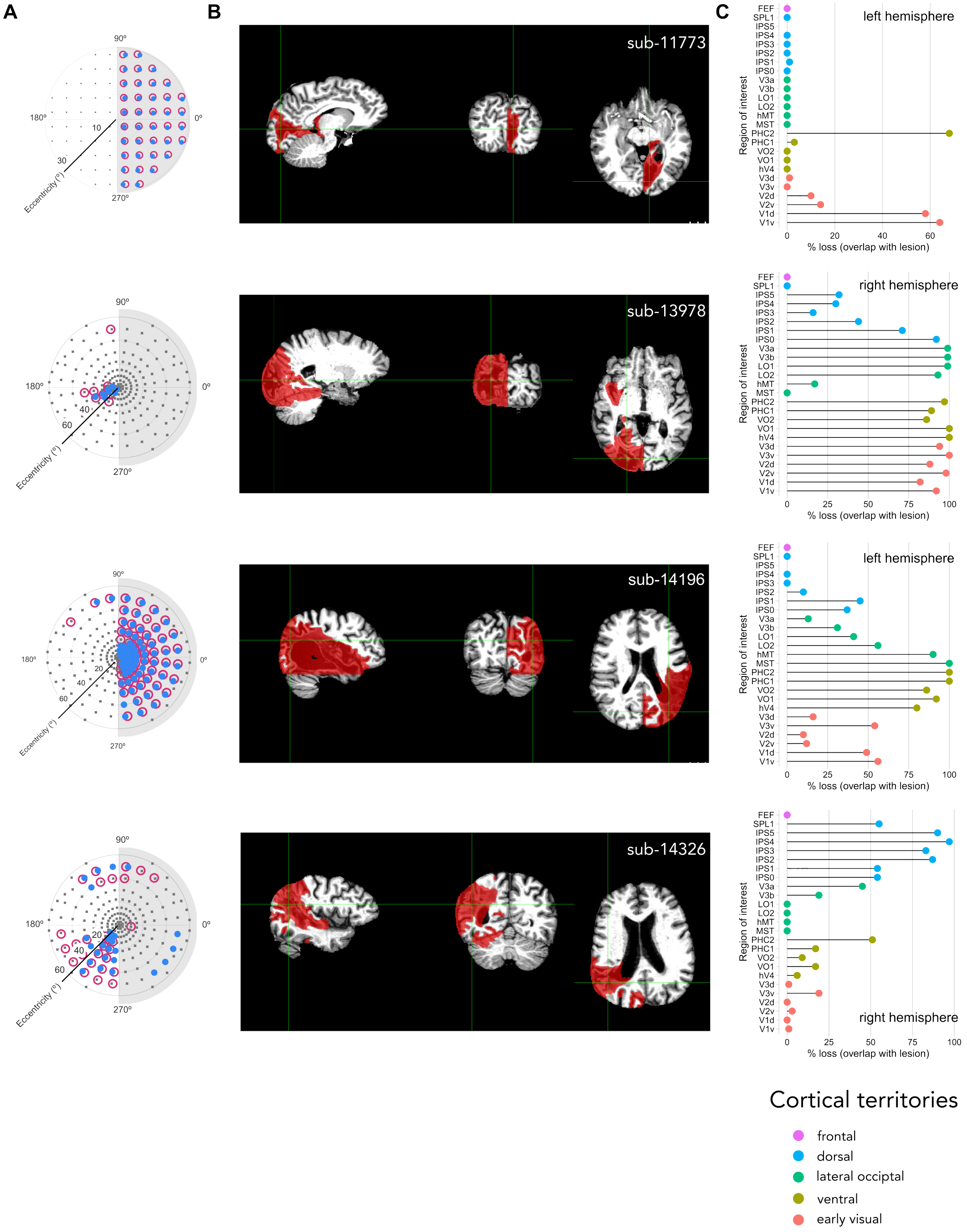
A
B
C
90°
0°
180°
270°
10
20
30
40
60
Eccentricity (°)
sub-11773
sub-13978
sub-14196
sub-14326
left hemisphere
right hemisphere
left hemisphere
right hemisphere
FEF
SPL1
IPS5
IPS4
IPS3
IPS2
IPS1
IPS0
V3a
V3b
LO1
LO2
hMT
MST
PHC2
PHC1
VO2
VO1
hV4
V3d
V3v
V2d
V2v
V1d
V1v
Region of interest
% loss (overlap with lesion)
0
20
40
60
25
50
75
100
Cortical territories
frontal
dorsal
lateral occiptal
ventral
early visual

Figure 5.12: Characterization and quantification of anatomical lesions across each participant (subject 11773, 13978, 14196, 14326) with reference to perimetry results. (A) Definition of homonymous visual field loss with perimetry for both eyes. (B) Brain-extracted anatomical images in sagittal, coronal, and axial view (grayscale), in planes that show the extent of the anatomically defined lesions (red). We used *optiBET* (Lutkenhoff et al., 2014) for skull stripping. (B) Lesion damage by subregions. Each row (dot) of the plot represents percentage overlap between lesion mask and regions of interest defined in the probabilistic atlas of L. Wang et al. (2015). To aid visualisation, we grouped ROIs into cortical territories: early visual (red), ventral (dark yellow), lateral occipital (green), dorsal (blue), see also 5.10.

5.8 T2-weighted images

The current version of my analysis did not use the T2-weighted images for lesion segmentation. However, this is something I intend to further develop in the future. As seen in Figure 5.13, different and meaningful information about the lesion definition can be acquired from both the T1-weighted and T2-weighted images. ITK-SNAP has function that allows semi-automatic lesion segmentation using different image layers by converging across images to isolate the lesion. This would allow for more precise drawings of the lesion mask.

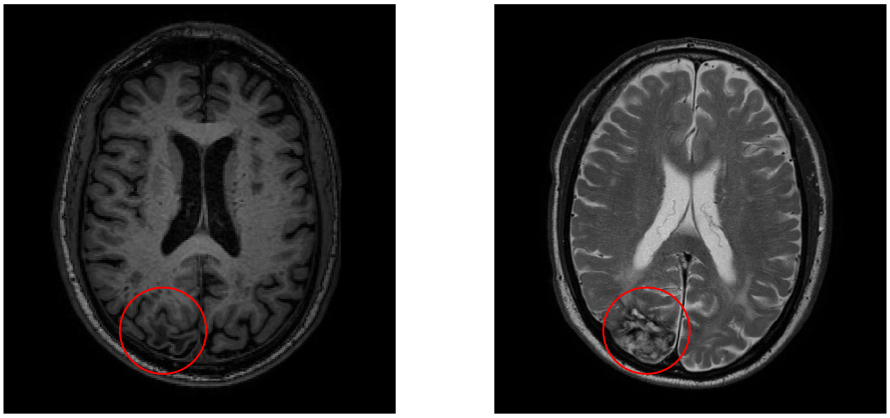

T1-weighted image

T2-weighted image

Figure 5.13: T1-weighted and T2-weighted images of the lesion in axial view. Red circle highlights the lesion site.

5.9 Analysis of diffusion weighted data

To provide a measure of white matter integrity, we used FMRIB's Diffusion Toolbox (FDT) to process the diffusion weighted imaging data. Figure 5.14 shows a pipeline for the diffusion tensor imaging analysis.

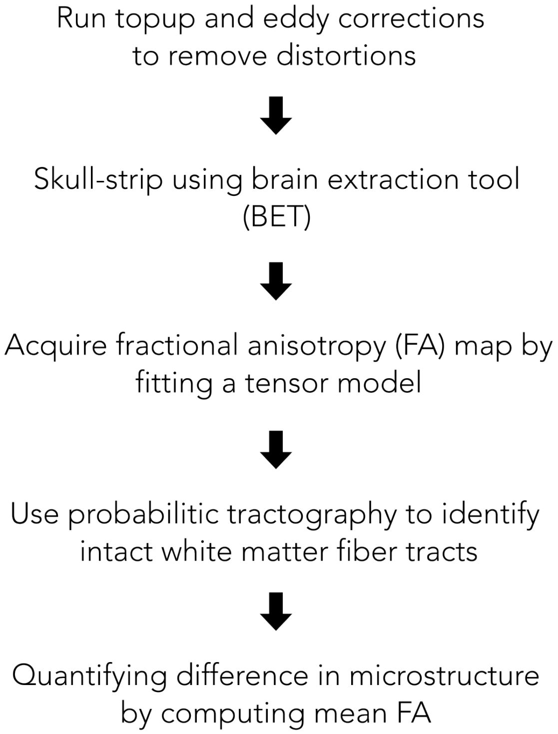

Figure 5.14: Pipeline for diffusion tensor imaging analysis.

5.10 Distortion correction and skull stripping

When an object is introduced into a homogeneous magnetic field, changes in its susceptibility can disrupt the magnetic field, resulting in B_0 magnetic field inhomogeneities. For many forms of imaging, these inhomogeneities lead to localized geometric distortions and drop-outs (susceptibility artifacts). Diffusion data acquired using echo-planar imaging are commonly known to have these distortions.

Using the two calibration images acquired in reversed phase-encoding directions (anterior and posterior direction), we can estimate the distortion and correct for them using FSL's *topup* (Andersson et al., 2003; S. M. Smith et al., 2004). Figure 5.15 shows an example of the calibration images acquired from the anterior and posterior phase directions; the differences in distortions across the two images can be used to estimate a field map. I used the standard steps for running *topup* on our data. Briefly, I merged two images acquired with different phase-encoding into a single dataset, provided information about the acquisition parameters in a text file and estimated the field map and warp field for unwarping using the *topup* command.

For diffusion weighted data, another source of distortions comes from eddy currents, which result from changing magnetic field gradients. I corrected for this distortion and subject motion using the command *eddy*.

Before further processing, I skull-stripped the diffusion weighted data (using *bet* on the mean image across all diffusion directions). Note that lesions appear bright in diffusion weighted data, as seen in Figure 5.16 and does not appear to hinder the skull stripping algorithm (compared to what I found for T1-weighted anatomical data, see 5.3).

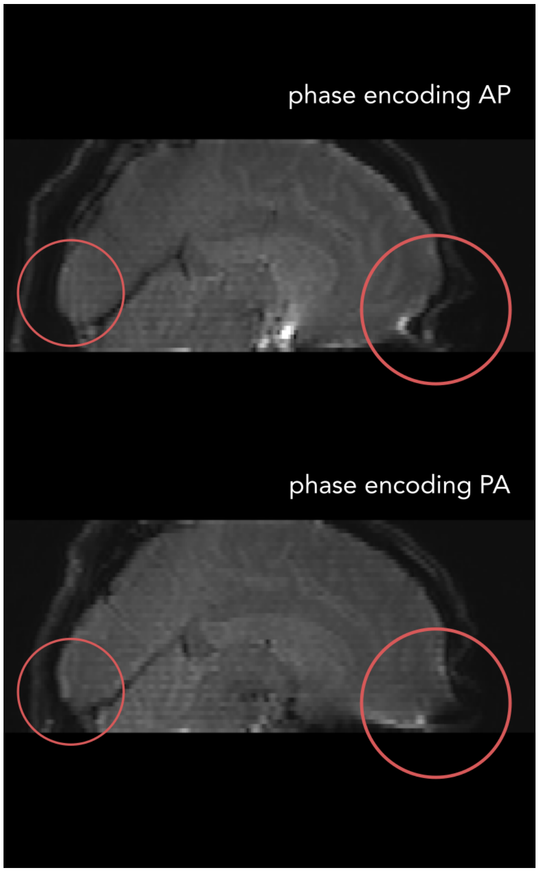

Figure 5.15: Calibration images (sagittal view) acquired from the anterior (top) and posterior (bottom) phase directions for participant 14326. Distortions (red circle) caused from diffusion profiles with different read-outs (phase encoding direction) allows us to infer the underlying field inhomogeneities, using the *topup* command from FSL.

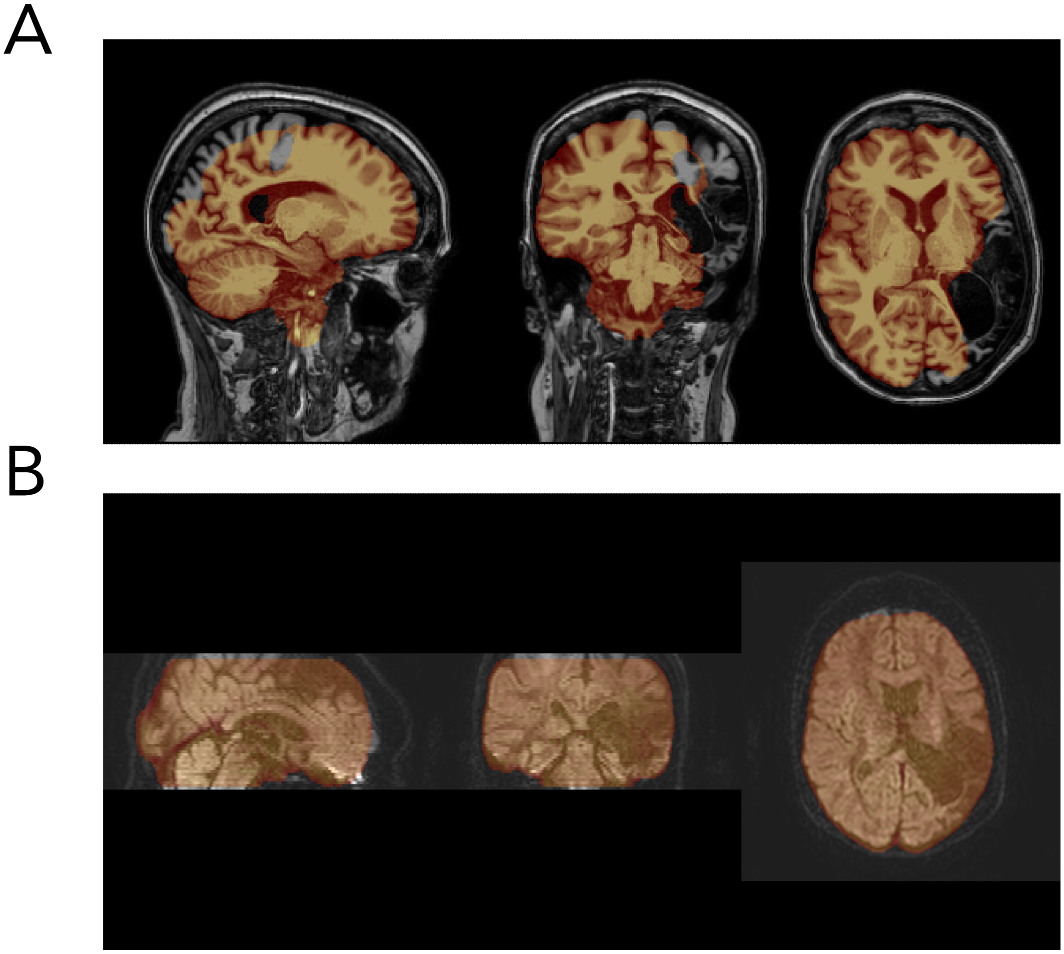

Figure 5.16: Comparisons between skull stripping using BET for the T1-weighted image and diffusion-weighted image for participant 14196.

5.11 Fitting a tensor model

Fitting a tensor model allowed us to quantify the standard diffusion measures often reported in the literature (Cottaar, 2020). These include the three principal diffusion directions (anterior-posterior, dorsal-ventral and left-right), the mean diffusivity and the fractional anisotropy (FA) across each voxel. This is done using the *dtifit* command and using the eddy unwarped images (see 5.10), the brain mask, b-vectors (information of the gradient directions that were applied) and the b-values (size of diffusion gradient applied during each volume).

Figure 5.17 shows an example of a principle diffusion direction map (corresponding to the long axis of the ellipsoid fitted to the diffusion data) modulated by the underlying FA values. This compound map provides information on both level of diffusion anisotropy and the directionality (directions are encoded as combinations of colours: red for right-left, blue for dorsal-ventral, and green for anterior-posterior). The intermediate data produced in this step is then used for use with a probabilistic tractography, explained below, as well as for quantifying white matter intactness in identified tracts in a later analysis step.

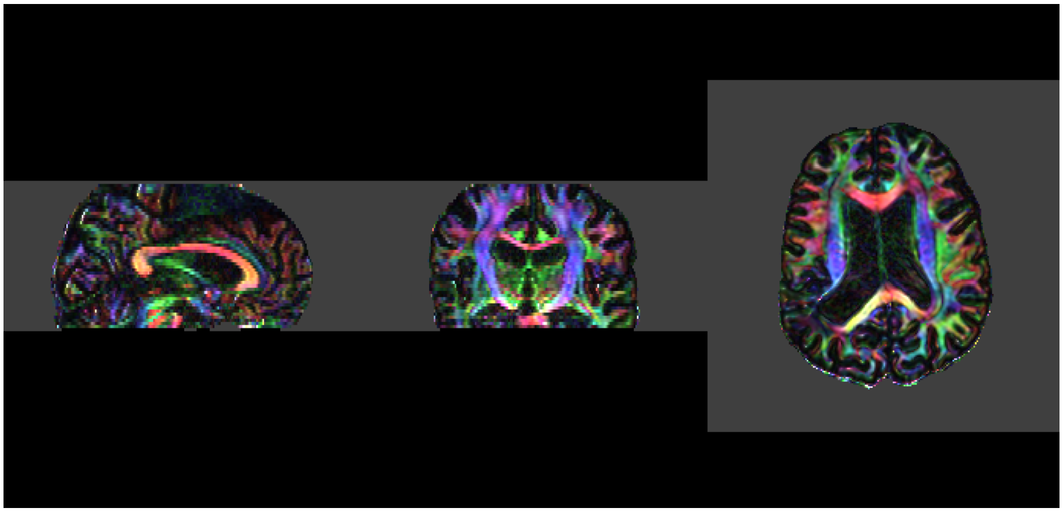

Figure 5.17: Example of FA map with standard RGB color map (red for right-left, blue for dorsal-ventral, and green for anterior-posterior) modulated using the underlying FA values for participant 14326.

5.12 Probabilistic tractography

The principle diffusion direction acquired from DTI analysis provides an estimate of the least restricted diffusion direction, usually assumed to be along the direction of fibre bundles, because of the make-up of axons. By putting together the voxelwise estimates of these diffusion direction, we can estimate and reconstruct the white matter tracts using the principle of streamline tractography (Basser et al., 2000; Mori et al., 1999). Some of the tractography algorithms are deterministic, as they rely on the dominant diffusion direction in each voxel and therefore produce exactly the same streamlines for a given starting point. However, this approach has shortcomings, in particular failing in regions where the diffusion signal provides ambiguous information. I used a probabilistic tractography approach, as implemented in FSL/FDT, which take into account the the direction of the principle eigenvectors (of the tensor), but uses a distribution of possible directions at each voxel, rather than only the most likely one, to calculate a distribution of possible streamlines. The result of this “simulation” provides information about the most likely streamline endpoints, but also a spatial spread of alternatives.

I used the standard “ball and stick” model implemented in *bedpostx* (Bayesian Estimation of Diffusion Parameters Obtained using Sampling Techniques) for estimating the local diffusion parameters and default values with *probtrackx* for probabilistic tractography (Behrens et al., 2007; Behrens et al., 2003).

In addition, I used a tool called *xtract* (De Groot et al., 2013; Warrington et al., 2019), which is a wrapper for *probtrackx* that comes with a curated set of seed, waypoint, and target masks for delineating identified white matter tracts. I used this to trace tracts proximal to the lesion sites in the data: left/right: *optic radiations, vertical occipital fasciculi, dorsal cingulum*, as well as the *forceps major*.

5.13 Diffusion-weighted imaging indicates tract-level damage

To assess white matter integrity at the level of major identified tracts, I used the probabilistic tractography data in combination with the fractional anisotropy measures from the tensor fit. The most relevant tracts for the stroke survivors in this study were those connecting areas within and between the occipital lobes, namely:

- the *vertical occipital fasciculi* (*vof*, left and right),
- the *optic radiations* (*or*, left and right),
- the *dorsal bundles of the cingulum* (*cbd*, left and right).

In addition to these lateralized structures, I also analyzed the *forceps major*, a large bundle connecting the visual areas via the splenium of the corpus callosum.

After computing the microstructural measures using a diffusion tensor fit (*dtifit*), and probabilistic tractography (*bedpostx*) I used an automated method for defining the tracts of interest (*xtract*, see 5.12). Figure 5.18 shows a rendering of those tracts superimposed on the fractional anisotropy (FA) map for participant 14196 (right hemianopia). An extended area of reduced FA is clearly visible in the left hemisphere (compared to the right). This area corresponds to part of the stroke lesion.

Despite the stroke lesion overlapping the *optic radiation* (OR) in the left hemisphere, the probabilistic tractography identified tracts on both sides. It is worth noting that although the left OR looks completely disrupted in the particular section shown (blue label, Figure 5.18), according to the tractorgraphy analysis a bundle was still present, although of a reduced volume: in this participant it measured 8470 mm^3 in the left hemisphere compared to 12254 mm^3 in the right (using the default threshold of 0.001 on the tract probability maps).

To quantify the differences in the underlying microstructure, I computed the mean FA value in the identified tracts and compared the values in the lesioned hemispheres to those in the non-lesioned ones. For all participants, there was a clear reduction in the FA values in the lesioned hemisphere, although the magnitude and pattern of reduction was markedly different across participants (Figure 5.18).

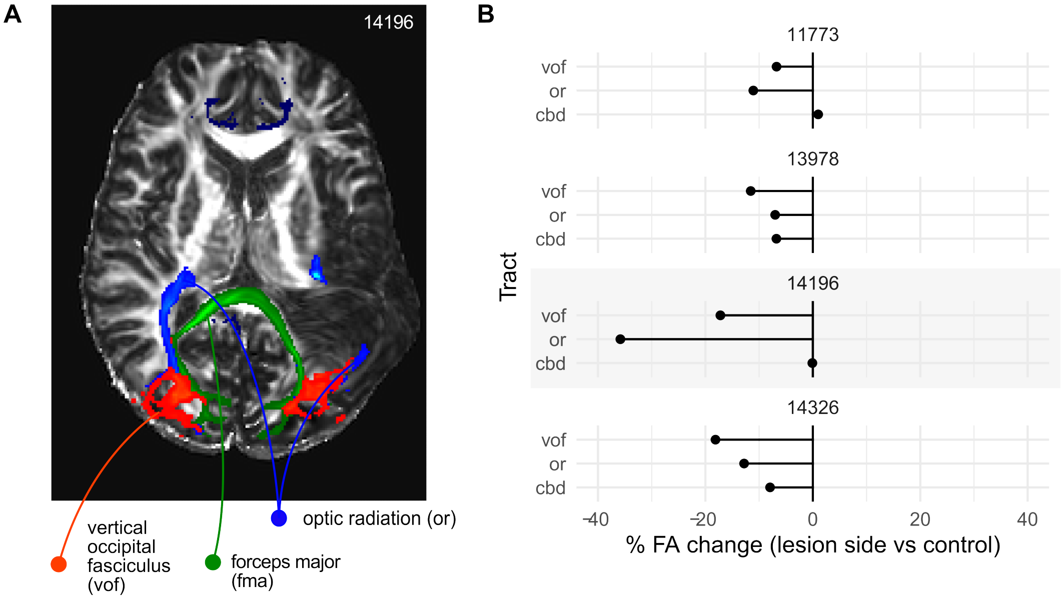

Figure 5.18: White matter intactness, results from diffusion weighted imaging and analysis. (A) White matter tracts identified from diffusion weighted data by probabilistic tractography (*probtrackx*). Blue, optic radiations (left and right); red, vertical occipital fasciculi (left and right); green, forceps major, a large fiber bundle of the corpus callosum connecting visual areas in the left and right hemisphere. Grayscale image, map of fractional anisotropy. (B) Percentage change in fractional anisotropy between the lesioned and non-lesioned hemisphere for *vof*, *or*, and *cbd*. For all participants (sub-panels), there was a clear reduction in the FA values in the lesioned hemisphere up to 40%, although the magnitude and pattern of reduction was markedly different across participants.

Chapter 6

Cross-modal insights

6.1 Overview

This chapter will discuss the results across different imaging modalities and how combinations of measurements may be used to better characterize the lesions and understand the extent of the visual field deficit. The broader, cross-modal picture could provide useful information for establishing participants' potential for rehabilitation, raising interesting directions of approaching restitutive strategies. Here, I highlight some prospective research ideas that can be developed further, in light of the findings presented in this study.

6.2 Mismatches between perimetry and imaging defined responses

It is useful to consider the mismatches between the clinical, static perimetry and imaging defined measures in turn: to (a) lesion definitions from anatomy scans; (b) fMRI derived population receptive field (pRF) maps; (c) any damage in diffusion imaging defined white matter tracts. Each of these measures provides complementary information about the stroke-related damage in the brain. Ultimately, building up a more detailed, multifaceted characterization of stroke lesions in this way will help identify new strategies for rehabilitation.

6.2.1 Perimetry and anatomical MRI

The pattern and extent of cerebral lesions varies substantially across stroke survivors, even in situations where the perimetry-defined visual field loss is remarkably similar. For example, participants 11773 and 14196 in our study, both with hemianopia, have very distinct and different patterns of cerebral lesions, yet a nearly indistinguishable visual field loss. This in itself underscores the value of additional personalised measurements to characterise the patient-specific visual field loss.

Many reports of anatomical lesion definitions of HVFD provide only a cursory outline of the lesion location, pointing to the occipital cortex or the occipital pole (Fujino et al., 1986; Sanchez-Lopez et al., 2020). However, there is a drive for personalised approaches to treatment and constant improvements in imaging technology are likely to facilitate this (Hinman et al., 2016).

Here, I used information from a probabilistic atlas of visual areas (L. Wang et al., 2015) to further subdivide the cortical parts of the stroke lesions. Other cortical atlases and parcellations may provide additional information (van Essen et al., 2019), but the choice of using a probabilistic atlas of visual areas was driven by a similarity in the methodology used to define topographically organised areas, and a growing literature on the functional properties of these areas (Wandell et al., 2007). The definitions of the 25 regions in each hemisphere, alongside which areas are most and least affected by the stroke, suggest particular stimulus categories or “channels” that may be most useful for rehabilitation.

6.2.2 Perimetry and visual responses in functional MRI

Residual visual responses to stimuli presented inside the scotoma were found for all participants. In three out of the four stroke survivors, residual functional activity was robust and in one case (participant 14326) the functional responses were broadly similar to the non-lesioned hemisphere (see Figure 4.13d, 4.14a). For one participant (13978, Figure 4.13b, 4.14a) this pattern was much less clear, but it should be noted that this individual had particularly unstable fixation, as seen in the microperimetry derived measure of fixation stability (BCEA) (see 2.4.3). This has the potential to reduce the reliability of functional maps and in situations where fixation stability is poor, some form of gaze contingent mapping may be beneficial. At present, we do not know whether ocular instability has masked residual cortical activity within the defined region of the scotoma.

6.2.3 Perimetry and diffusion weighted imaging /tractography

Diffusion weighted imaging data was obtained for all participants in the study. By fitting a diffusion tensor model, these data can be used to compute voxel-wise statistics such as *fractional anisotropy* (FA) and *mean diffusivity* (MD) that are sensitive to changes in microstructure. Without much further analysis, these images provide an additional image contrast that can be useful in clearly defining lesion damage (Tae et al., 2018). In addition, I performed probabilistic tractography using tools from FDT (*bedpostx, probtrackx, xtract*). For each participant, the following tracts in the posterior part of the brain were identified: left and right *optic radiations*, left and right *vertical occipital fasciculi*, *forceps major* (connecting visual areas in the left and right hemispheres) as well as the posterior portion of the *cingulum*. To assess white matter integrity, I compared FA values across the lesioned and non-lesioned hemisphere for the identified tracts. Although, perimetry results from participant 11773 and 14196 showed similar patterns of visual field deficit (complete right hemianopia), the FA reduction of the in the lesioned hemisphere (most notably the *optic radiation*) is more pronounced in participant 14196 — which imply higher levels of tissue damage. This could potentially explain why we observe more functional responses in the 'blind' field in participant 11773 compared to 14196, and warrants further investigation.

6.3 Potential sites for rehabilitation and optimal stimuli for perceptual learning

The use of perceptual learning paradigms rely on the individual's capacity to relay relevant information about the stimulus from the retina to visual cortex (Horton et al., 2017). If the cortex, or the connecting white matter tracts are completely lost, any changes in visual function, or recovery inside the scotoma cannot be expected. Therefore, to maximise potential success of any rehabilitation approach it is important to identify strategies that are consistent with individual physiology. In order to do this, two pieces of information are crucial: 1) the locations of any sparing in the visual field and 2) which functional/anatomical regions are partially or fully intact. This information could be used to guide a personalised approach to where in the visual field training should occur, say, a patch extending from the fovea to a known eccentricity in the lower left quadrant, which was identified during fMRI mapping.

Importantly, the information about spared anatomical regions (or even functional subdivisions) suggests a class of stimuli or tasks that might provide the largest responses, and therefore present the most likely route to rehabilitation. If we consider the field loss revealed by perimetry in terms of topographically mapped regions, then the use of imaging allows the measurement of other "down-stream" loss maps in the post-stroke brain, which may look quite different. Recovery of lost topographic information due to damage in early visual cortex is less plausible (Horton et al., 2017), but if the loss map for regions that prefer e.g. colour, motion, or faces are less affected, then subjects may be able to ‘learn’ how to exploit this information in the residual field to support visual behaviours. In some ways, this is akin to the problems introduced by retinal or cortical implants for vision restoration. In that situation, the device introduces distortions and lossy information about the image, but patients can re-learn to use this new input for a range of visual behaviours (for discussion see Beyeler et al. (2017)).

For example, if ventral regions are relatively spared compared to dorsal regions, then a training programme based on objects, faces, and other stimuli preferentially processed in these regions suggests itself (Grill-Spector, 2003; Kanwisher et al., 1997). The location for visual rehabilitation in the affected visual field should be guided by where (functional) responses can be elicited and then further enhanced by training. This may include areas of the visual field with “functional MRI-defined blindsight” – declared by perimetry to be non-functioning but responding in the fMRI experiment. Additionally, they may also include a more fine-grained definition of areas appearing as *spared* in perimetry, but not well-defined due to the relatively coarse spatial scale of perimetry.

By way of example, consider the imaging results from participant 11773 (right hemianopia). Residual functional activity within the scotoma, measured across different visual areas, represents the lower right quadrant of the visual field. I propose that restitutive approaches should target this location for perceptual training. The ROIs labelled as contributing to this residual function point towards the class of stimuli that might be most suitable. For example, there is good evidence that V3 is sensitive to chromatic- and luminance-defined motion stimuli (Gegenfurtner et al., 1997; McKeefry et al., 2010). To recruit this part of cortex, therefore, perceptual learning based training using moving chromatic and luminance grating stimuli in locations where we still find residual visual function in the 'blind' field may be most appropriate.

This principle could be applied for other ROIs identified in this way, such as *LO1* and *IPS0*, though visual pRFs representing the scotoma that were defined with standard retinotopy stimuli may be less efficient at driving higher level regions differentially (Yildirim et al., 2018). In addition, the distribution of residual function may vary substantially among other stroke survivors. An interesting question for future work would be to test whether the least complex stimuli consistent with residual function (such as oriented or, curvature defined stimuli) or more complex stimuli (such as faces, objects, etc) are stronger drivers for rehabilitation.

Ultimately, restitutive approaches are perceptually challenging and require a significant time commitment from stroke survivors – often long hours training on a computer display are required. To ensure the best chance of success and to improve training compliance, it's important to establish a protocol that is guided by the individual functional activity pattern, using stimuli that the patient's visual brain can potentially learn to respond to.

6.4 Conclusions

Multi-modal imaging in stroke survivors provides informative data on both the lesion and spared functional regions in visual cortex for a relatively small time commitment and cost. The scanning protocol used here took only *one hour* for data acquisition (*90 minutes* including setup). We believe our approach could particularly inform perceptual learning-based rehabilitation, by enabling the targeting of specific visual field locations and selecting the most optimal class of stimuli. The current work shows that different individuals might benefit from rehabilitation that targets a specific set of downstream cortical regions. Crucially, detailed mapping in this way could also serve to inform clinicians to direct stroke survivors to other rehabilitation approaches, if imaging-based mapping reveals that no residual function is measurable across the majority of visual areas in the lesioned hemisphere.

It is important to note that other imaging approaches could yield useful, complementary information. Therefore, a larger scale study with more patients, different levels of damage to cortex and using a broader set of imaging modalities based on MR or MEG (see e.g. Kupers et al. (2021)) would be very timely. The emphasis here is to establish methodologies for identifying and clearly defining parts of the post-stroke brain that retain the potential to support some usable visual function.

Chapter 7

Simulated Hemianopia

7.1 Overview

This chapter will explore how homonymous visual field defects can be simulated in healthy participants and how this could allow the development of methods to study recovery from HVFD in stroke survivors. The particular emphasis of this experiment is on how recovery of visual sensitivity in the blind field might impact reading performance. To address this question behaviourally, I employed a gaze contingent paradigm and manipulated the degree of spatial blurring in one hemifield to simulate hemianopic loss (and potential recovery). I then measured how these manipulations changed oculomotor behaviour during text reading. At high levels of blurring, visual information fundamental to text recognition and comprehension is no longer available (Kwon & Legge, 2012). I argue that this can be used to functionally simulate the effects of vision loss in each hemifield. By manipulating the degree of blurring, I systematically controlled access to spatial information in one hemifield and measured how this changed both the pattern of eye movements and reading speed.

Because reading ability changes with age (for a detailed summary see Laubrock et al. (2006))) and the effects of spatially blurring text may differentially impact eye movement characteristics in younger and older subjects, I recruited two groups of observers – one with younger participants, another with older participants. The second group was chosen to be closer in age to the risk group for ischaemic strokes (England, 2018). Findings from this study open up the possibility of using participants with normal visual function to help identify the most promising strategies for HVFD, before translation to patient groups.

7.2 Materials and methods

7.2.1 Participants

I recruited 15 young adult participants (mean age is 20.9 yrs) and 15 participants for an older control group (mean age is 54.7 yrs). For the control group, I recruited between ages 40 and 70. This age bracket was informed by stroke incidence rates, indicating that 97% of estimated stroke incidence occurs above the age of 40 (England, 2018). Data from 1 participant in the young adult group was excluded, as it was incomplete. The young adults were recruited from the student population at the University of Nottingham, while the older group were recruited through local communities in Nottingham. The inclusion criteria for participation in the study were: 1) normal or corrected to normal vision; 2) no history of a stroke; 3) formally educated in the English language. Experiments were approved by the School of Psychology Ethics committee and all participants provided informed, written consent.

7.2.2 Reading stimuli

The text stimuli used in the reading task were based on paragraphs from the *International Reading Speed Test* (iRest, Trauzettel-Klosinski et al. (2012)). The paragraphs in that test are standardised in terms of length, difficulty, and linguistic complexity and have previously been used to assess reading performance in individuals with low vision (Kortuem et al., 2021; Mathews et al., 2017; Ramulu et al., 2013).

The text stimuli were displayed on a gamma-corrected CRT monitor (resolution: 1024x768, screen width = 40.6cm, refresh rate: 85Hz) using custom software written in Python/PsychoPy (Peirce, 2007). Text was displayed using the Arial font and the individual letters were sized such that the vertical size of the letter ‘x’ (x-height) was at 0.4 logMAR (0.21°). Initial pilot testing showed this to be a comfortable text size for reading paragraphs. The viewing distance was set to 114 cm and text was rendered in white on a grey background (root mean square contrast: 0.2, Weber contrast: 1.0).

In total, I used 10 different paragraphs, one of which was randomly selected for an initial practice trial and excluded from the final analysis. The total number of words in the paragraphs ranged from 136 to 166 (mean number, 154). The average number of words in a single line was 9.7 and the vertical spacing between lines was 0.25°. All but one of the text stimuli contained 16 lines in one paragraph (one having 15 lines). To avoid order effects, the sequence of text displayed was randomised across individuals. Participants were instructed to read the text silently and to signal when they had finished reading by pressing the ‘space‘ key.

7.2.3 Eye tracking and gaze contingent viewing

Eye positions and movements were recorded monocularly (right eye) with an Eyelink 1000 infrared eye tracker (SR Research Ltd., Ottawa) at a sample rate of 500 Hz. A 9-point fixation grid was used to calibrate the eye tracker at the start of every trial. Calibration was repeated if fixation to any point had an error of 1° or higher. The eye level of participants was set to the centre of the screen with their chin firmly resting on a chin rest.

To simulate visual field loss in one of the hemifields (left or right), the text image was blurred towards the left or right side of the screen with respect to the current eye position. To achieve this gaze-contingent display, I combined the original (unblurred) text image with a blurred version which was revealed with a moving “aperture” through alpha-blending. This aperture was constructed to reveal a particular side of the screen with respect to fixation, as seen in Figure 7.2. The screen position of the aperture was updated every 100ms to reduce the effect of high temporal frequency noise in the eye position measurements.

To blur the text stimuli used in this display, I applied a 10th order Butterworth low pass filter (Kwon & Legge, 2012). The filter is described by the following function:

$$f = \frac{1}{1 + (\frac{r}{c})^{2n}}$$

where r is the spatial frequency, c is the low-pass cut-off spatial frequency, and n is the filter order.

The cut-off frequency of the filter was set at different multiples of the Nyquist frequencies: 1, 0.2, 0.15, 0.1, and 0.05 (see Figure 7.1). The lower the cut-off frequency of the pass band, the more blurred the text appeared. Using the pixel width of the letter ‘x’ as a baseline (11 pixels / 0.22° wide, in the display), the cut-off frequencies can also be translated into units of *cycles per letter*. The values corresponded to 5.5 (unfiltered), 1.1, 0.825, 0.55, 0.275 cycles per letter (cpl). Examples of the blurred stimuli are shown in Figure 7.2. The selection of this particular set of blurring values was based on pilot measurements to establish a suitable range of reading performances, while keeping the number of testing conditions manageable. Participants across both age groups (between-subjects factor) were subjected to both left and right simulated HVFD conditions across all blurring levels, in addition to the control conditions (within-subject factor).

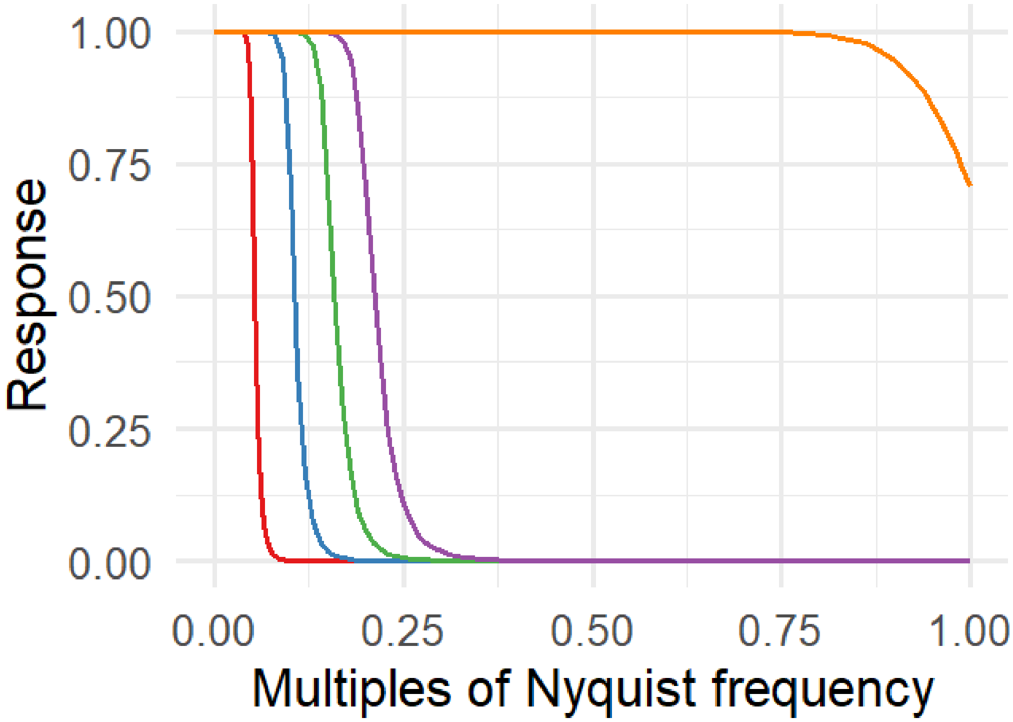

Figure 7.1: Response function of the 10th order Butterworth filter at various frequencies (1, 0.2, 0.15, 0.1, and 0.05). These cut-off frequencies translate to 5.5, 1.1, 0.825, 0.55, 0.275 *cycles per letter* at 0.22° letter size.

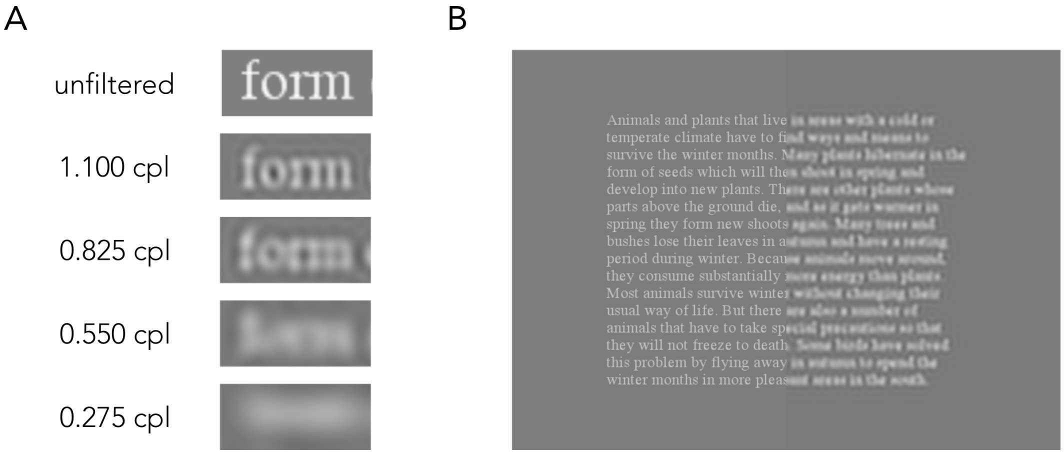

Figure 7.2: Example of gaze contingent blurring on the text stimuli. (A) Example of the word ‘form’ at different blurring levels using the cut-off frequency thresholds indicated (cpl, cycles per letter). (B) Visualisation of the partially blurred paragraph of text (here, blurred on the right side with respect to the current eye position, approximately in the centre of the display).

7.2.4 Procedure

The day before the experiment, participants were told that the task involved reading and were asked to wear any corrective lenses they would normally use when reading at home. Participants were briefed to wear prescription contact lenses if available to correct for any myopia. However, across both groups of participants, only 5 wore corrective spectacle lenses and the other 25 did not require any vision correction. All participants had normal, or corrected to normal, distance visual acuity (Bailey-Lovie chart) and could comfortably read the text at the presented size (equivalent to 0.4 logMAR). For those wearing glasses, we did not find any detrimental effects on eye tracking.

At the start of the experiment, participants were instructed to position themselves comfortably using the chin and forehead rest. The eye tracker was then adjusted to provide an optimum view of the right eye. Participants were instructed to silently read through the entire paragraph at their normal reading pace. They were also told to move on to the next word if they were struggling to read any particular words. When they finished reading, they terminated the trial by pressing the ‘space‘ key. As participants reported the simulated vision loss to be quite unusual when first applied, we made sure to include several training blocks using the sample text (at the highest blurring level) until they were comfortable finishing the paragraph.

7.3 Raw eye movement traces

To illustrate the patterns of eye movement we observed across the different conditions, samples of raw eye traces are shown in Figure 7.3. The plots show the horizontal component of the eye movements (x-coordinate) as a function of time for the beginning of example trials. The three panels show traces for a control trial (no blurring, *top*), one for simulated right homonymous visual field defect (HVFD, *middle*), and a third for the corresponding left HVFD condition (*bottom*). Pixel coordinates [0, 0] refer to the centre of the screen, positive x-coordinates refer to the right side of the screen (negative values to the left); positive y coordinates refer to the top part of the screen (negative values to the bottom).

Normal reading behaviour, as seen for the control condition, results in a typical, repeating staircase pattern of the x-coordinates: the participant fixates on a word for a short period, then promptly moves to the next, until the end of the line is reached. The search for the start of the new line is indicated by the large displacement, eye position changes from -200 to +200 in pixel coordinates along the x-axis. Note that the duration of a single staircase pattern can be used to quantify the time taken for a participant to read one line of text. The data from a simulated *left* HVFD condition looks similar to the control condition, however, the corresponding simulated *right* HVFD produces a much more variable pattern of eye movements. It is also apparent that a higher number of saccades are being made as the reader progresses through the text. As a result, the participants took longer to complete each line. In the example shown here, the time to complete a line in the slowest condition is about four times that of the control condition.

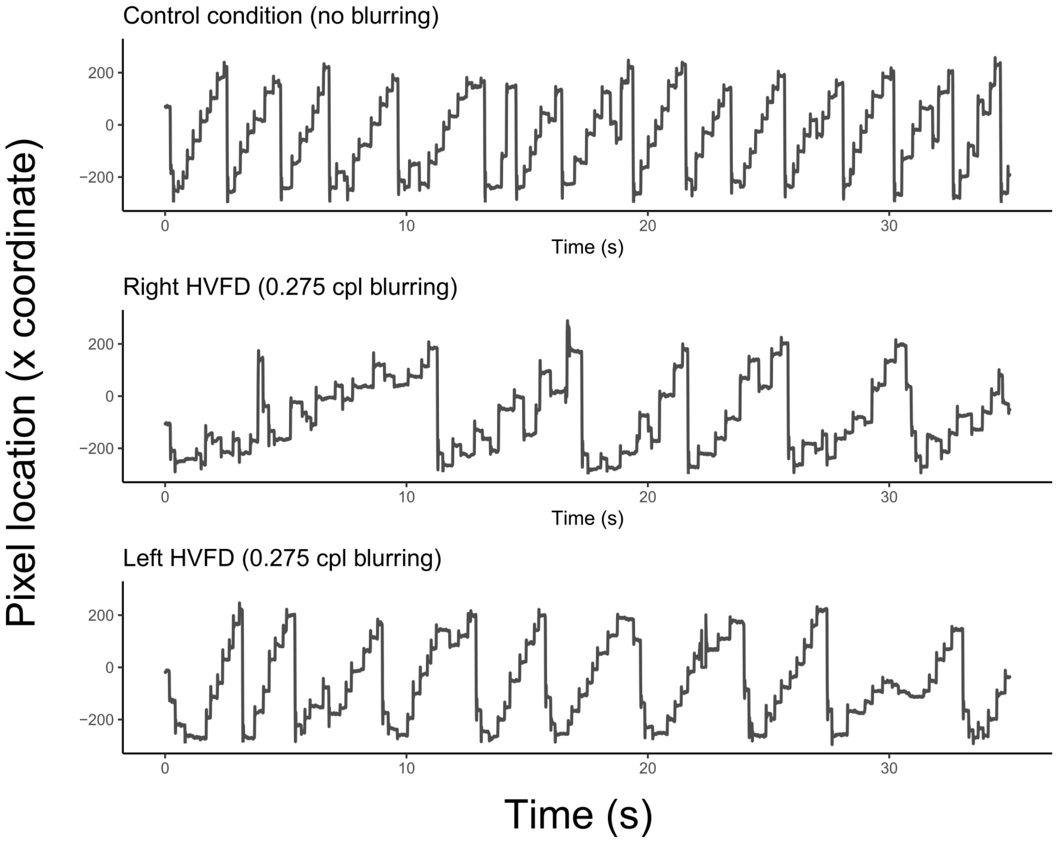

Figure 7.3: Samples of raw eye traces along the x-coordinate domain (pixels) in an experiment trial for control (top), right simulated HVFD - 0.275 cpl blurring (middle) and left simulated HVFD - 0.275 cpl blurring (bottom). Note that the figure only depicts eye traces up to 35s for all conditions and does not represent the entire trial for some conditions. Lateral eye movement patterns resemble a staircase-like pattern when reading a paragraph, where each step is a fixation and a forward saccade would move the staircase upwards and a regressive saccade would move the staircase downwards. The staircase would then ‘reset’ when the line is complete and the reader is moving on to the next line. In some conditions there is a jitter before resetting as readers struggle to fixate on the first word of the next line.

7.4 Adaptive velocity-based algorithm

Some algorithms for classifying fixations and saccades only use a single velocity threshold. Because this study actively impairs normal reading behaviour and there was a large age range across participants, I anticipated larger variance in the eye movement patterns and higher levels of variability across participants and trial conditions. To accommodate this, I employed an adaptive velocity-based algorithm (Nyström & Holmqvist, 2010). This data-driven approach has been shown to be less sensitive to the effects of noise and better suited than other commonly used algorithms for detecting both fixations, saccades (and also glissades[1]) (Nyström & Holmqvist, 2010).

7.4.1 Key parameters

To classify eye events, we use 3 parameters [x, y, t], representing the eye position on the screen and the time, to derive the velocity and acceleration across eye position samples:

---

[1] It should be noted that this study does not use ‘glissades’ – a post-saccadic eye movement that is believed to realign the eye position before fixation (Nyström & Holmqvist, 2010), in the analysis. As the classification of glissades does not disrupt the classification of fixations and saccades, no changes were made to algorithm.

$$\text{velocity} = \frac{\sqrt{(x_{n+1} - x_n)^2 + (y_{n+1} - y_n)^2}}{t}$$

$$\text{acceleration} = \frac{\text{velocity}_{n+1} - \text{velocity}_n}{t}$$

Note that, because we are taking finite differences, the number of samples are n-1 for velocity and n-2 for acceleration
respectively.

7.4.2 Filtering and denoising

Calculating the velocity and acceleration from sample to sample using finite differences can lead to noisy estimates. Small fluctuations in gaze samples, which can be caused by a combination of factors: optical artefacts; mechanical or electromagnetic disturbances during recording; rounding errors, result in noisy signals. These are further exacerbated in the first derivative over time (velocity) and second derivative (acceleration). To address this issue, I used the Savitzky Golay finite impulse response filter, SG-FIR (Savitzky & Golay, 1964) to smooth the data. This filter has the advantage of retaining high-frequency detail across the signal along with key information about the local maxima and minima in the data, while making no strong assumption on the velocity profiles.

The Savitzky-Golay-FIR models a polynomial function that best fits a set of samples across the signal. It is defined by 2 parameters, the filter order – which determines the degree of the fitted polynomial function, and the filter length – which determines the size of the window of samples. Similarly to Nyström and Holmqvist (2010), the filter order was set to 2 and the filter length was set to 10 samples (2 x minimum saccade duration, 10ms). Figure 7.4 shows a comparison of the unfiltered data against the SG-FIR filtered data for a selected interval of the data, across the x-coordinate (position as a function of time), eye movement velocity (as a function of time) and eye movement acceleration (as a function of time). The filtered signal allows us to precisely capture important eye position changes while smoothing noisy parts of the data.

Prior to this filtering, blinks and physiologically impossible samples were also removed from the data (velocity > 1000°/sec, acceleration > $100000°/\text{sec}^2$.

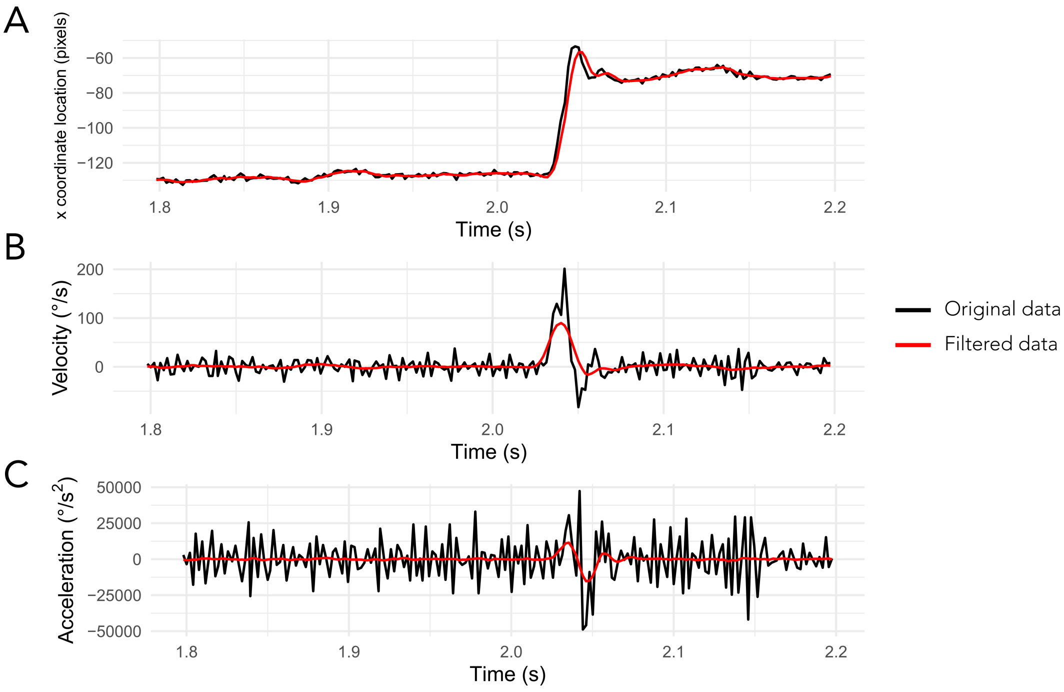

Figure 7.4: Comparing unfiltered data against Savitzky-Golay filtered data. A small interval of the eye tracking data was selected to demonstrate the filter under different profiles: (A) x-coordinate change, (B) eye movement velocity and (C) eye movement acceleration. The black line represents the original data while the red line represents the filtered data. The Savitzky-Golay filter order was set to 2 and the filter length to 10 samples (2 x the minimum saccade duration, 10 ms). Note that when tracking the x-coordinate change, the shift in eye position comes slightly after the 2.0s, which can also be seen in the velocity and acceleration profiles. However in the unfiltered data, the velocity and acceleration profiles seem to be noisy before and after the actual eye movement, largely due to small fluctuations in the raw gaze samples. The filtered data succeeds in filtering the noise and capturing important eye movement changes.

7.4.3 Velocity Threshold Estimation

Velocity-based classification of eye events traditionally uses a fixed velocity threshold to identify fixations and saccades (Salvucci & Goldberg, 2000). However, as mentioned previously, I anticipate large variance in eye movement patterns across participants and trials. If the fixed velocity threshold is set too high, short saccades may be dismissed as noise, whereas if it is set too low, some fixations may be incorrectly detected as saccades. Hence, the use of a variable velocity threshold produces more reliable eye event detection.

To run the velocity threshold estimation, an initial velocity threshold, PT_1 is set at 100°/sec. For a given dataset, all eye movement velocity samples below PT_1 are tabulated. From this set of samples, I calculate the mean (μ) and standard deviation (σ). The velocity threshold is then updated as follows:

$$PT_n = \mu_n + 6\sigma_{n-1}$$

This process is performed iteratively until the latest velocity threshold, PT_n is less than $1°$/sec from the previous velocity threshold, PT_{n-1}. This allows the velocity threshold to converge to a threshold low enough to detect as many saccades as the variance in the velocity samples will allow, without compromising any false positive detection of saccades in datasets with a high noise level. This particular method of thresholding has been shown to robustly detect saccades across individuals with large variances in eye movement patterns (Nyström & Holmqvist, 2010). Figure 7.5 shows examples of the final velocity threshold across participants with different levels of noise in their eye movement velocity profiles.

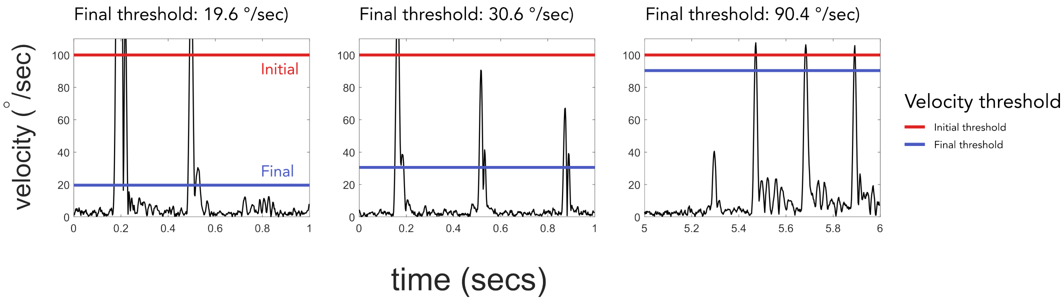

Figure 7.5: Examples of velocity threshold estimation across participants with different levels of noise in their eye movement velocity profiles. The final velocity threshold converges to a threshold low enough to detect as many saccades as the variance in the velocity samples would allow, without compromising any false positive detection of saccades in datasets with a high noise level. Note the large difference in final velocity threshold estimation across the left (19.6 °/sec) and right (90.4 °/sec) velocity profiles. The algorithm effectively captures saccadic movements while ignoring noisy eye movement data.

7.4.4 Saccade detection

After arriving at a suitable velocity threshold, PT_n, the algorithm searches for both the onset and offset of the saccade peaks. From the peak, it searches leftwards (backwards in time) for the onset and rightwards (forwards in time) for the offset.

The *saccadic onset* is determined by the first sample that has met two requirements: (i) having a velocity below the *saccade onset threshold* $(\mu + 3\sigma)$; (ii) the current velocity sample is *higher* or *equal* to the next velocity sample in time $(Velocity_n - Velocity_{n+1} \geq 0)$. Operationally, the algorithm attempts to find the first local minima that is below the *saccade onset threshold*.

The *saccadic offset threshold* is determined by the weighted combination of the global noise and locally adaptive noise. For the locally adaptive noise factor, it is derived using a window of samples that precedes the saccade, where the size of the window is defined by the minimum allowed fixation duration (40 ms). This approach allows the algorithm to manage local variation in noise across saccades, which could arise from individual differences – shape of eyelashes or presence of corrective lenses (Duchowski & Duchowski, 2017; Nyström & Holmqvist, 2010). The global noise factor is determined by [α x *saccade onset threshold*] while the locally adaptive noise factor is determined by [β x $(\mu_{local} + 3\sigma_{local})$], where α and β are set at 0.7 and 0.3 respectively. In a similar fashion to detecting saccadic onsets, the saccadic offset is determined by the first sample that has met two requirements: (i) having a velocity below the *saccade offset threshold* $(\alpha \ onset_{threshold} + \beta \ (\mu_{local} + 3\sigma_{local})$; (ii) the current velocity sample is lower or equal to the next velocity sample in time $(Velocity_n - Velocity_{n+1} \leq 0)$.

In addition to these steps, any saccades smaller than 10 ms are removed. Figure 7.6 shows an example of saccade detection using the algorithm.

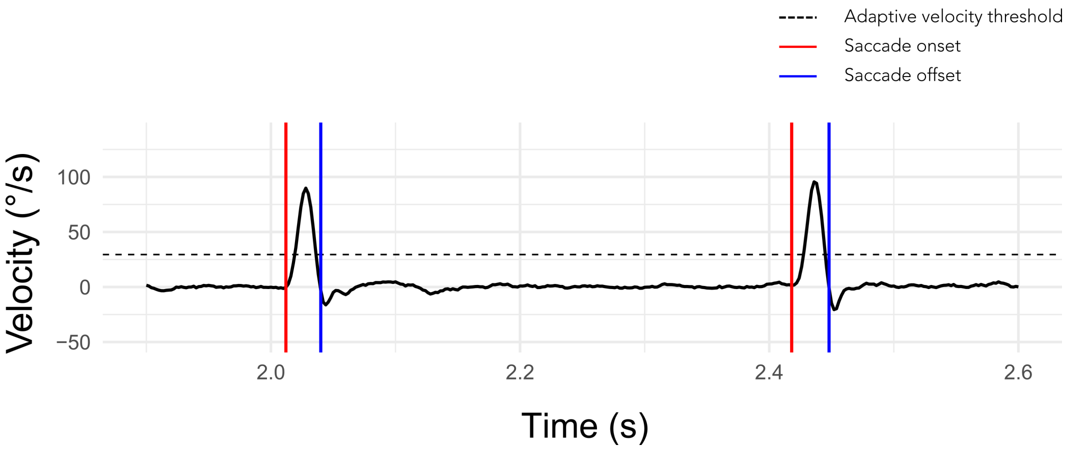

Figure 7.6: Detecting saccades using adaptive event detection algorithm. The figures shows a specific interval of the (unfiltered) velocity plot from the eye tracking data. The horizontal dotted line represents the adaptive velocity threshold, derived using the velocity threshold estimation, accounting for the variable noise across participants and trials. The red line represents the *saccade onset* (when the saccade starts), which is the first local minima below the *saccadic onset threshold*. The blue line represents the *saccade offset* (when the saccade ends), which uses the weighted combination of the *global* and *locally adaptive* noise in the data to find the first local minima below the *saccadic offset threshold*.

7.4.5 Glissade detection

Although glissades are not used in the analysis, it is still important to classify these events. Glissade durations may be misclassified by the algorithm as extremely small fixations, or may extend the average saccade duration by up to 25% (Nyström & Holmqvist, 2010). Hence, I will briefly discuss how glissades are classified. Glissades are separated into two categories: high velocity and low velocity glissades. The high velocity glissade is detected by using a window (set by the minimum fixation duration – 40 ms) after the saccadic offset and if any sample is raised above the peak saccade threshold PT_n whereas the low velocity glissades is uses the same window but it only requires the sample to raise above the *saccade* *offset threshold* defined by the preceding saccade. The *glissade onset* is determine using the offset of the preceding saccade whereas the *glissade offset* is defined as the first sample to reach a local minima, moving forward in time $(Velocity_n - Velocity_{n+1} \leq 0)$.

7.4.6 Fixation detection

Finally, fixations are defined if a sample is not labelled as a saccade, glissade or noise. Fixation windows below the minimum fixation duration (40 ms) are removed. Commonly, the minimum fixation duration is set at a higher value, 100-200 ms (Holmqvist et al., 2011; Salvucci & Goldberg, 2000). However, there is evidence that shorter fixations are a marker for high mental workload (Ehmke & Wilson, 2007; Unema & Rötting, 1990), which I anticipated could be a possible feature in the samples given how the hemianopic filter creates a difficult reading environment. Additionally, the original paper for the adaptive velocity-based algorithm has shown that it performs well in identifying fixations using this minimum duration (for a more in depth review, see Nyström and Holmqvist (2010)).

7.4.7 Manual data quality control

After running the adaptive velocity-based algorithm, I performed a visual quality check of the eye traces for each trial to ensure data quality. Samples of these traces, visualised on to the text stimuli, can be seen in Figure 7.7.

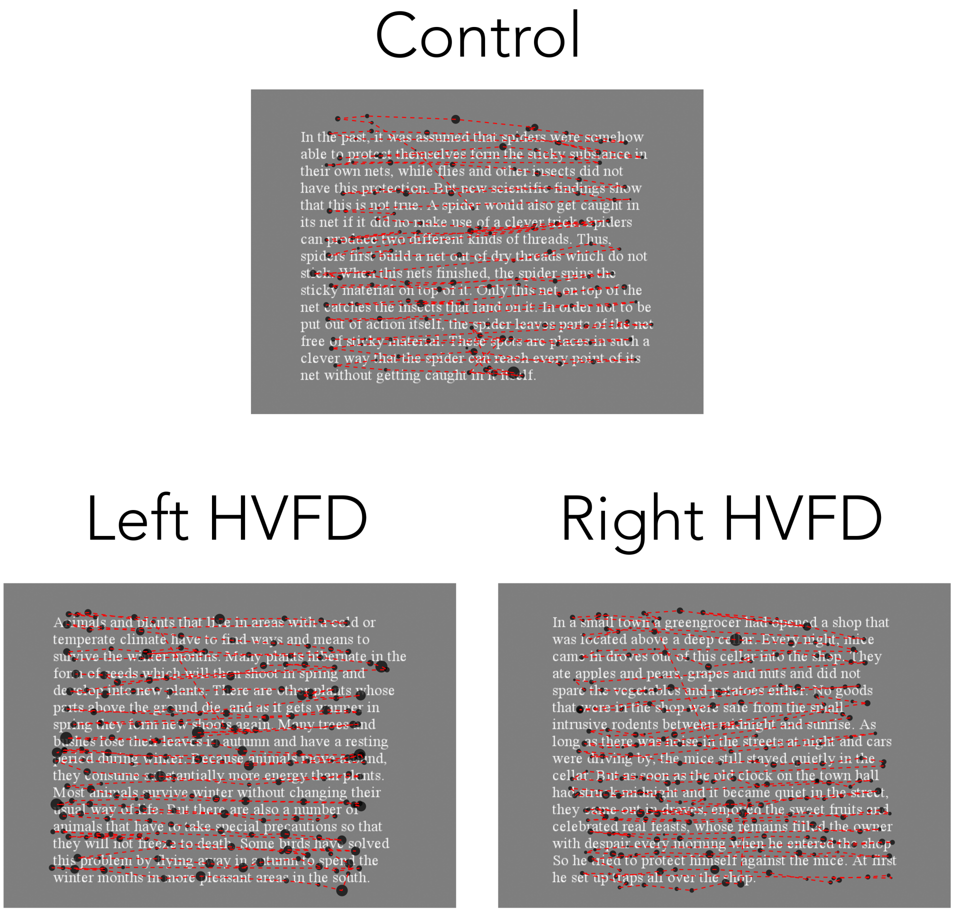

Control

In the past, it was assumed that spiders were somehow able to protect themselves form the sticky substance in their own nets, while flies and other insects did not have this protection. But new scientific findings show that this is not true. A spider would also get caught in its net if it did no make use of a clever trick. Spiders can produce two different kinds of threads. Thus, spiders first build a net out of dry threads which do not stick. When this nets finished, the spider spins the sticky material on top of it. Only this net on top of the net catches the insects that land on it. In order not to be put out of action itself, the spider leaves parts of the net free of sticky material. These spots are places in such a clever way that the spider can reach every point of its net without getting caught in it itself.

Left HVFD

Animals and plants that live in areas with a cold or temperate climate have to find ways and means to survive the winter months. Many plants hibernate in the form of seeds which will then shoot in spring and develop into new plants. There are other plants whose parts above the ground die, and as it gets warmer in spring they form new shoots again. Many trees and bushes lose their leaves in autumn and have a resting period during winter. Because animals move around, they consume substantially more energy than plants. Most animals survive winter without changing their usual way of life. But there are also a number of animals that have to take special precautions so that they will not freeze to death. Some birds have solved this problem by flying away in autumn to spend the winter months in more pleasant areas in the south.

Right HVFD

In a small town a greengrocer had opened a shop that was located above a deep cellar. Every night, mice came in droves out of this cellar into the shop. They ate apples and pears, grapes and nuts and did not spare the vegetables and potatoes either. No goods that were in the shop were safe from the small intrusive rodents between midnight and sunrise. As long as there was noise in the streets at night and cars were driving by, the mice still stayed quietly in the cellar. But as soon as the old clock on the town hall had struck midnight and it became quiet in the street, they came out in droves, enjoyed the sweet fruits and celebrated real feasts, whose remains filled the owner with despair every morning when he entered the shop So he tried to protect himself against the mice. At first he set up traps all over the shop.

Figure 7.7: Sample of eye traces for the control - unfiltered condition (top), simulated left HVFD condition - 0.275 cpl blurring (bottom left) and simulated right HVFD condition - 0.275 cpl blurring (bottom right) overlaid on the respective text image. The black circles are plotted on fixation positions and larger sizes indicate longer fixation durations, the red dashes between the black circles are the saccade direction.

7.5 Dynamic Time Warping

The following variables were derived from the eye events and used in further analysis:

- *number of fixation per line*,
- *number of forward saccades per line*
- *number of regressive saccades per line* (saccades that were in the opposite direction to the reading direction),
- *number of saccades made during return sweep* (any additional saccades from the final fixation to the new line),
- *average median fixation duration* and
- *average median forward saccade amplitude*.

To quantify the number of oculometric events per line, I developed a new method that can reliably mark the first and last fixation made on a line. While the raw eye trace and the labelled trace for fixations itself provides some indication of where refixation to the new line occurs, simple manual segmentation of the events is prone to error. Furthermore, using the y-coordinate to determine a line change is unreliable in noisier datasets. Here, I used *dynamic time warping* – an algorithm which non-linearly matches two signals in time (Sakoe & Chiba, 1978). Although reading speed varies across people, the overall pattern of eye movements will inevitably be similar given the fixed number of lines in a paragraph, as seen in Figure 7.3. Therefore, I could construct a prediction of the expected eye movement patterns, particularly for the x-coordinates. By warping this signal to match each individual trial, I could efficiently identify the *start* and the *end* of the line across different reading speeds. First, I created a simplified 'design' matrix of the expected eye movement pattern over time and warped it onto the original dataset to find the first and last fixations for each line in the paragraphs. This process was then automated across each trial, adapting to different patterns of eye movements for each of the blurring conditions.

A sample of the dynamic time warping process can be seen in Figure 7.8. In Figure 7.8a, I have classified fixation points (*black circle*) using the adaptive velocity-based algorithm and plotted it over the eye traces (*red dashes*). Plotting only the fixation starting points over the entire trial provides a simplified view of the data (Figure 7.8b), which clearly shows some segments of the eye movement recordings with an increased number of saccades. The 'design' matrix for the expected eye movement pattern for the text stimuli can be seen in Figure 7.8c: increasing values for the screen x-coordinates from left to right in a number (n=5) steps in a regular staircase pattern, ending with a reset to the left which includes a short jitter to account for any additional saccade to find the new line. To reduce the number of local mismatches, I chose 5 equally spaced steps to reflect the average number of saccades per line in a typical trial.

The result of the dynamic time warping (the design matrix matched onto the original time series) captured the timing of the overall pattern of eye movements accurately as seen in Figure 7.8d. In turn, this allowed us to accurately estimate the start (*green circle*) and end (*red circle*) of a line as seen in Figure 7.8e. Using these markers, I can calculate (per line) the number and amplitude of (1) forward saccades, (2) regressive saccades, (3) saccades made during the return sweep. For further analysis, the median value of fixation durations and forward saccade amplitudes were estimated across each line and averaged for each subject.

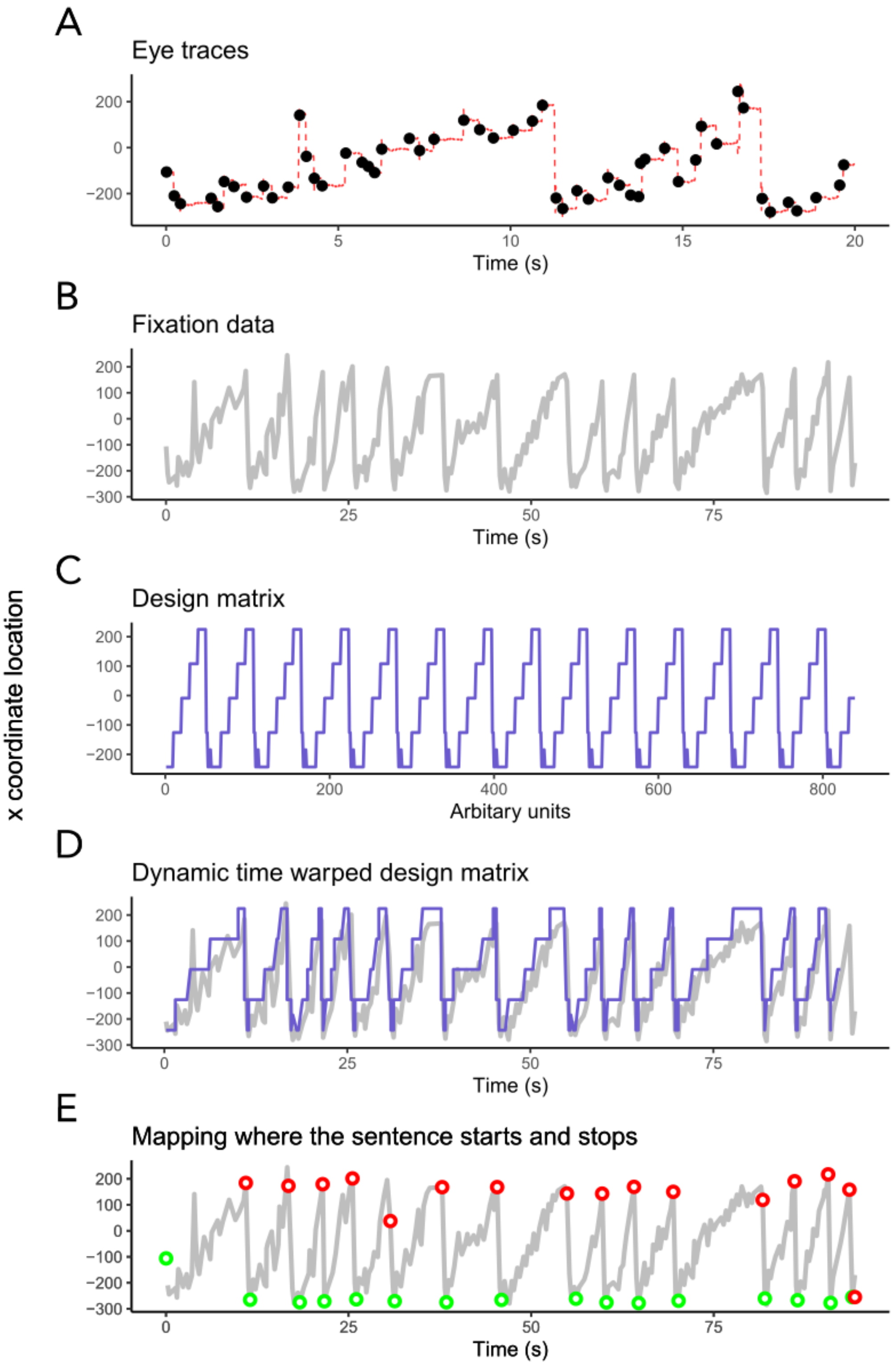
A
Eye traces
200
0
−200
0
5
10
15
20
Time (s)
B
Fixation data
200
100
0
−100
−200
−300
0
25
50
75
Time (s)
C
Design matrix
200
100
0
−100
−200
0
200
400
600
800
Arbitary units
D
Dynamic time warped design matrix
200
100
0
−100
−200
−300
0
25
50
75
Time (s)
E
Mapping where the sentence starts and stops
200
100
0
−100
−200
−300
0
25
50
75
Time (s)
x coordinate location

Figure 7.8: Using dynamic time warping to mark first and final fixation on a line. (A) A segment of the raw eye traces from a single trial from the right HVFD condition with cut-off frequency of 0.275 cpl (red dashes) with fixation points (black circles) plotted over them. (B) Fixation points plotted as a line plot across the entire trial. (C) The design matrix of the expected eye movement patterns. (D) The time warped design matrix plotted along the original fixation line plot. (E) Mapping of the first (green circle) and final (red circle) fixation points for each line.

7.6 Comparisons with patient population

To establish that the visual field manipulations produced the effects that I intended, I compared the control condition (normal reading behaviour) with the simulated hemianopia (left & right side) at the highest blurring level (cut-off frequency, 0.275 cpl). I plotted oculometric measures (*number of forward saccades per line, number of regressive saccades per line, number of saccades made during return sweep*, and *reading speed*) for both, simulated right and left HVFD and for both age groups (Figure 7.9). Measurements from Trauzettel-Klosinski and Brendler (1998a), who recorded similar oculometric measures in patients with pathological HVFD were also included for visual comparison.

Simulated blurring on both left and right hemifields led to significant changes in the oculometric measures compared to the control condition. Overall, *reading speeds* were slower and there was a higher *number of forward* as well as *regressive saccades per line*. In line with this, we found smaller *forward saccade amplitudes* and an increase in the *number of saccades made during the return sweep*. The *median forward saccade amplitude* and *median fixation duration* were calculated for each line and then aggregated for the analysis (see Figure 7.10). To assess statistical significance of these effects, we performed the following analysis. A multiple 3x2 mixed design repeated measures analysis of variance (ANOVA) was used to investigate differences between simulated HVFD location (within subjects factor) and age group (between subjects factor) across our oculometric measures. To correct for multiple comparisons, I adjusted the critical p-value to 0.05/6, using a Bonferroni correction.

For all measures, apart from *median fixation duration*, there was a significant main effect of the HVFD side (smallest $^{*}F(1.42, 38.37) = 11.30$, $p < .001$.). The simulated right HVFD condition led to smaller and more *forward saccades*, more *regressive saccades* along with slower *reading speeds* compared to the simulated left HVFD condition and control. The simulated left HVFD condition resulted in higher number of saccades during the return sweep compared to control, but no statistical difference with the simulated right HVFD condition was found for this measure. Although no significant differences were observed for *median fixation duration* at the aggregated level, we performed a more detailed analysis looking for patterns across lines (see section 7.7.2). Table 7.1 shows average values and results of pairwise comparisons. Note that across all measures with a significant main effect of HVFD, we found significant differences over all combinations of pairwise comparisons (control-right, control-left and right-left) with the exception of the *number of saccades made during return sweep*. For that measure there was no significant difference between simulated right HVFD and left HVFD. Lastly, we did not observe any significant difference between age groups nor any other interaction effects.

---

[*] corrected using *Greenhouse-Geisser sphericity correction*

Table 7.1: Oculometric measures for control, right HVFD and left HVFD. The mean (and standard deviation) were derived after collapsing across age groups. Statistical comparisons were made across all conditions using pairwise t-test (using Bonferroni correction), n.s., *p* >. 05, * *p*<.05, ** *p* <.01 *** *p* < .001

	Control (normal reading)	**Right HVFD**	**Left HVFD**	**Control - Right HVFD**	**Control - Left HVFD**	**Right HVFD - Left HVFD**
Reading speed (words per minute)	309(98.7)	124(50.2)	197(76)	***	***	***
Number of forward saccade per line	3.91(1.77)	7.68(2.39)	5.95(1.79)	***	***	***
Number of regressive saccade per line	0.55(0.59)	3.19(2.88)	1.11(1.17)	***	*	**
Number of saccades made during return sweep	0.28(0.32)	1.18(0.96)	1.27(1.05)	***	***	n.s.
Median forward saccade amplitude (°)	2.23(0.92)	1.32(0.39)	1.70(0.36)	***	**	***
Median fixation duration (ms)	339(217)	330(55.5)	263(33.7)	Main effect n.s.	Main effect n.s.	Main effect n.s.

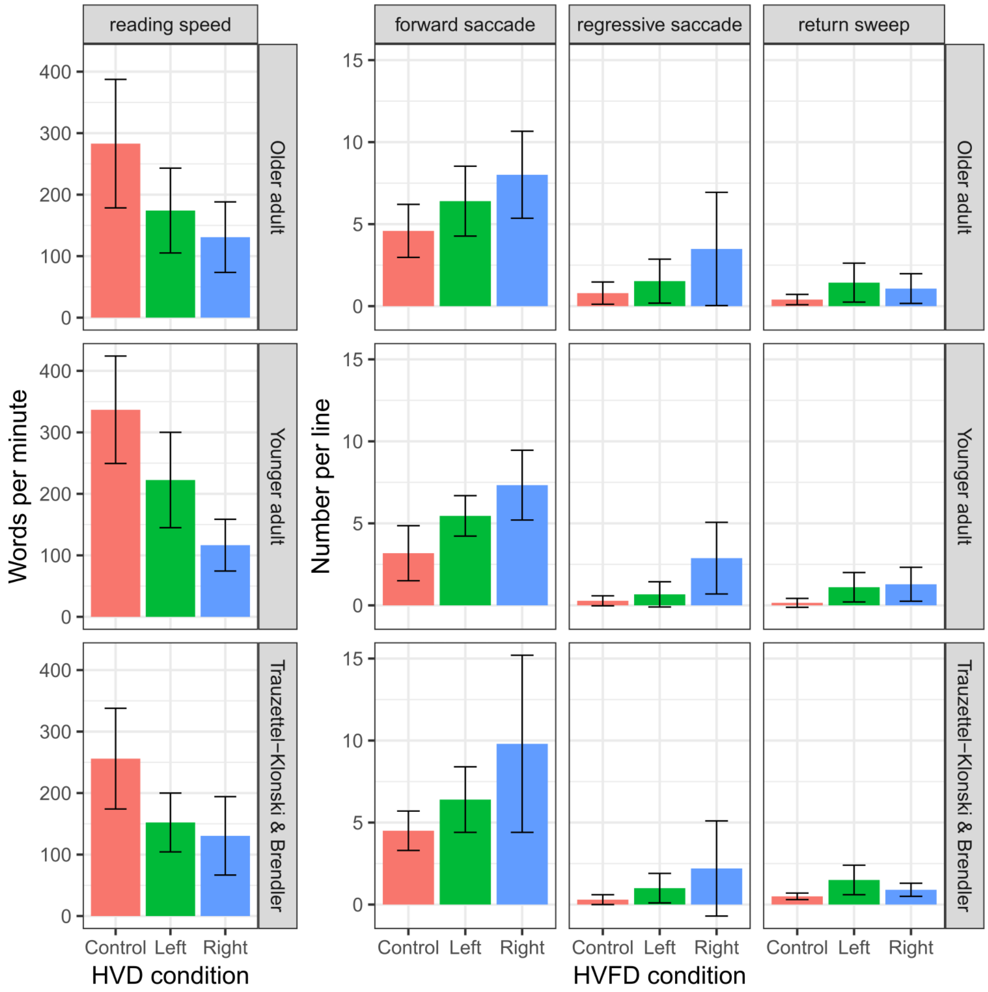

Figure 7.9: Oculometric measures across simulated HVFD sides for both old and young adult groups, along with corresponding measurements from patients with HVFD replotted from Trauzettel-Klosinski and Brendler (1998a) for comparison. To represent both left and right HVFD conditions, the trials of the highest simulated blurring condition (0.25 cpl) across both left and right were used. Number of eye event measures were calculated by the number of occurrences within a single line from the paragraph. (A) *Number of forward saccades per line* (left), *number of regressive saccades per line* (middle) and *number of saccades during return sweep* (right) are measured by the mean number observed across a line, with standard deviation as error bars. (B) Reading speed is measured using mean words per minute. Error bars, ± 1 standard deviation.

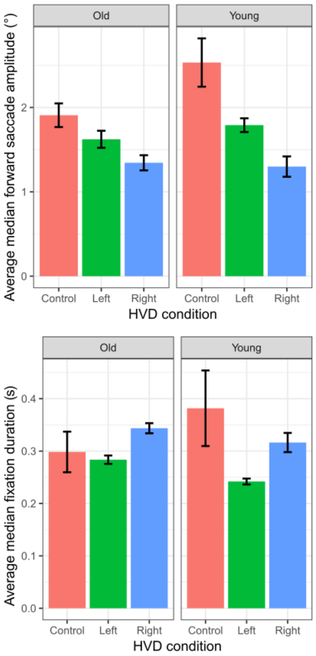

Figure 7.10: *Average median forward saccade amplitude* (above) and *average median fixation duration* (below) across simulated HVFD sides for both old and young adult groups. Error bars, ± 1 standard deviation. The median values for each measure across groups were aggregated into the mean.

7.7 Progressive blurring provides insight on reading with HVFD

7.7.1 The effect of spatial filtering on hemianopic reading

To test the relationship between spatial blurring (cut-off spatial frequency), simulated HVFD side and participant age, I used multiple mixed design repeated measures ANOVAs. The data were *reading speed, number of forward saccade per line, number of regressive saccade per line, number of saccades made during return sweep, average median forward saccade amplitude* and *median fixation duration* and I corrected for multiple comparisons using a Bonferroni corrected p-value of 0.05/6 = 0.0083. All relevant statistical values can be seen in Table 7.2. The main effect of cut-off frequency was observed across all measures except *median fixation duration*, (smallest $^{*}F(2.49, 67.26) =16.23$, $p <. 001.$), indicating that as the level of blurring increased (cut-off frequency decreased), I observed slower reading speed, a higher number of forward and regressive saccades, a higher number of saccades made during the return sweep and shorter average median forward saccade amplitudes. However, we did not find any influence of blurring on *average median fixation duration* (further explored in a later analysis).

The side (left or right) of the simulated vision loss had a significant (main) effect across all measures except for *number of saccades made during* *return sweep* and *median fixation duration* (smallest $F(1, 27) = 13.43$, $p = .001$) indicating that these two measures showed similar performance metrics in both left and right simulated HVFD. The age of participants had no significant effect on any measure, indicating that younger and older participants performed similarly across conditions.

I found an interaction between cut-off frequency and HVFD side for *reading speed, number of forward saccade per line, number of regressive saccade per line,* (smallest $^{*}F(2.39, 64.45) = 9.26$, $p < .001$), but no significant interaction effect for *number of saccades made during return sweep, median fixation duration* and *median saccade amplitude*. To provide a clear, parametric description of the relationship between cut-off frequency and HVFD side, we use a piecewise regression model to estimate the critical cut-off frequency and slope for each of these measures, similar to Kwon and Legge (2012). The descriptive model is captured by the following formula, starting either with a ascending or descending segment followed by a horizontal line:

$$f(x) = \begin{cases} a \cdot x + b - a \cdot c & \text{if } x < c \\ b & \text{if } x \geq c \end{cases}$$

where *f(x)* is the oculometric measure, *x* is the spatial frequency cut-off, *a* represents the slope of the ascending/descending line (depending on the sign of *a*), *b* represents the plateau of the oculometric measure in normal reading behaviour and *c* represents the critical cut-off frequency. I used an iterative, non-linear least-squares method (*optim()* in R version 4.1.0, (R Core Team, 2021)) to estimate the parameters (*a, b, c*) as well as standard errors (which are derived from the diagonal of the Hessian matrix).

Figure 7.11 shows *reading speed, number of forward saccade per line* and *number of regressive saccade per line* plotted against different cut-off frequencies for each simulated HVFD side. The fitted model provided us with two key components that describe the relationship, the *critical cut-off frequency* and *slope of ascent/descent*. The *critical cut-off* frequency represents the estimated minimum frequency required to achieve normal reading behaviour, while the slope indicates the impact on reading performance with each additional filter step (beyond the critical cut-off point). These two measures allow us to quantify the interaction between HVFD side and age group, as cut-off frequency is reduced.

When looking at reading speed, I found that the *right* simulated HVFD had a lower critical cut-off (1.15 cpl ± 0.01) compared to the left simulated HVFD (1.22 cpl ± 0.01). Beyond the critical frequency, reading speed was more affected in the right compared to the left simulated HVFD. A loss of 0.1 cpl in the right visual field resulted in a decrease of 22.0 wpm ± 0.12, compared to a decrease of 11.9 wpm ± 0.11 for left HVFD. Although the loss of visual information had a more severe impact in the *right* simulated HVFD condition, it only occurred at a lower cut-off frequency.

Although a main effect of age was not found using the ANOVA, I performed an analysis of reading speed as a function of cut-off frequency across both HVFD side and age groups, as I was interested in the detailed pattern of reading performance change which was not captured by an ANOVA. Figure 7.12 shows that although the *older* age group shared similar critical cut-off frequencies in both *left* and *right* simulated HVFD (left: 1.23 cpl ± 0.01, right: 1.25 ± 0.01 cpl), the *younger* age group showed that the *left* simulated HVFD had a higher critical cut-off (1.20 cpl ± 0.01) compared to *right* HVFD (1.06 cpl ± 0.01). This suggests that the difference in critical cut-off frequency found in the initial analysis may be largely driven by the *young* adult group.

Similarly, beyond the critical frequency, reading speed was more affected in the right compared to the left simulated HVFD for both age groups. However, the *younger* age group was more impacted by the loss of visual information:a loss of 0.1 cpl in the right side results in a decrease in 29.1 wpm ± 0.02 (left HVFD: 12.5 wpm ± 0.02). In contrast, a loss of 0.1 cpl in the right visual field produces a more modest reduction in reading speed in the older age group (right HVFD: 16.5 wpm ± 0.01, left HVFD: 11.4 wpm ± 0.01).

Among all eye event measures, reading speed remains the most clinically relevant measure for any reading impairment. Although other eye movement measures may provide interesting insights into how they might play into overall reading performance, the experimental design of the current study did not allow us to separate out those effects.

Table 7.2: Statistical summary of mixed design repeated measures ANOVA conducted across oculometric measures (*reading speed*, *number of forward saccades per line*, *number of regressive saccade per line*, *number of saccades made during return sweep*, *average median forward saccade amplitude* and *median fixation duration* respectively). The summary outlines the *main effect of cut-off frequency*, *main effect of HVFD side*, *main effect of age*, and *interaction effect between cut-off frequency and HVFD side*, and their corresponding *F*-statistics , degree of freedoms (df_1 & df_2), and *p*-value. Bonferroni correction was used to correct for multiple comparisons (*p*-value was set to 0.05/6 = 0.008).

Main effect of cut-off frequency

Oculometric Measure	***F***	df_1	df_2	***p***
Reading speed	57.82	1.82	49.15	$< 1e^{-12}$
Forward saccades	52.26	2.38	64.29	$< 1e^{-14}$
Regressive saccades	33.12	1.48	39.84	$< 1e^{-7}$
Return sweep	41.74	2.21	59.72	$< 1e^{-11}$
Forward saccade amplitude	16.23	2.49	67.26	$< 1e^{-16}$
Fixation duration	1.18	1.73	46.78	0.310

Main effect of HVFD side

Oculometric Measure	***F***	df_1	df_2	***p***
Reading speed	22.76	1	27	$< 1e^{-4}$
Forward saccades	25.85	1	27	$< 1e^{-4}$
Regressive saccades	16.33	1	27	$< 1e^{-7}$
Return sweep	0.05	1	27	0.820
Forward saccade amplitude	13.43	1	27	0.001
Fixation duration	2.60	1	27	0.120

Main effect of age

Oculometric Measure	***F***	df_1	df_2	***p***
Reading speed	4.41	1	27	0.045
Forward saccades	4.09	1	27	0.053
Regressive saccades	4.43	1	27	0.045
Return sweep	3.50	1	27	0.072
Forward saccade amplitude	1.47	1	27	0.024
Fixation duration	0.02	1	27	0.900

Interaction effect between cut-off frequency and HVFD side

Oculometric Measure	***F***	df_1	df_2	***p***
Reading speed	10.14	2.69	72.61	$< 1e^{-4}$
Forward saccades	9.26	2.39	64.45	$< 1e^{-3}$
Regressive saccades	10.57	1.43	38.52	$< 1e^{-3}$
Return sweep	0.38	1.46	39.37	0.620
Forward saccade amplitude	3.74	2.28	61.58	0.024
Fixation duration	4.89	2.20	59.31	0.009

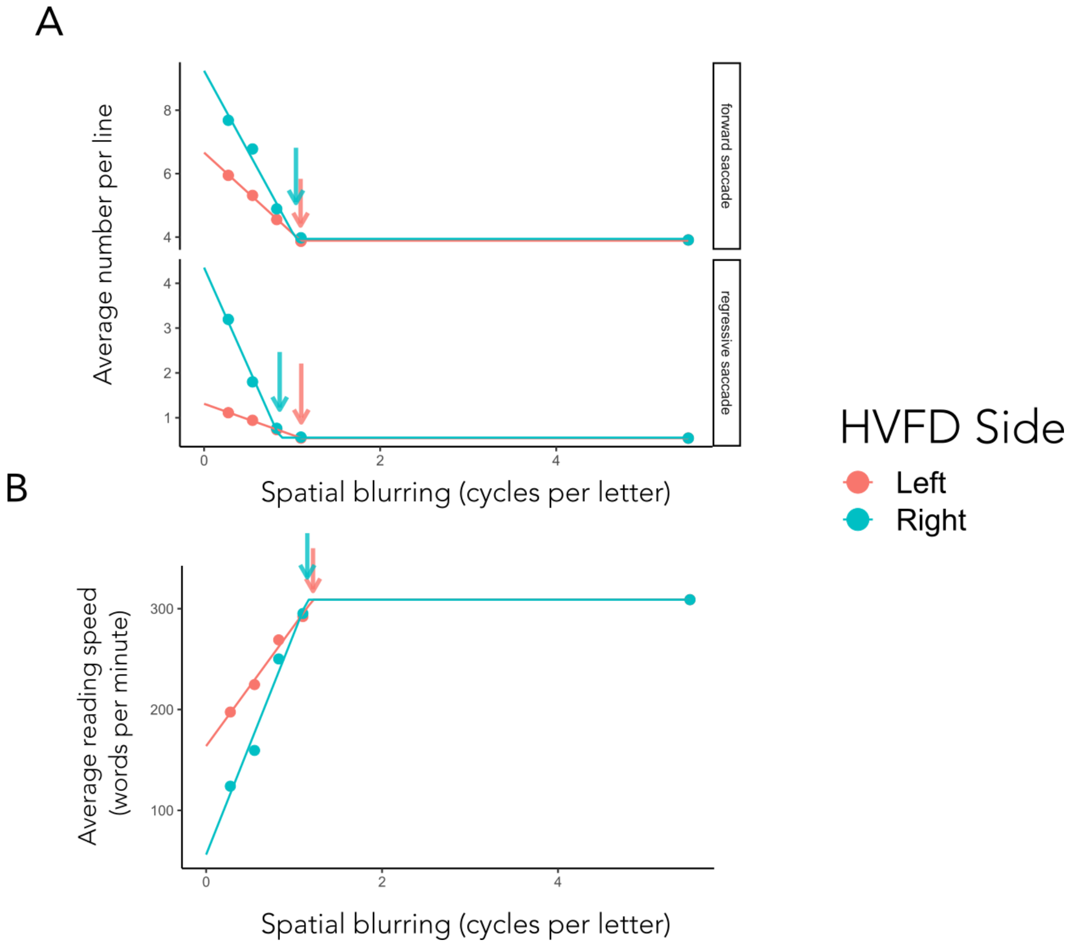

Figure 7.11: Oculometric measures from simulated hemianopic reading at different levels of spatial blurring (pooled across age groups). The lower the cut-off frequency (cycles per letter) of the low-pass spatial filter, the larger the blur. Data is split between HVFD sides (colors). A piecewise linear model was fitted to the group average data (collapsed across age groups), allowing the critical cut-off frequencies and slopes to be calculated. (A) Average number of forward and regressive saccades made per line. (B) Average reading speed - words per minute.

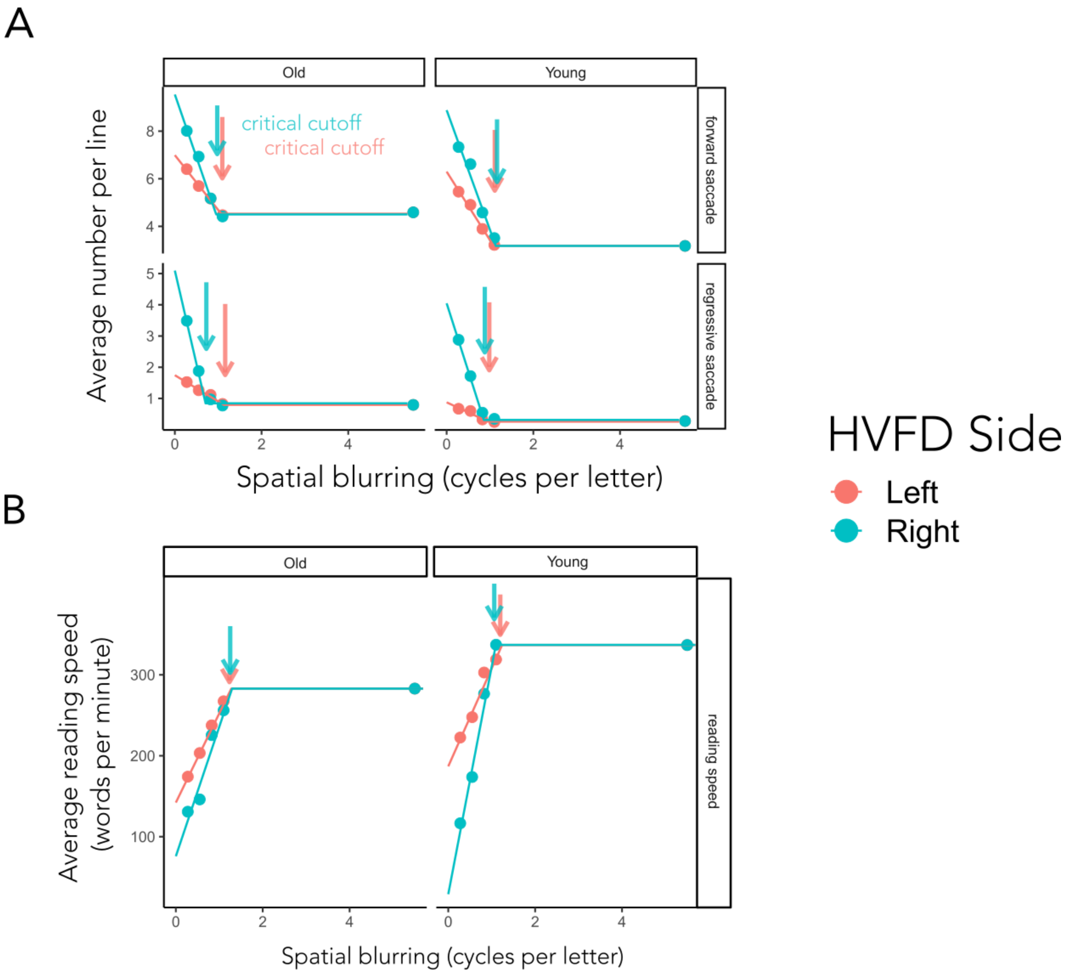

Figure 7.12: Oculometric measures from simulated hemianopic reading at different levels of spatial blurring. The lower the cut-off frequency (cycles per letter) of the low-pass spatial filter, the larger the blur. Data is split up by age groups (left, right facets in plots) and HVFD sides (colors). A piecewise linear model was used to fit the the group average data, allowing the critical cut-off frequencies and slopes to be calculated. (A) Average number of forward and regressive saccades made per line. (B) Average reading speed - words per minute.

7.7.2 Median fixation duration while paragraph reading

In the previous analysis, no statistical differences were found in median fixation duration between HVFD conditions. However, this could have been due to data averaging across different segments (lines of the text), hiding any differences in durations. To clarify this, I performed a separate analysis that looked at median fixation duration across each line, instead of averaging across the paragraph. As there was no significant main effect of age on median fixation duration, I considered the complete data set (collapsed across age groups) for this analysis.

I found that the median fixation duration was longer for simulated loss on the right side than the left. Figure 7.13 shows average median fixation durations across different paragraph sections for both left and right HVFD at different cut-off frequencies. Paragraph sections consisted of 5 lines of text binned into 3 groups: *top, middle* and *bottom*. The 16th line of text was excluded from the analysis, as its length varied in the number of words across the different stimuli. To investigate the relationship between HVFD side, cut-off frequency and paragraph section on fixation duration, I ran a three-way repeated measures ANOVA. I found a significant three-way interaction between simulated HVFD side, cut-off frequency and paragraph bin, $F(56, 1568) = 1.86$, $p < .001$.

To understand the interaction effects across these 3 variables, I ran a simple two-way interaction analysis between simulated HVFD side and paragraph bin for each cut-off frequency level (0.275, 0.55, 0.825 & 1.1 cpl, control condition was excluded). A Bonferroni correction was applied and the level for statistical significance was set to $p < 0.0125$. Firstly, differences in fixation durations were only observed in the 0.275 and 0.55 cpl cut-off frequency, smallest $^{*}F(1.3, 36.45) = 8.40$, $p = 0.003$. The right HVFD had higher median fixation durations compared to the left HVFD side, while the *top* paragraph section shows higher median fixation durations compared to the *middle* and *bottom* section. No statistical differences were found across HVFD side and paragraph bins at higher cut-off frequencies (>0.825 cpl). Secondly, I found a significant interaction effect (between simulated HVFD side and paragraph section) at 0.275 cpl, $^{*}F(1.43, 39.98) = 6.6$, $p = .007$; the *top* (557ms ± 277) paragraph section had significantly longer median fixation duration compared to the *middle* (453ms ± 245) and *bottom* (421ms ± 225) paragraph bin in the right simulated HVFD condition, while in the left simulated HVFD, median fixation duration was similar across the 3 sections (*top*: 265ms ± 101, *middle*: 265ms ± 110, *bottom*: 249ms ± 100). This suggests that as the subjects gained experience reading with the simulated HVFDs, any differences in fixation duration became negligible.

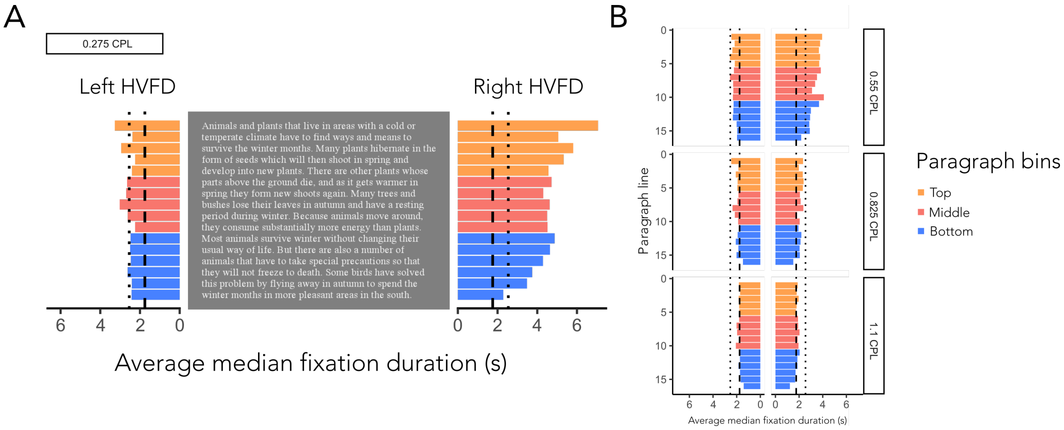

Animals and plants that live in areas with a cold or temperate climate have to find ways and means to survive the winter months. Many plants hibernate in the form of seeds which will then shoot in spring and develop into new plants. There are other plants whose parts above the ground die, and as it gets warmer in spring they form new shoots again. Many trees and bushes lose their leaves in autumn and have a resting period during winter. Because animals move around, they consume substantially more energy than plants. Most animals survive winter without changing their usual way of life. But there are also a number of animals that have to take special precautions so that they will not freeze to death. Some birds have solved this problem by flying away in autumn to spend the winter months in more pleasant areas in the south.

Figure 7.13: Average median fixation duration across paragraph sections for both left and right HVFD at different cut-off frequencies (excluding the control-unfiltered condition). Paragraph sections are binned into 3 groups: *top, middle* and *bottom*; each group consists of 5 lines, the 16th line is excluded in the analysis but shown here in the *bottom* group for visualisation purposes. (A) (0.275 cpl) Measurements from the left and right HVFD conditions are displayed respectively to the left and right of the text stimuli. The dashed line represents the overall average median fixation duration in the control condition (unfiltered - 5.5 cpl) while the dotted line is 1 sd above the mean. (B) (0.55, 0.825, 1.1 cpl) Measurements are displayed in the same format without the text stimuli in between the two HVFD conditions.

7.8 Discussion

The current design found similar eye movement patterns with simulated HVFD in healthy participants as those in patients with HVFD. In the first set of results, which compared the highest blurring level to simulate HVFD in each hemifield against the control (unfiltered) condition, showed directly comparable results to studies in patients with HVFD (Trauzettel-Klosinski & Brendler, 1998a; Zihl, 1995). This is an important first step in establishing that the stimulus manipulation that was introduced mimics task-critical properties of HVFD. In the simulated left HVFD, both the younger and older group required more saccades to find the start of the new line during the return sweep, similar to patient data.

Surprisingly, an increase in the number of return sweep saccades was also observed in simulated right HVFD. Although this feature of impairment is more typically associated with left HVFD, the findings are consistent with hemianopia patient data (Trauzettel-Klosinski & Brendler, 1998a), where the increase in number of saccades during the return sweep was similar across both left and right HVFD (see Figure 7.9, right column). In the simulated right HVFD conditions, I found higher numbers of smaller forward saccades and regressive saccades along with more fixations of longer duration in both younger and older adult populations, matching the eye movements patterns in the patient population. (Note that the number of forward and regressive saccades are a proxy measure of number of fixations, as a saccade precedes a fixation.)

The reduction in reading speed, across both simulated HVFD conditions, mirrors that found in patients (Trauzettel-Klosinski & Brendler, 1998a; Zihl, 1995). Right HVFD severely impairs reading speed (slowing reading speed to around half the rate of the control condition) with left HVFD having a lesser impact.

Having established that the HVFD manipulation produces qualitatively similar effects on eye movement patterns for paragraph reading, I examined how the degree of spatial filtering influenced reading speed. I estimated the critical filter cut-off frequency - the point where blurring a particular hemifield starts impacting reading speed. Importantly, the *slope* of the function quantifies the decline in reading performance with each filter step. The findings suggest that the spatial requirements to maintain fluent reading is lower in the right HVFD side compared to the left HVFD side, as reflected in the lower critical cut-off frequency (right HVFD: 1.15 cpl, left HVFD 1.22 cpl).

Beyond the critical cut-off, I observed a steeper decline in reading speed under the simulated right HVFD compared to simulated left HVFD, which is also consistent with patient data (Trauzettel-Klosinski & Brendler, 1998a; Zihl, 1995). It seems that there is a resilience to the loss of spatial information in the right hemifield despite the steeper decline in reading speed past the critical cut-off, but why is this the case? In my analysis, it appears that this difference was largely driven by the younger adults, although I did not find any significant age-related differences in the ANOVA. The piecewise regression model provides a more detailed description of the age-related differences across different levels and a transition point - the *critical cut-off frequency*. In my experiments, the critical cut-off frequency for reading speed is approximately 1.20-1.25 cpl (across age groups and HVFD location). For the right simulated HVFD condition, the younger adult group showed a slightly lower critical cut-off of 1.06 cpl. Beyond the critical cut-off, young adults appear to be impacted more by systematic loss of spatial information in the right hemifield. Both age groups show a steeper decline in reading speed under the simulated right HVFD (compared to simulated left HVFD), but this difference is much more prominent in younger adults (29.5 wpm per 0.2 cpl in young adults against 16.5 wpm per 0.2 cpl in older adults). This suggests that younger adults are less sensitive to the loss of spatial information in the right hemifield compared to older adults.

One explanation for the lower critical cut-off in younger adults could be the decline in sensitivity to medium and high spatial frequencies as a function of increasing age (Ross et al., 1985). The difference between younger and older adults suggests that some higher spatial frequency content in the parafoveal region provides information to maintain reading fluency in younger adults. Previous studies have also shown that older adults are less efficient at using parafoveal information when reading (Rayner et al., 2009; Risse & Kliegl, 2011), and has been attributed to age-related decline in modulating fixation durations in response to processing opportunities in the perceptual span. I speculate that a combination of higher sensitivity to a larger range of spatial frequencies *and* more efficient parafoveal processing, is contributing to the lower critical cut-off frequency in younger adults.

Paterson et al. (2013) has shown that younger adults display better comprehension and faster reading speeds, compared to older adults, in conditions where text outside a moving-window contains only medium and high spatial frequencies. In their study they used a gaze-contingent moving-window paradigm, where text outside the moving window was spatially filtered to leave low, medium and high bands of spatial frequencies (2.6 - 5.2, 5.0 - 10.0, and 8.3 - 16.6 cycles per degree (cpd) respectively, with 4 letters subtending 1.2° so one letter subtending 0.3°). They also found that reading performance in older adults were less affected when the filtered text contained only low (2.6 - 5.2 cpd) or medium spatial frequencies, compared to younger adults. Their findings suggested that younger adults were more attuned to fine scale information when reading (medium-high spatial frequencies) whereas older adults relied on coarser, contextual based information (low-medium spatial frequencies). Although letter sizes across this study and theirs showed a modest difference (0.09°), the critical cut-off frequency of 1.06 cpl in the young adults data approximately translates to 4.88 cpd, which is similar to their medium spatial frequency range (5.0-10.0 cpd). This is analogous to the current finding: younger adults showed a sharper decline in reading speed past the critical cut-off in right HVFD, compared to older adults. It should be noted that Paterson et al., used a series of sentences, rather than entire paragraphs. My work suggests that the attenuation difference across spatial frequency between young and old readers extends to more complex reading tasks, where crowding effects and fatigue are more commonly experienced.

The steeper decline in younger adults beyond the critical cut-off could also be related to the starting performance level of reading: the average reading speed was 337 wpm in young adults compared to 283 wpm in older adults. With maximal blurring, reading speed drops to a similar floor in both age groups. At that point, reading speed is likely determined by a common factor across all subjects. However, because the reading speed in the unblurred condition is much higher in younger subjects, the performance loss appears to be more precipitous in the younger group.

It is important to note that the filter manipulation is *simulating* a visual field deficit in participants with normal vision. This approach cannot entirely mimic the actual impairments that arise from HVFD, which may not be limited to a loss of spatial vision. As pointed out by Schuett et al. (2008b), while the visual field deficit plays a key role in hemianopic dyslexia, it is not the only cause. In a few cases where occipital white matter, occipitoparietal structures, or the posterior thalamus is spared, individuals are capable of developing efficient and spontaneous oculomotor adaptation to compensate for the deficit (Corbetta & Shulman, 2002; Schuett et al., 2008b; Zihl, 1995; Zihl, 2010). Some oculomotor adaptations involve switching to ‘safe-but-slow’ saccadic eye movements (Meienberg et al., 1981) while more efficient adaptations involve top-down guided predictive saccade overshoot into the blind field (Zangemeister et al., 1995). These forms of compensation do not occur in the majority of cases and reading impairment persists in many with HVFD (Horton et al., 2021; Zihl, 2010). That said, it is clear that the changes in eye movement patterns we observe are more likely to reflect early stages of visual loss and not compensatory eye movement strategies that subsequently develop over time. It is possible that through chronic exposure to hemianopic blur, new oculomotor reading behaviour could develop, but this would require a longitudinal design where participants are repeatedly trained to read in the presence of blur. Interestingly, adapted oculomotor behaviour is probably the only route to improved performance, since there is effectively no perceptual learning for targets subjected to image blur (Westheimer, 2014).

The methods presented here for measuring the critical cut-off for reading speed have some potentially interesting implications for restitutive strategies in the blind field of stroke survivors (Barbot et al., 2021; Huxlin et al., 2009). Studies that have attempted to restore visual function in the blind field via training, have demonstrated robust sensitivity improvements for specific types of visual information (e.g. luminance and motion detection, coarse orientation discrimination) when spared cortical regions still respond to visual stimuli in the blind field (Barbot et al., 2021; Beh et al., 2022; Papanikolaou et al., 2014). An important next step would be to ask whether recovery of function inside the blind field has a beneficial, knock-on effect, on text reading. The data show that beyond the cut-off frequency, small improvements in the representation of stimuli can have a dramatic impact on the pattern of eye movements and reading performance. At present there is insufficient data to guide recovery of reading performance in HVFD.

What level of visual recovery would be required in order to observe any improvement in reading performance? How much improvement is required to regain fluent reading capabilities? This study seeks to act as a starting point to explore the effects of partial visual restoration on reading with hemianopia and other forms of vision loss. By systematically degrading visual information, the point where eye movement patterns change and reading performance is reduced can be measured in healthy volunteers. Training efforts could then be tested in scenarios where vision is artificially degraded. For example, in right HVFD with macular sparing (due to preserved perfusion from the middle cerebral artery), reading performance is often normal (Horton et al., 2021; Leff et al., 2000; Trauzettel-Klosinski & Reinhard, 1998). This suggests a set of experiments with testable predictions: any enhancement of the reading span in the right hemifield in patients with reduced macular sparing is likely to be highly beneficial. The findings also suggest a difference in resilience to the loss of spatial information in the right hemifield across younger and older adults. Hence it is important to test these paradigms on age brackets that have shown high stroke incidence rates, so they can be translated into patient groups. The general approach in this study could also be extended to different configurations of visual manipulations. Other aspects of the stimuli that are pivotal to reading, such as contrast sensitivity, spatial context or the shape of the visible aperture could be used to mimic different types of visual field defect, such as quadrantanopia or other patterns of visual field loss seen in glaucoma or macular disease.

Chapter 8

General conclusions

8.1 Overview

This chapter provides a summary of the entire thesis and discusses the main findings and potential future work that could be developed.

8.2 Summary of findings

In Chapter 1 of the thesis, it was established that HVFD is a debilitating visual impairment caused by postgeniculate damage, affecting many facets of daily living, most notably reading ability (Trauzettel-Klosinski & Brendler, 1998a; Zihl, 1995). In terms of rehabilitative options for HVFD, it appears that previous restitutive approaches showed potential in recovering visual function in the 'blind' field and this has, understandably, generated much excitement. Although large clinical trials were unable to replicate the same levels of success (Cavanaugh et al., 2020), it may be because the potential for visual recovery is largely driven by surviving anatomical and functional circuits that can support visual function in the 'blind' field (Barbot et al., 2021; Papanikolaou et al., 2014), which can vary a lot between individuals. To investigate this idea, I proposed a line of research that used a cross-modal imaging approach to acquire higher-resolution definitions of the patient-specific patterns of visual field coverage and cortical integrity, which will ultimately improve both diagnosis and our understanding of the disorder (Millington et al., 2017). Additionally, I also conducted an investigation into simulating hemianopia whilst reading, using a gaze-contingent paradigm, in healthy controls. The aim here was to develop a laboratory test bed to help identify the most promising strategies for mitigating HVFD, before translation to patient groups.

In the cross-modal imaging study (see Chapter 2 - 6), I initially planned to recruit a group of 10-12 stroke survivors with HVFD. However, due to the experimental testing restrictions caused by the COVID-19 outbreak, recruitment of stroke survivors was discontinued due to health and safety concerns. Many stroke survivors opted to shield during the pandemic due to pre-existing vascular risk factors and the number of new patients attending hospital with acute stroke-related symptoms also declined dramatically (Uchino et al., 2020). Despite these challenges, I was able to recruit 4 stroke survivors with HVFD (who were also eligible for brain scans) prior to the onset of the pandemic. In Chapter 2, I outlined relevant clinical and demographic information for each stroke survivor. The visual assessments conducted were outlined in detail. This included *refraction*, visual *acuity measurement*, *ocular alignment* and *motility static*, *kinetic* and *microperimetry*. These assessments revealed that two participants had homonymous hemianopia (no macular sparing) and two had homonymous quadrantanopia (one with macular sparing - participant 14326). In addition, all participants showed no presence of spatial neglect and were able to maintain stable fixation (which is important for measuring accurate and reliable visual function in the brain).

Chapter 3 outlined the scanning pipeline for the cross-modal imaging study, which included the acquisition of *T1-weighted, T2-weighted anatomical images, T2*-weighted (BOLD) images*, a *B0 map* and *diffusion weighted images*. The key feature of our protocol was that we were able to acquire useful imaging data in a relatively short time frame without sacrificing data quality and patient comfort. This balance is important as it is not realistic to scan stroke survivors for long periods due to their age and comfort. This chapter also provided information about the standard retinopathy stimulus used in the scanner, the scanning parameters used for each imaging protocol along with the preprocessing steps.

Chapter 4 provides a description of how I mapped and visualised functional visual responses in the brain using standard retinotopy stimuli (DeYoe et al., 1996), population receptive field analysis and visual field coverage maps (Papanikolaou et al., 2014). Using the L. Wang et al. (2015) probabilistic atlas (described in Chapter 5), I was able to quantify and compare visual field responses across the lesioned hemisphere and non-lesioned hemisphere for all stroke survivors, in a reproducible and standardised measure (cf Table 4.1). This revealed the different extents of residual visual function in the blind field across participants, most notably in participant 11773 (complete left homonymous hemianopia). Visual field coverage maps across 3 regions with high pRF counts (V3, LO1 and IPS0) showed consistent residual function in the lower quadrant of the hemifield within the scotoma (see Figure 4.14), providing support for common residual input from these areas from this region of the blind field.

In Chapter 5, I discussed how the analysis of anatomical and diffusion weighted images was conducted. Due to abnormal structures in lesioned brains, I developed a pipeline that uses a semi-automatic lesion segmentation tool, ITK-SNAP (Yushkevich et al., 2016) and optiBET (a tool that wraps FSL's BET and optimized for lesioned brains) to produce reliable brain and lesion masks. I have shown that using these masks improves the registration and normalization process. Here I also described how I used the Wang et al., atlas to identify 25 cortical ROIs in visually responsive areas (subdivided into 5 cortical territories for visualization purposes). I highlighted in the chapter that lesion size was not a good indicator of visual field loss. One participant (11773) manifested a complete homonymous hemianopia despite a relatively small lesion, contrasting with another participant (13978) with quadrantanopia with a relatively large lesion definition.

This chapter also described the distortion correction, tensor model and probabilistic tractography pipeline for analyzing diffusion weighted data. I identified 3 major tracts that connected cortical fields within and between occipital lobes and compared fractional anisotropy (FA) values across lesioned and non-lesioned hemispheres for all stroke survivors. Although there was a clear reduction in mean FA values – an indirect measure of white matter integrity - in the lesioned hemisphere for all participants, the magnitude and pattern of reduction was markedly different across participants.

Chapter 6 discussed the insights gained from the different imaging data of stroke survivors with homonymous visual field deficits. It is clear that there are distinct 'mismatches' between the clinical, static perimetry and imaging- defined measures of visual field coverage. It is only by considering the complementary information from each measure, that we can build a better understanding of stroke damage and any residual visual capacity. Our multi-modal approach allowed us to obtain two crucial bits of information which I think are vital to restitutive strategies:(1) the location of any sparing in the impaired visual field and (2) what functional/anatomical regions are partially or fully intact. Together, this can potentially guide the *where* (location of stimulus) and *what* (choice of stimulus or task) in perceptual learning based training (Barbot et al., 2021; Huxlin et al., 2009). Combining this information effectively may lead to the highest likelihood of rehabilitation success.

Chapter 7 explored how we might use the degradation of spatial information in the hemianopic field to understand the impact of visual recovery on reading performance, using a gaze contingent paradigm simulating hemianopia. This paradigm allowed us to determine the cut-off frequency where the pattern of eye movements change and reading performance is reduced. These measures allow us to make inferences about the extent of visual function recovery required via restitutive HVFD strategies to restore functional reading performance. While the spatial content of text is a vital component of reading fluency, it is also possible to explore different manipulations of visual input, such as contrast sensitivity, spatial context or the shape of the visible aperture, in order to mimic a broader range of typical visual field defects. This experiment acts as a starting point for exploring the effects of partial visual restoration on reading with hemianopia and allows us to test new ideas in healthy controls, before translating to patient groups.

8.3 Future directions

8.3.1 Using imaging to guide perceptual learning based training programs

Perceptual learning based training programs commonly involve presenting moving high contrast stimuli in the ‘blind’ field, with stimulus intensity controlled via a psychophysical procedure, whilst the subject performs a task. Previous work typically targeted training to locations along the border of the scotoma using various kinds of stimuli (Barbot et al., 2020; Casco et al., 2018; Huxlin et al., 2009; Pleger et al., 2003; Sahraie et al., 2006). With the methodology developed here to identify key functional pathways and anatomical regions that are spared and still respond to visual stimulation, we can start to define candidate stimuli for use in learning-based training programs. These can be specified to target functioning regions; using information specific to each patient to determine *where* and *what* kind of stimuli. My hypothesis is that training specific visual field locations (*where*) in the blind field – that still responds to visual stimulation, using targets and tasks that have been shown to be actively processed at sites (*what*) that are spared, will lead to the highest likelihood of visual recovery. The challenge here is to be able to disentangle the improvements that arise from these two components.

Figure 8.1 shows an example of how an experiment may look. Figure 8.1a shows an example of residual visual function identified using a brain-based visual field coverage map (for more details see Chapter 4). Based on this example, we can select two regions to target for training, a visual field location where the functional mapping has identified residual visual function (red), and a secondary location, at a common eccentricity, but with no identified residual visual function (blue). We would expect to see results similar to Figure 8.1b post-training, showing that training in locations with residual visual function result in statistically significant improvements in the task, as opposed to training in locations without residual visual function (blue) showing no significant improvements. Next we can then compare across visual areas defined by a probabilistic atlas (similar to methods found in Chapter 5) for each participant as seen in Figure 8.1c. In the scatter plot, each dot represents a single participant, showing the pRF count for a particular visual area and the results post-training. By plotting this relationship for each participant, we could interpret what is driving the improvement in visual function in the training location. If there are high pRF counts in a visual area (see visual area A) along with large improvements in the task, we can infer that recovery is likely driven by this visual area. If there are low pRF counts and we observe large improvements in the tasks among participants (see visual area B), it is unlikely that this visual area is driving the recovery. And is it also possible that we observe two visual areas with high pRF count complimented with large improvements post-training (see visual area C), suggesting that a possible combination of two visual areas are involved.

There are, however, some additional considerations for design like the one outlined above. If the visual deficit is partial (such as in quadrantanopia), it may be difficult to identify (if any) and train a location with and without residual visual function as the loss would be confined to a relatively constricted region of the visual field. Additionally, as the possible anatomical/functional sparing is not clear prior to scanning of the participants, the pattern of spared cortices or functional networks might not allow us to make the comparisons mentioned above (for example, if residual function is confined to only one or two visual areas across all participants).

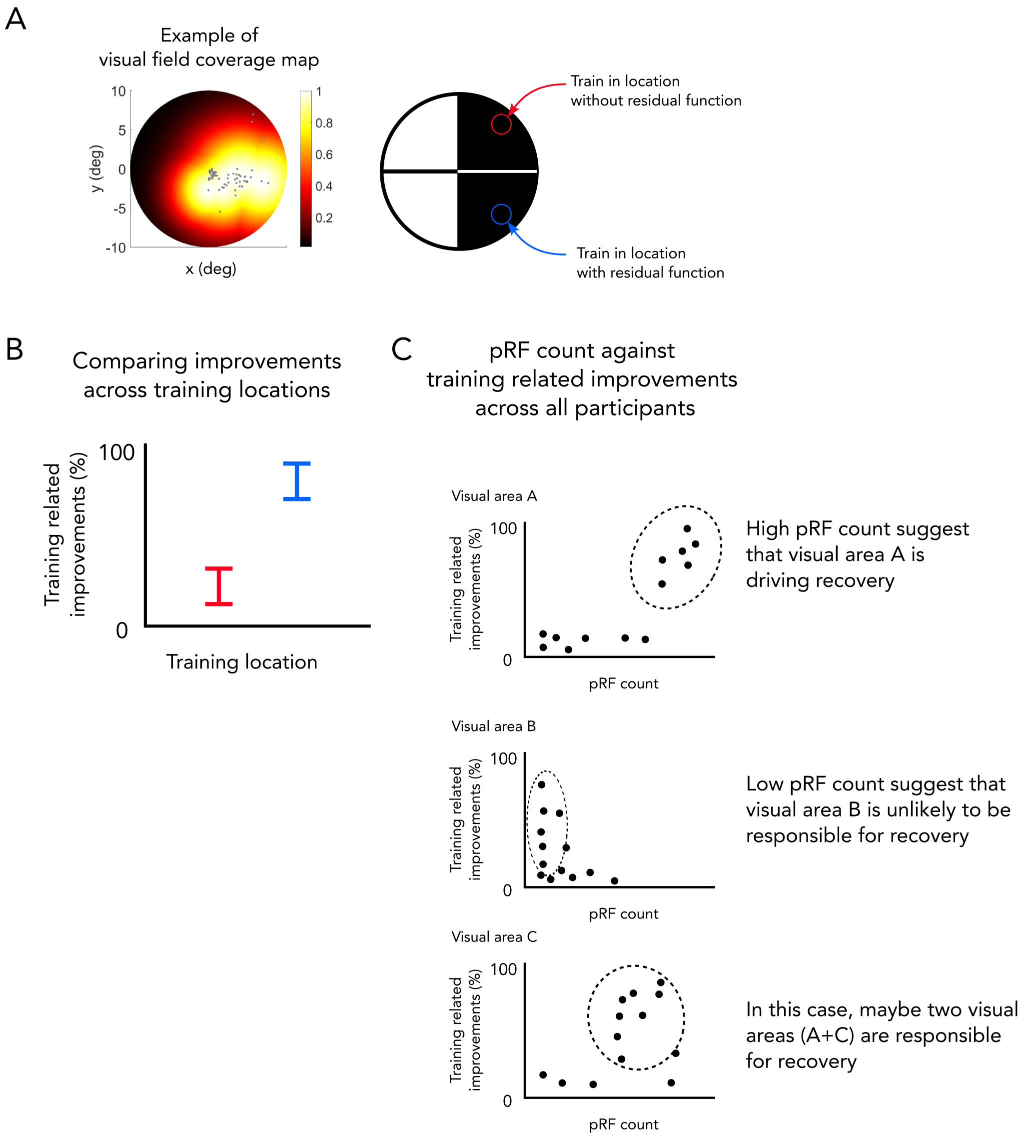

Figure 8.1: Diagram of possible developments to investigate the relationship between restitutive training related improvements and spared functional/anatomical circuits. (A) Example of residual visual function identified using a visual field coverage maps (for more details see Chapter 4). Based on this example, we can select two regions to target for training, a visual field location where the functional mapping has identified residual visual function (red), and a secondary location with similar eccentricities but with no identified residual visual function (blue). (B) Example of post-training results, showing that training in locations with residual visual function (red) result in statistically significant improvements in the task, as opposed to training in locations without residual visual function (blue) showing no significant improvements. (C) Example of a series of plots depicting different visual field areas, visualizing the relationship between training-related improvements and pRF count respective to the visual area.

8.3.2 Improve upon current analysis of the visual deficit and imaging data

The current approach allows us to characterize the extent of visual field deficit, lesion size and location, any functional responses and also white matter integrity. Together, this provides a multivariate picture of the stroke damage. As analysis methods improve and even more precise measurements can be obtained, a clearer picture of the stroke damage can emerge that will better inform potential rehabilitative strategies to exploit. I identified three key facets that could lead to potential improvements of our technique: (i) using kinetic perimetry, alongside static perimetry, to assess visual field deficits; (ii) Using novel stimulus configurations (as opposed to the standard retinotopic stimulus) to potentially evoke stronger functional responses in higher visual areas (such as the fusiform face area, known to be sensitive to face stimuli (Kanwisher et al., 1997)); (iii) Using T2-weighted images in conjunction with T1-weighted images to improve the current pipeline for establishing a lesion mask, potentially also in a robust, automated way.

(i) As mentioned in Chapter 2, I opted out of using a kinetic perimeter as part of the visual fields assessment because I only had access to manual kinetic perimetry, which lead to methodological issues tied to operator's experience in using the instrument. For the purposes of the current study, the static perimetry and microperimetry measures already provided a comprehensive measurement of the visual field deficit within the central 10°, but this may not be the case in future work. Besides reading impairments, HVFD also makes it difficult to navigate crowded environments (Goodwin, 2014; Szlyk et al., 2005). If I wish to explore this component of the impairment, assessing visual deficit using kinetic perimetry could be more appropriate as it is able to cover a larger part of the visual fields. To overcome the methodological issues tied to manual kinetic perimetry, I could explore access to an automated kinetic perimetry (Mönter et al., 2017), which are more standardized with high test-retest reliability. The key advantage with kinetic perimetry is that it could chart the sensitivity profile of a scotoma. Tightly space contours would indicate that targets of all different sizes are seen at around the same point and the edge of the scotoma is highly demarcated. However, more gradual spacing of the contours may be indicative of tissue around the edge that is damaged, rather than lost, and this may be helpful in terms of predicting recovery or where to train. It would be very difficult to get this information from static perimetry or microperimetry.

(ii) As alluded to in Chapter 6, a potential future project could investigate the use of stimuli that more selectively activate particular, higher visual areas. The current pRF paradigm involves the use of standard retinotopy stimulus – different configurations of apertures that reveal a high luminance contrast reversing pattern (DeYoe et al., 1996; Dumoulin & Wandell, 2008), aimed at evoking a response to a wider range of neuronal populations. However, the use of more selective stimuli have been shown to better characterize pRF parameters in higher visual areas (Yildirim et al., 2018). Improving on our current approach, we could possibly include additional stimuli during the scanning session without compromising the current measures. The challenge here is to identify key stimulus configurations that would give us meaningful information that compliments our current analysis. Some possible stimulus configuration ideas that would be interesting to investigate include: contrast modulated noise stimuli, isoluminant coloured stimuli, and stimulus apertures that are defined by different in orientations or local motion.

(iii) In the current pipeline, I acquired T2-weighted images which were not required in the final analysis. As mentioned in Chapter 5, ITK-SNAP has a function that converges across different image layers to isolate the lesion. This may results in more precise lesion definition, especially in cases where the boundary of the lesion appears ambiguous in T1-weighted images (both CSF and inflammation appear dark). In addition, automated image segmentation algorithms, such as those implemented in FSL/FAST (Jenkinson et al., 2012), can make use of multiple contrasts to improve tissue labelling. The inclusion of multiple contrasts into my analysis pipeline would reduce errors at each processing step, and ultimately improve the characterization of the lesion.

8.3.3 Test different configurations of visual manipulations in the gaze contingent paradigm

In Chapter 7, I used a systematic approach to degrade visual information in a simulated hemianopic field to study the potential for visual restoration and its impact of reading performance. A potential future investigation could take a different approach. Instead of reducing the level of blurring across the entire hemifield, particular locations where the blurring is reduced could be introduced, leaving the rest of the screen blurred, as seen in Figure 8.2. The example shows an area approximating the central 2° where I would reduce the level of blurring. This might more closely resemble visual restoration, as previous studies have shown some level of visual function recovery near the border of the scotoma (Barbot et al., 2020; Huxlin et al., 2009), as opposed to the design in Chapter 7 where blurring is reduced across the entire hemifield. The manipulation of this particular location (central 2°) could also be a good starting point to investigate gradual visual function recovery in terms of reading impairments, as stroke survivors with macular sparing were found to be able to maintain reading fluency (Horton et al., 2021).

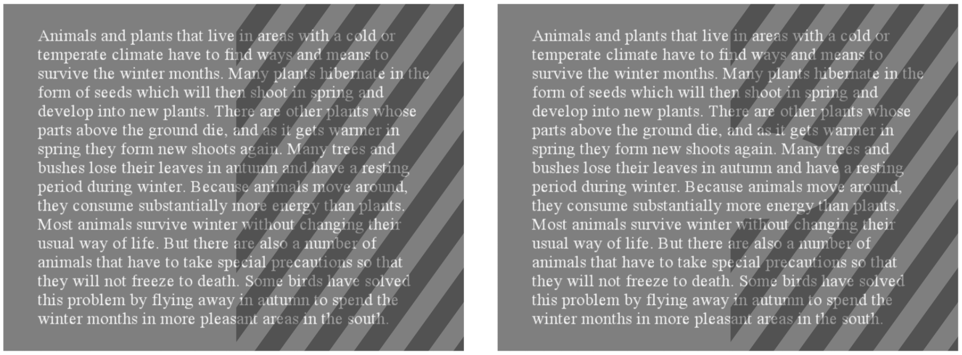

Animals and plants that live in areas with a cold or temperate climate have to find ways and means to survive the winter months. Many plants hibernate in the form of seeds which will then shoot in spring and develop into new plants. There are other plants whose parts above the ground die, and as it gets warmer in spring they form new shoots again. Many trees and bushes lose their leaves in autumn and have a resting period during winter. Because animals move around, they consume substantially more energy than plants. Most animals survive winter without changing their usual way of life. But there are also a number of animals that have to take special precautions so that they will not freeze to death. Some birds have solved this problem by flying away in autumn to spend the winter months in more pleasant areas in the south.

Animals and plants that live in areas with a cold or temperate climate have to find ways and means to survive the winter months. Many plants hibernate in the form of seeds which will then shoot in spring and develop into new plants. There are other plants whose parts above the ground die, and as it gets warmer in spring they form new shoots again. Many trees and bushes lose their leaves in autumn and have a resting period during winter. Because animals move around, they consume substantially more energy than plants. Most animals survive winter without changing their usual way of life. But there are also a number of animals that have to take special precautions so that they will not freeze to death. Some birds have solved this problem by flying away in autumn to spend the winter months in more pleasant areas in the south.

Figure 8.2: Example of a new design to study visual restoration and reading performance. (Left) Example of current filter applied on one side of the screen (respective to eye positioned in the center) to simulate hemianopia. (Right) New design would only systematically reduce the blurring in a particular location (in this example it would extend from the eye position towards the simulated hemianopic field), and leave the rest of the screen at maximum blurring levels.

8.4 Concluding remarks

The work presented in this thesis provides useful tools that allows us to characterise stroke damage and visual field loss more clearly and using different ways of quantification, ultimately building a more accurate profile of the homonymous visual field deficit. Besides deepening our understanding of the relationship between the visual impairment and anatomical or functional damage in the brain, this approach may also better inform rehabilitation strategies with the highest likelihood of recovery.

Bibliography

Acton, S. T. (2009). Chapter 20 - Diffusion Partial Differential Equations for Edge Detection. In A. Bovik (Ed.), *The Essential Guide to Image Processing* (pp. 525–552). Academic Press. https://doi.org/10.1016/B978-0-12-374457-9.00020-2

Ajina, S., Pestilli, F., Rokem, A., Kennard, C., & Bridge, H. (2015). Human blindsight is mediated by an intact geniculo-extrastriate pathway. *eLife*, *4*, e08935. https://doi.org/10.7554/eLife.08935

Altman, J., & Das, G. D. (1965). Autoradiographic and histological evidence of postnatal hippocampal neurogenesis in rats [Publisher: Wiley Online Library]. *Journal of Comparative Neurology*, *124*(3), 319–335.

Andersson, J. L. R., Skare, S., & Ashburner, J. (2003). How to correct susceptibility distortions in spin-echo echo-planar images: Application to diffusion tensor imaging. *NeuroImage*, *20*(2), 870–888. https://doi.org/10.1016/S1053-8119(03)00336-7

Aqil, M., Knapen, T., & Dumoulin, S. (2020). Biologically inspired unification of population receptive field models provides new insights into cortical computations. *Journal of Vision*, *20*(11), 377. https://doi.org/10.1167/jov.20.11.377

Astle, A. T., Blighe, A. J., Webb, B. S., & McGraw, P. V. (2015). The effect of normal aging and age-related macular degeneration on perceptual learning [Publisher: The Association for Research in Vision and Ophthalmology]. *Journal of Vision*, *15*(10), 16–16. https://doi.org/10.1167/15.10.16

Astle, A. T., Webb, B. S., & McGraw, P. V. (2011). Can perceptual learning be used to treat amblyopia beyond the critical period of visual development? [_eprint: https://onlinelibrary.wiley.com/doi/pdf/10.1111/j.1475-1313.2011.00873.x]. *Ophthalmic and Physiological Optics*, *31*(6), 564–573. https://doi.org/https://doi.org/10.1111/j.1475-1313.2011.00873.x

Barbot, A., Das, A., Melnick, M. D., Cavanaugh, M. R., Merriam, E. P., Heeger, D. J., & Huxlin, K. R. (2020). Changes in perilesional V1 underlie training-induced recovery in cortically-blind patients [Publisher: Cold Spring Harbor Laboratory]. *bioRxiv*.

Barbot, A., Das, A., Melnick, M. D., Cavanaugh, M. R., Merriam, E. P., Heeger, D. J., & Huxlin, K. R. (2021). Spared perilesional V1 activity underlies training-induced recovery of luminance detection sensitivity in cortically-blind patients [Number: 1 Publisher: Nature Publishing Group]. *Nature Communications*, *12*(1), 6102. https://doi.org/10.1038/s41467-021-26345-1

Barbur, J. L., Watson, J. D., Frackowiak, R. S., & Zeki, S. (1993). Conscious visual perception without VI [Publisher: Oxford University Press]. *Brain*, *116*(6), 1293–1302.

Barker, W. H., & Mullooly, J. P. (1997). Stroke in a Defined Elderly Population, 1967-1985 [Publisher: American Heart Association]. *Stroke*, *28*(2), 284–290. https://doi.org/10.1161/01.STR.28.2.284

Basser, P. J., Pajevic, S., Pierpaoli, C., Duda, J., & Aldroubi, A. (2000). In vivo fiber tractography using DT-MRI data [_eprint: https://onlinelibrary.wiley.com/doi/pdf/10.1002/1522-2594%28200010%2944%3A4%3 *Magnetic Resonance in Medicine*, *44*(4), 625–632. https://doi.org/10.1002/1522-2594(200010)44:4<625::AID-MRM17>3.0.CO;2-O

Beh, A., McGraw, P. V., Webb, B. S., & Schluppeck, D. (2022). Linking Multi-Modal MRI to Clinical Measures of Visual Field Loss After Stroke. *Frontiers in Neuroscience*, *15*. Retrieved January 17, 2022, from https://www.frontiersin.org/article/10.3389/fnins.2021.737215

Behrens, T. E. J., Berg, H. J., Jbabdi, S., Rushworth, M. F. S., & Woolrich, M. W. (2007). Probabilistic diffusion tractography with multiple fibre orientations: What can we gain? *NeuroImage*, *34*(1), 144–155. https://doi.org/10.1016/j.neuroimage.2006.09.018

Behrens, T. E. J., Woolrich, M. W., Jenkinson, M., Johansen-Berg, H., Nunes, R. G., Clare, S., Matthews, P. M., Brady, J. M., & Smith, S. M. (2003). Characterization and propagation of uncertainty in diffusion-weighted MR imaging [_eprint: https://onlinelibrary.wiley.com/doi/pdf/10.1002/mrm.10609]. *Magnetic Resonance in Medicine*, *50*(5), 1077–1088. https://doi.org/10.1002/mrm.10609

Bergan, J. F., Ro, P., Ro, D., & Knudsen, E. I. (2005). Hunting increases adaptive auditory map plasticity in adult barn owls [Publisher: Soc Neuroscience]. *Journal of Neuroscience*, *25*(42), 9816–9820.

Berman, R. A., & Wurtz, R. H. (2010). Functional Identification of a Pulvinar Path from Superior Colliculus to Cortical Area MT. *Journal of Neuroscience*, *30*(18), 6342–6354. https://doi.org/10.1523/JNEUROSCI.6176-09.2010

Beyeler, M., Rokem, A., Boynton, G. M., & Fine, I. (2017). Learning to see again: Biological constraints on cortical plasticity and the implications for sight restoration technologies. *Journal of neural engineering*, *14*(5), 051003. https://doi.org/10.1088/1741-2552/aa795e

Bowers, A. R., Ananyev, E., Mandel, A. J., Goldstein, R. B., & Peli, E. (2014). Driving With Hemianopia: IV. Head Scanning and Detection at Intersections in a Simulator [Publisher: The Association for Research in Vision and Ophthalmology]. *Investigative Ophthalmology & Visual Science*, *55*(3), 1540–1548. https://doi.org/10.1167/iovs.13-12748

Bowers, A. R., Tant, M., & Peli, E. (2012). A Pilot Evaluation of On-Road Detection Performance by Drivers with Hemianopia Using Oblique Peripheral Prisms [Publisher: Hindawi]. *Stroke Research and Treatment*, *2012*, e176806. https://doi.org/10.1155/2012/176806

Boynton, G. M., Engel, S. A., Glover, G. H., & Heeger, D. J. (1996). Linear systems analysis of functional magnetic resonance imaging in human V1 [Publisher: Soc Neuroscience]. *Journal of Neuroscience*, *16*(13), 4207–4221.

Brainard, M. S., & Knudsen, E. I. (1998). Sensitive Periods for Visual Calibration of the Auditory Space Map in the Barn Owl Optic Tectum. *The Journal of Neuroscience*, *18*(10), 3929–3942. https://doi.org/10.1523/JNEUROSCI.18-10-03929.1998

Bridge, H., Thomas, O., Jbabdi, S., & Cowey, A. (2008). Changes in connectivity after visual cortical brain damage underlie altered visual function [Publisher: Oxford University Press]. *Brain*, *131*(6), 1433–1444.

Calford, M. B., Wang, C., Taglianetti, V., Waleszczyk, W. J., Burke, W., & Dreher, B. (2000). Plasticity in adult cat visual cortex (area 17) following circumscribed monocular lesions of all retinal layers. *The Journal of Physiology*, *524*(Pt 2), 587–602. https://doi.org/10.1111/j.1469-7793.2000.t01-1-00587.x

Casco, C., Barollo, M., Contemori, G., & Battaglini, L. (2018). Neural restoration training improves visual functions and expands visual field of patients with homonymous visual field defects [Publisher: IOS Press]. *Restorative Neurology and Neuroscience*, *36*(2), 275–291.

Caselles, V., Kimmel, R., & Sapiro, G. (1995). Geodesic active contours. *Proceedings of IEEE International Conference on Computer Vision*, 694–699. https://doi.org/10.1109/ICCV.1995.466871

Cavanaugh, M. R., Blanchard, L. M., McDermott, M., Lam, B. L., Tamhankar, M., & Feldon, S. E. (2020). Efficacy of Visual Retraining in the Hemianopic Field after Stroke: Results of a Randomized Clinical Trial. *Ophthalmology*. https://doi.org/10.1016/j.ophtha.2020.11.020

Charng, J., Sanfilippo, P. G., Attia, M. S., Dolliver, M., Arunachalam, S., Chew, A. L., Wong, E. N., Mackey, D. A., & Chen, F. K. (2020).

Interpreting MAIA Microperimetry Using Age- and Retinal Loci-Specific Reference Thresholds. *Translational Vision Science & Technology*, *9*(7), 19. https://doi.org/10.1167/tvst.9.7.19

Chen, J., & Cohen-Adad, J. (2019). Functional Magnetic Resonance Imaging. In R. Narayan (Ed.), *Encyclopedia of Biomedical Engineering* (pp. 533–544). Elsevier. https://doi.org/10.1016/B978-0-12-801238-3.99948-3

Chen, J. L., Lin, W. C., Cha, J. W., So, P. T., Kubota, Y., & Nedivi, E. (2011). Structural basis for the role of inhibition in facilitating adult brain plasticity. *Nature neuroscience*, *14*(5), 587–594. https://doi.org/10.1038/nn.2799

Chew, E. Y., Clemons, T. E., Jaffe, G. J., Johnson, C. A., Farsiu, S., Lad, E. M., Guymer, R., Rosenfeld, P., Hubschman, J.-P., & Constable, I. (2019). Effect of ciliary neurotrophic factor on retinal neurodegeneration in patients with macular telangiectasia type 2: A randomized clinical trial [Publisher: Elsevier]. *Ophthalmology*, *126*(4), 540–549.

Cohen, J. M., & Waiss, B. (1996). Visual field remediation. *Remediation and Management of Low Vision. St. Louis: Mosby*, 1–25.

Corbetta, M., & Shulman, G. L. (2002). Control of goal-directed and stimulus-driven attention in the brain [Publisher: Nature Publishing Group]. *Nature reviews neuroscience*, *3*(3), 201–215.

Cottaar, M. (2020). FDT/UserGuide - FslWiki. Retrieved June 21, 2022, from https://fsl.fmrib.ox.ac.uk/fsl/fslwiki/FDT/UserGuide#DTIFIT

Cowey, A. (2010). The blindsight saga. *Experimental Brain Research*, *200*(1), 3–24. https://doi.org/10.1007/s00221-009-1914-2

Cramer, S. C. (2008). Repairing the human brain after stroke: I. Mechanisms of spontaneous recovery [_eprint: https://onlinelibrary.wiley.com/doi/pdf/10.1002/ana.21393]. *Annals of Neurology*, *63*(3), 272–287. https://doi.org/10.1002/ana.21393

Crossland, M. D., Sims, M., Galbraith, R. F., & Rubin, G. S. (2004). Evaluation of a new quantitative technique to assess the number and extent of preferred retinal loci in macular disease. *Vision Research*, *44*(13), 1537–1546. https://doi.org/10.1016/j.visres.2004.01.006

Dalton, C. M., Brex, P. A., Jenkins, R., Fox, N. C., Miszkiel, K. A., Crum, W. R., O'Riordan, J. I., Plant, G. T., Thompson, A. J., & Miller, D. H. (2002). Progressive ventricular enlargement in patients with clinically isolated syndromes is associated with the early development of multiple sclerosis [Publisher: BMJ Publishing Group Ltd Section: Paper]. *Journal of Neurology, Neurosurgery & Psychiatry*, *73*(2), 141–147. https://doi.org/10.1136/jnnp.73.2.141

Darian-Smith, C., & Gilbert, C. D. (1994). Axonal sprouting accompanies functional reorganization in adult cat striate cortex. *Nature*, *368*(6473), 737–740. https://doi.org/10.1038/368737a0

Das, A., & Huxlin, K. R. (2010). New Approaches to Visual Rehabilitation for Cortical Blindness: Outcomes and Putative Mechanisms [Publisher: SAGE Publications Inc STM]. *The Neuroscientist*, *16*(4), 374–387. https://doi.org/10.1177/1073858409356112

De Groot, M., Vernooij, M. W., Klein, S., Ikram, M. A., Vos, F. M., Smith, S. M., Niessen, W. J., & Andersson, J. L. (2013). Improving alignment in tract-based spatial statistics: Evaluation and optimization of image registration [Publisher: Elsevier]. *Neuroimage*, *76*, 400–411.

DeYoe, E. A., Carman, G. J., Bandettini, P., Glickman, S., Wieser, J. O. N., Cox, R., Miller, D., & Neitz, J. (1996). Mapping striate and extrastriate visual areas in human cerebral cortex [Publisher: National Acad Sciences]. *Proceedings of the National Academy of Sciences*, *93*(6), 2382–2386.

Dilks, D. D., Serences, J. T., Rosenau, B. J., Yantis, S., & McCloskey, M. (2007). Human Adult Cortical Reorganization and Consequent Visual Distortion. *Journal of Neuroscience*, *27*(36), 9585–9594. https://doi.org/10.1523/JNEUROSCI.2650-07.2007

Donoghue, J. P. (1995). Plasticity of adult sensorimotor representations. *Current Opinion in Neurobiology*, *5*(6), 749–754. https://doi.org/10.1016/0959-4388(95)80102-2

Drieghe, D., Brysbaert, M., & Desmet, T. (2005). Parafoveal-on-foveal effects on eye movements in text reading: Does an extra space make a difference? [Publisher: Elsevier]. *Vision research*, *45*(13), 1693–1706.

Duchowski, A. T., & Duchowski, A. T. (2017). *Eye tracking methodology: Theory and practice*. Springer.

Dumoulin, S. O., Hoge, R. D., Baker, C. L., Hess, R. F., Achtman, R. L., & Evans, A. C. (2003). Automatic volumetric segmentation of human visual retinotopic cortex. *NeuroImage*, *18*(3), 576–587. https://doi.org/10.1016/S1053-8119(02)00058-7

Dumoulin, S. O., & Wandell, B. A. (2008). Population receptive field estimates in human visual cortex. *NeuroImage*, *39*(2), 647–660. https://doi.org/10.1016/j.neuroimage.2007.09.034

Duszynski, L. R. (1955). Hemianopsia dichroic mirror device. *American journal of ophthalmology*, *39*(6), 876–878.

Ehmke, C., & Wilson, S. (2007). Identifying web usability problems from eyetracking data.

England, P. H. (2018). Briefing Document: First Incidence of Stroke—Estimates for England 2007 to 2016 [Publisher: PHE publications London, England].

Eriksson, P. S., Perfilieva, E., Björk-Eriksson, T., Alborn, A.-M., Nordborg, C., Peterson, D. A., & Gage, F. H. (1998). Neurogenesis in the adult human hippocampus [Publisher: Nature Publishing Group]. *Nature medicine*, *4*(11), 1313–1317.

Ernst, R. R., & Anderson, W. A. (1966). Application of Fourier transform spectroscopy to magnetic resonance [Publisher: American Institute of Physics]. *Review of Scientific Instruments*, *37*(1), 93–102.

Fendrich, R., Wessinger, C. M., & Gazzaniga, M. S. (1992). Residual vision in a scotoma: Implications for blindsight [Publisher: American Association for the Advancement of Science]. *Science*, *258*(5087), 1489–1491.

Fiez, J. A., Damasio, H., & Grabowski, T. J. (2000). Lesion segmentation and manual warping to a reference brain: Intra- and interobserver reliability [_eprint: https://onlinelibrary.wiley.com/doi/pdf/10.1002/%28SICI%291097-0193%28200004%2
Human Brain Mapping, *9*(4), 192–211. https://doi.org/10.1002/(SICI)1097-0193(200004)9:4<192::AID-HBM2>3.0.CO;2-Y

Fischl, B. (2012). FreeSurfer. *NeuroImage*, *62*(2), 774–781. https://doi.org/10.1016/j.neuroimage.2012.01.021

Friston, K. J., Fletcher, P., Josephs, O., Holmes, A., Rugg, M. D., & Turner, R. (1998). Event-related fMRI: Characterizing differential responses [Publisher: Elsevier]. *Neuroimage*, *7*(1), 30–40.

Fuchs, E., & Flügge, G. (2014). Adult Neuroplasticity: More Than 40 Years of Research [Publisher: Hindawi]. *Neural Plasticity*, *2014*, e541870. https://doi.org/10.1155/2014/541870

Fujino, T., Kigazawa, K. I., & Yamada, R. (1986). Homonymous hemianopia: A retrospective study of 140 cases. *Neuro-Ophthalmology*, *6*(1), 17–21. https://doi.org/10.3109/01658108608997320

Gammeri, R., Iacono, C., Ricci, R., & Salatino, A. (2020). Unilateral spatial neglect after stroke: Current insights [Place: New Zealand Publisher: Dove Medical Press Ltd.]. *Neuropsychiatric Disease and Treatment*, *16*. https://doi.org/10.2147/NDT.S171461

Gardner, J. L., Merriam, E. P., Schluppeck, D., Besle, J., & Heeger, D. J. (2018). mrTools: Analysis and visualization package for functional magnetic resonance imaging data. https://doi.org/10.5281/zenodo.1299483

Gegenfurtner, K., Kiper, D., & Levitt, J. (1997). Functional Properties of Neurons in Macaque Area V3. *Journal of neurophysiology*, *77*, 1906–23. https://doi.org/10.1152/jn.1997.77.4.1906

Giorgi, R. G., Woods, R. L., & Peli, E. (2009). Clinical and Laboratory Evaluation of Peripheral Prism Glasses for Hemianopia. *Optometry and vision science : official publication of the American Academy of Optometry*, *86*(5), 492–502. https://doi.org/10.1097/OPX.0b013e31819f9e4d

Girotti, F., Casazza, M., Musicco, M., & Avanzini, G. (1983). Oculomotor disorders in cortical lesions in man: The role of unilateral neglect [Publisher: Elsevier]. *Neuropsychologia*, *21*(5), 543–553.

Goebel, R., Muckli, L., Zanella, F. E., Singer, W., & Stoerig, P. (2001). Sustained extrastriate cortical activation without visual awareness revealed by fMRI studies of hemianopic patients. *Vision Research*, *41*(10), 1459–1474. https://doi.org/10.1016/S0042-6989(01)00069-4

Goodlaw, E. (1983). Review of low vision management of visual field defects. *Optom Monthly*, *74*, 363–8.

Goodwin, D. (2014). Homonymous hemianopia: Challenges and solutions. *Clinical Ophthalmology (Auckland, N.Z.)*, *8*, 1919–1927. https://doi.org/10.2147/OPTH.S59452

Graessner, J. (2011). Frequently Asked Questions: Diffusion-Weighted Imaging (DWI), 4.

Graziadei, P. P. C., Karlan, M. S., Monti, G. A., & Bernstein, J. J. (1980). Neurogenesis of sensory neurons in the primate olfactory system after section of the fila olfactoria [Publisher: Elsevier]. *Brain Research*, *186*(2), 289–300.

Greene, C. A., Dumoulin, S. O., Harvey, B. M., & Ress, D. (2014). Measurement of population receptive fields in human early visual cortex using back-projection tomography. *Journal of Vision*, *14*(1), 17. https://doi.org/10.1167/14.1.17

Grill-Spector, K. (2003). The neural basis of object perception. *Current Opinion in Neurobiology*, *13*(2), 159–166. https://doi.org/10.1016/S0959-4388(03)00040-0

Hallett, M. (2002). Recent Advances in Stroke Rehabilitation [Publisher: SAGE Publications Inc STM]. *Neurorehabilitation and Neural Repair*, *16*(2), 211–217. https://doi.org/10.1177/0888439002016002004

Halligan, P. W., Marshall, J. C., & Wade, D. T. (1990). Do visual field deficits exacerbate visuo-spatial neglect? *Journal of Neurology, Neurosurgery & Psychiatry*, *53*(6), 487–491. https://doi.org/10.1136/jnnp.53.6.487

Halligan, P. W., Cockburn, J., & Wilson, B. A. (1991). The behavioural assessment of visual neglect [Publisher: Taylor & Francis]. *Neuropsychological rehabilitation*, *1*(1), 5–32.

Hennel, F. (1997). Multiple-shot echo-planar imaging [_eprint: https://onlinelibrary.wiley.com/doi/pdf/10.1002/%28SICI%291099-0534%281997%299
Concepts in Magnetic Resonance, *9*(1), 43–58. https://doi.org/10.1002/(SICI)1099-0534(1997)9:1<43::AID-CMR4>3.0.CO;2-N

Hess, R. F., & Pointer, J. S. (1989). Spatial and temporal contrast sensitivity in hemianopia: A comparative study of the sighted and blind hemifields [Publisher: Oxford University Press]. *Brain*, *112*(4), 871–894.

Hinman, J., Rost, N., Leung, T., Montaner, J., Muir, K., Brown, S., Arenillas, J., Feldmann, E., & Liebeskind, D. (2016). Principles of precision medicine in stroke. *Journal of Neurology, Neurosurgery & Psychiatry*, *88*, jnnp–2016. https://doi.org/10.1136/jnnp-2016-314587

Holliday, I. E., Anderson, S. J., & Harding, G. F. A. (1997). Magnetoencephalographic evidence for non-geniculostriate visual input to human cortical area V5. *Neuropsychologia*, *35*(8), 1139–1146. https://doi.org/10.1016/S0028-3932(97)00033-X

Holmqvist, K., Nyström, M., Andersson, R., Dewhurst, R., Halszka, J., & van de Weijer, J. (2011). *Eye Tracking : A Comprehensive Guide to Methods and Measures*. Oxford University Press. Retrieved May 31, 2022, from http://lup.lub.lu.se/record/1852359

Horton, J. C. (2005). Disappointing results from Nova Vision's visual restoration therapy. *British Journal of Ophthalmology*, *89*(1), 1–2. https://doi.org/10.1136/bjo.2004.058214

Horton, J. C., Economides, J. R., & Adams, D. L. (2021). The Mechanism of Macular Sparing. *Annual review of vision science*, *7*, 155–179. https://doi.org/10.1146/annurev-vision-100119-125406

Horton, J. C., Fahle, M., Mulder, T., & Trauzettel-Klosinski, S. (2017). Adaptation, perceptual learning, and plasticity of brain functions. *Graefe's Archive for Clinical and Experimental Ophthalmology*, *255*(3), 435–447. https://doi.org/10.1007/s00417-016-3580-y

Horton, J. C., & Hocking, D. R. (1998). Monocular core zones and binocular border strips in primate striate cortex revealed by the contrasting effects of enucleation, eyelid suture, and retinal laser lesions on cytochrome oxidase activity [Publisher: Soc Neuroscience]. *Journal of Neuroscience*, *18*(14), 5433–5455.

Houston, K. E., Peli, E., Goldstein, R. B., & Bowers, A. R. (2018). Driving with hemianopia VI: Peripheral prisms and perceptual-motor training improve detection in a driving simulator [Publisher: The Association for Research in Vision and Ophthalmology]. *Translational vision science & technology*, *7*(1), 5–5.

Huber, A. (1992). Homonymous hemianopia [Publisher: Taylor & Francis]. *Neuro-ophthalmology*, *12*(6), 351–366.

Huettel, S. A., Song, A. W., & McCarthy, G. (2004). *Functional magnetic resonance imaging* (Vol. 1). Sinauer Associates Sunderland, MA.

Huisman, T. (2010). Diffusion-weighted and diffusion tensor imaging of the brain, made easy. *Cancer Imaging*, *10*(1A), S163–S171. https://doi.org/10.1102/1470-7330.2010.9023

Huxlin, K. R., Martin, T., Kelly, K., Riley, M., Friedman, D. I., Burgin, W. S., & Hayhoe, M. (2009). Perceptual Relearning of Complex Visual Motion after V1 Damage in Humans. *Journal of Neuroscience*, *29*(13), 3981–3991. https://doi.org/10.1523/JNEUROSCI.4882-08.2009

Jenkinson, M., Beckmann, C. F., Behrens, T. E., Woolrich, M. W., & Smith, S. M. (2012). Fsl [Publisher: Elsevier]. *Neuroimage*, *62*(2), 782–790.

Johnson, C. A., Wall, M., & Thompson, H. S. (2011). A history of perimetry and visual field testing [Publisher: LWW]. *Optometry and Vision Science*, *88*(1), E8–E15.

Kaas, J. H., Krubitzer, L. A., Chino, Y. M., Langston, A. L., Polley, E. H., & Blair, N. (1990). Reorganization of retinotopic cortical maps in adult mammals after lesions of the retina [Publisher: American Association for the Advancement of Science]. *Science*, *248*(4952), 229–231.

Kanwisher, N., McDermott, J., & Chun, M. M. (1997). The Fusiform Face Area: A Module in Human Extrastriate Cortex Specialized for Face Perception, 10.

Karmarkar, U. R., & Dan, Y. (2006). Experience-Dependent Plasticity in Adult Visual Cortex. *Neuron*, *52*(4), 577–585. https://doi.org/10.1016/j.neuron.2006.11.001

Karnath, H.-O., & Hartje, W. (1987). Residual information processing in the neglected visual half-field [Publisher: Springer]. *Journal of neurology*, *234*(3), 180–184.

Kasten, E., Poggel, D. A., & Sabel, B. A. (2000). Computer-based training of stimulus detection improves color and simple pattern recognition in the defective field of hemianopic subjects [Publisher: MIT Press One Rogers Street, Cambridge, MA 02142-1209, USA journals-info . . .]. *Journal of cognitive neuroscience*, *12*(6), 1001–1012.

Kasten, E., & Sabel, B. A. (1995). Visual field enlargement after computer training in brain-damaged patients with homonymous deficits: An open pilot trial [Publisher: IOS Press]. *Restorative neurology and neuroscience*, *8*(3), 113–127.

Kasten, E., Wüst, S., Behrens-Baumann, W., & Sabel, B. A. (1998). Computer-based training for the treatment of partial blindness [Publisher: Nature Publishing Group]. *Nature medicine*, *4*(9), 1083–1087.

Keck, T., Mrsic-Flogel, T. D., Vaz Afonso, M., Eysel, U. T., Bonhoeffer, T., & Hübener, M. (2008). Massive restructuring of neuronal circuits during functional reorganization of adult visual cortex. *Nature Neuroscience*, *11*(10), 1162–1167. https://doi.org/10.1038/nn.2181

Kedar, S., Zhang, X., Lynn, M. J., Newman, N. J., & Biousse, V. (2007). Congruency in Homonymous Hemianopia. *American Journal of Ophthalmology*, *143*(5), 772–780. https://doi.org/10.1016/j.ajo.2007.01.048

Kennedy, A. (2000). Parafoveal processing in word recognition [Publisher: SAGE Publications Sage UK: London, England]. *The Quarterly Journal of Experimental Psychology Section A*, *53*(2), 429–455.

Kornack, D. R., & Rakic, P. (1999). Continuation of neurogenesis in the hippocampus of the adult macaque monkey [Publisher: National Acad Sciences]. *Proceedings of the National Academy of Sciences*, *96*(10), 5768–5773.

Kortuem, C., Marx, T., Altpeter, E. K., Trauzettel-Klosinski, S., & Kuester-Gruber, S. (2021). Comparing Reading Speeds for Reading Standardized Single Sentences and Paragraphs in Patients with Maculopathy [Number: 3]. *Ophthalmic Research*, *64*(3), 512–522. https://doi.org/10.1159/000509687

Kupers, E. R., Edadan, A., Benson, N. C., Zuiderbaan, W., De Jong, M. C., Dumoulin, S. O., & Winawer, J. (2021). A population receptive field model of the magnetoencephalography response [Publisher: Elsevier]. *NeuroImage*, *244*, 118554.

Kwon, M., & Legge, G. E. (2012). Spatial-frequency requirements for reading revisited [Publisher: Elsevier]. *Vision Research*, *62*, 139–147.

Landers, J. (2003). A comparison of perimetric results with the Medmont and Humphrey perimeters. *British Journal of Ophthalmology*, *87*(6), 690–694. https://doi.org/10.1136/bjo.87.6.690

Laubrock, J., Kliegl, R., & Engbert, R. (2006). SWIFT explorations of age differences in eye movements during reading. *Neuroscience & Biobehavioral Reviews*, *30*(6), 872–884. https://doi.org/10.1016/j.neubiorev.2006.06.013

Leff, A. P., Scott, S. K., Crewes, H., Hodgson, T. L., Cowey, A., Howard, D., & Wise, R. J. S. (2000). Impaired reading in patients with right hemianopia [_eprint: https://onlinelibrary.wiley.com/doi/pdf/10.1002/1531-8249%28200002%2947%3A2%3
Annals of Neurology, *47*(2), 171–178.

https://doi.org/https://doi.org/10.1002/1531-8249(200002)47:2<171::AID-ANA6>3.0.CO;2-P

Leh, S. E., Johansen-Berg, H., & Ptito, A. (2006). Unconscious vision: New insights into the neuronal correlate of blindsight using diffusion tractography. *Brain*, *129*(7), 1822–1832. https://doi.org/10.1093/brain/awl111

Lerma-Usabiaga, G., Winawer, J., & Wandell, B. A. (2021). Population Receptive Field Shapes in Early Visual Cortex Are Nearly Circular. *The Journal of Neuroscience*, *41*(11), 2420–2427. https://doi.org/10.1523/JNEUROSCI.3052-20.2021

Liew, S.-L., Anglin, J. M., Banks, N. W., Sondag, M., Ito, K. L., Kim, H., Chan, J., Ito, J., Jung, C., Khoshab, N., Lefebvre, S., Nakamura, W., Saldana, D., Schmiesing, A., Tran, C., Vo, D., Ard, T., Heydari, P., Kim, B., . . . Stroud, A. (2018). A large, open source dataset of stroke anatomical brain images and manual lesion segmentations [Number: 1 Publisher: Nature Publishing Group]. *Scientific Data*, *5*(1), 180011. https://doi.org/10.1038/sdata.2018.11

Logothetis, N. K. (2003). The Underpinnings of the BOLD Functional Magnetic Resonance Imaging Signal. *The Journal of Neuroscience*, *23*(10), 3963–3971. https://doi.org/10.1523/JNEUROSCI.23-10-03963.2003

Lutkenhoff, E. S., Rosenberg, M., Chiang, J., Zhang, K., Pickard, J. D., Owen, A. M., & Monti, M. M. (2014). Optimized Brain Extraction for Pathological Brains (optiBET). *PLoS ONE*, *9*(12). https://doi.org/10.1371/journal.pone.0115551

Luu, C. D., Dimitrov, P. N., Wu, Z., Ayton, L. N., Makeyeva, G., Aung, K.-Z., Varsamidis, M., Robman, L., Vingrys, A. J., & Guymer, R. H. (2013).

Static and Flicker Perimetry in Age-Related Macular Degeneration. *Investigative Ophthalmology & Visual Science, 54*(5), 3560–3568. https://doi.org/10.1167/iovs.12-10465

Mannan, S. K., Pambakian, A. L. M., & Kennard, C. (2010). Compensatory strategies following visual search training in patients with homonymous hemianopia: An eye movement study. *Journal of Neurology*, *257*(11), 1812–1821. https://doi.org/10.1007/s00415-010-5615-3

Mansfield, P. (1977). Multi-planar image formation using NMR spin echoes. *Journal of Physics C: Solid State Physics*, *10*(3), L55–L58. https://doi.org/10.1088/0022-3719/10/3/004

Markowitz, S. N., & Reyes, S. V. (2013). Microperimetry and clinical practice: An evidence-based review. *Canadian Journal of Ophthalmology*, *48*(5), 350–357. https://doi.org/10.1016/j.jcjo.2012.03.004

Marshall, R. S., Chmayssani, M., O'Brien, K. A., Handy, C., & Greenstein, V. C. (2010). Visual field expansion after visual restoration therapy [Publisher: SAGE Publications Ltd STM]. *Clinical Rehabilitation*, *24*(11), 1027–1035. https://doi.org/10.1177/0269215510362323

Mathews, P. M., Ramulu, P. Y., Swenor, B. S., Utine, C. A., Rubin, G. S., & Akpek, E. K. (2017). Functional impairment of reading in patients with dry eye [Number: 4]. *British Journal of Ophthalmology*, *101*(4), 481–486. https://doi.org/10.1136/bjophthalmol-2015-308237

MathWorks. (2016). Version 9.10.0 (R2016b).

McConkie, G. W., & Rayner, K. (1975). The span of the effective stimulus during a fixation in reading [Publisher: Springer]. *Perception & Psychophysics*, *17*(6), 578–586.

McConkie, G. W., & Rayner, K. (1976). Asymmetry of the perceptual span in reading. *Bulletin of the Psychonomic Society*, *8*(5), 365–368. https://doi.org/10.3758/BF03335168

McKeefry, D. J., Burton, M. P., & Morland, A. B. (2010). The contribution of human cortical area V3A to the perception of chromatic motion: A transcranial magnetic stimulation study [_eprint: https://onlinelibrary.wiley.com/doi/pdf/10.1111/j.1460-9568.2010.07095.x]. *European Journal of Neuroscience*, *31*(3), 575–584. https://doi.org/10.1111/j.1460-9568.2010.07095.x

Meienberg, O., Zangemeister, H., Rosenberg, M., Hoyt, W., & Stark, L. (1981). Saccadic Eye-Movement Strategies in Patients with Homonymous Hemianopia. *Annals of neurology*, *9*, 537–44. https://doi.org/10.1002/ana.410090605

Merkel, C., Hopf, J.-M., & Schoenfeld, M. A. (2018). Spatial elongation of population receptive field profiles revealed by model-free fMRI back-projection. *Human Brain Mapping*, *39*(6), 2472–2481. https://doi.org/10.1002/hbm.24015

Merkel, C., Hopf, J.-M., & Schoenfeld, M. A. (2020). Modulating the global orientation bias of the visual system changes population receptive field elongations. *Human Brain Mapping*, *41*(7), 1765–1774. https://doi.org/10.1002/hbm.24909

Miller, M. W., & Nowakowski, R. S. (1988). Use of bromodeoxyuridine-immunohistochemistry to examine the proliferation, migration and time of origin of cells in the central nervous system [Publisher: Elsevier]. *Brain research*, *457*(1), 44–52.

Millington, R. S., James-Galton, M., Maia Da Silva, M. N., Plant, G. T., & Bridge, H. (2017). Lateralized occipital degeneration in posterior cortical atrophy predicts visual field deficits. *NeuroImage: Clinical*, *14*, 242–249. https://doi.org/10.1016/j.nicl.2017.01.012

Molina-Martín, A., Piñero, D. P., & Pérez-Cambrodí, R. J. (2016). Reliability and intersession agreement of microperimetric and fixation measurements obtained with a new microperimeter in normal eyes [Publisher: Taylor & Francis]. *Current Eye Research*, *41*(3), 400–409.

Mönter, V. M., Crabb, D. P., & Artes, P. H. (2017). Reclaiming the Periphery: Automated Kinetic Perimetry for Measuring Peripheral Visual Fields in Patients With Glaucoma. *Investigative Ophthalmology & Visual Science*, *58*(2), 868–875. https://doi.org/10.1167/iovs.16-19868

Morales, M. U., Saker, S., Wilde, C., Pellizzari, C., Pallikaris, A., Notaroberto, N., Rubinstein, M., Rui, C., Limoli, P., Smolek, M. K., & Amoaku, W. M. (2016). Reference Clinical Database for Fixation Stability Metrics in Normal Subjects Measured with the MAIA Microperimeter. *Translational Vision Science & Technology*, *5*(6), 6. https://doi.org/10.1167/tvst.5.6.6

Mori, S., Crain, B. J., Chacko, V. P., & Van Zijl, P. C. M. (1999). Three-dimensional tracking of axonal projections in the brain by magnetic resonance imaging [_eprint: https://onlinelibrary.wiley.com/doi/pdf/10.1002/1531-8249%28199902%2945%3A2%3 *Annals of Neurology*, *45*(2), 265–269. https://doi.org/10.1002/1531-8249(199902)45:2<265::AID-ANA21>3.0.CO;2-3

Morland, A. B., Lê, S., Carroll, E., Hoffmann, M. B., & Pambakian, A. (2004). The role of spared calcarine cortex and lateral occipital cortex in the responses of human hemianopes to visual motion [Publisher: MIT Press One Rogers Street, Cambridge, MA

02142-1209, USA journals-info . . .]. *Journal of cognitive neuroscience*, *16*(2), 204–218.

Morris, R. K., Rayner, K., & Pollatsek, A. (1990). Eye movement guidance in reading: The role of parafoveal letter and space information. [Publisher: American Psychological Association]. *Journal of Experimental Psychology: Human Perception and Performance*, *16*(2), 268.

Moss, A. M., Harrison, A. R., & Lee, M. S. (2014). Patients With Homonymous Hemianopia Become Visually Qualified to Drive Using Novel Monocular Sector Prisms. *Journal of Neuro-Ophthalmology*, *34*(1), 53–56. https://doi.org/10.1097/WNO.0000000000000060

Nayak, B., & Dharwadkar, S. (2014). Interpretation of autoperimetry. *Journal of Clinical Ophthalmology and Research*, *2*, 31. https://doi.org/10.4103/2320-3897.122659

Nelles, G., Esser, J., Eckstein, A., Tiede, A., Gerhard, H., & Diener, H. C. (2001). Compensatory visual field training for patients with hemianopia after stroke. *Neuroscience Letters*, *306*(3), 189–192. https://doi.org/10.1016/S0304-3940(01)01907-3

Nelles, G., Pscherer, A., de Greiff, A., Forsting, M., Gerhard, H., Esser, J., & Diener, H. C. (2009). Eye-movement training-induced plasticity in patients with post-stroke hemianopia [Publisher: Springer]. *Journal of neurology*, *256*(5), 726–733.

Nestares, O., & Heeger, D. J. (2000). Robust multiresolution alignment of MRI brain volumes [_eprint: https://onlinelibrary.wiley.com/doi/pdf/10.1002/%28SICI%291522-2594%28200005%2

Magnetic Resonance in Medicine, *43*(5), 705–715.

https://doi.org/10.1002/(SICI)1522-2594(200005)43:5<705::AID-MRM13>3.0.CO;2-R

Nottebohm, F. (1989). From bird song to neurogenesis [Publisher: JSTOR]. *Scientific American*, *260*(2), 74–79.

Nyström, M., & Holmqvist, K. (2010). An adaptive algorithm for fixation, saccade, and glissade detection in eyetracking data. *Behavior Research Methods*, *42*(1), 188–204. https://doi.org/10.3758/BRM.42.1.188

O'Donnell, L. J., & Westin, C.-F. (2011). An introduction to diffusion tensor image analysis. *Neurosurgery clinics of North America*, *22*(2), 185–viii. https://doi.org/10.1016/j.nec.2010.12.004

Office, N. A. (2010). Department of Health: Progress in improving stroke care - National Audit Office (NAO) Report. Retrieved February 4, 2022, from https://www.nao.org.uk/report/department-of-health-progress-in-improving-stroke-care/

Ogawa, S., Lee, T. M., Kay, A. R., & Tank, D. W. (1990). Brain magnetic resonance imaging with contrast dependent on blood oxygenation. *Proceedings of the National Academy of Sciences*, *87*(24), 9868–9872. https://doi.org/10.1073/pnas.87.24.9868

Pambakian, A. L. M., Mannan, S. K., Hodgson, T. L., & Kennard, C. (2004). Saccadic visual search training: A treatment for patients with homonymous hemianopia [Publisher: BMJ Publishing Group Ltd]. *Journal of Neurology, Neurosurgery & Psychiatry*, *75*(10), 1443–1448.

Papageorgiou, E., Hardiess, G., Schaeffel, F., Wiethoelter, H., Karnath, H.-O., Mallot, H., Schoenfisch, B., & Schiefer, U. (2007). Assessment of vision-related quality of life in patients with homonymous visual field defects. *Graefe's Archive for Clinical and*

Experimental Ophthalmology, *245*(12), 1749–1758. https://doi.org/10.1007/s00417-007-0644-z

Papanikolaou, A., Keliris, G. A., Papageorgiou, T. D., Shao, Y., Krapp, E., Papageorgiou, E., Stingl, K., Bruckmann, A., Schiefer, U., Logothetis, N. K., & Smirnakis, S. M. (2014). Population receptive field analysis of the primary visual cortex complements perimetry in patients with homonymous visual field defects. *Proceedings of the National Academy of Sciences*, *111*(16), E1656–E1665. https://doi.org/10.1073/pnas.1317074111

Paterson, K. B., & Jordan, T. R. (2010). Effects of increased letter spacing on word identification and eye guidance during reading. *Memory & Cognition*, *38*(4), 502–512. https://doi.org/10.3758/MC.38.4.502

Paterson, K. B., McGowan, V. A., & Jordan, T. R. (2013). Filtered text reveals adult age differences in reading: Evidence from eye movements. [Publisher: American Psychological Association]. *Psychology and Aging*, *28*(2), 352.

Patterson, D. (2019). FSL Lesion Normalization. Retrieved June 1, 2022, from https://neuroimaging-core-docs.readthedocs.io/en/latest/pages/fsl_anat_normalization-lesion.html

Peirce, J. W. (2007). PsychoPy—psychophysics software in Python [Number: 1-2 Publisher: Elsevier]. *Journal of neuroscience methods*, *162*(1-2), 8–13.

Peli, E. (2000). Field expansion for homonymous hemianopia by optically induced peripheral exotropia [Publisher: LWW]. *Optometry and Vision Science*, *77*(9), 453–464.

Peli, E., Bowers, A. R., Keeney, K., & Jung, J.-H. (2016). High-power prismatic devices for oblique peripheral prisms [Publisher: Wolters Kluwer Health]. *Optometry and Vision Science*, *93*(5), 521.

Phelps, C. D. (1978). Principles of Quantitative Perimetry: Testing and Interpreting the Visual Field [Publisher: American Medical Association]. *Archives of Ophthalmology*, *96*(9), 1709–1709.

Pleger, B., Foerster, A.-F., Widdig, W., Henschel, M., Nicolas, V., Jansen, A., Frank, A., Knecht, S., Schwenkreis, P., & Tegenthoff, M. (2003). Functional magnetic resonance imaging mirrors recovery of visual perception after repetitive tachistoscopic stimulation in patients with partial cortical blindness. *Neuroscience Letters*, *335*(3), 192–196. https://doi.org/10.1016/S0304-3940(02)01153-9

Poggel, D. A., Kasten, E., Müller-Oehring, E. M., Sabel, B. A., & Brandt, S. A. (2001). Unusual spontaneous and training induced visual field recovery in a patient with a gunshot lesion [Publisher: BMJ Publishing Group Ltd]. *Journal of Neurology, Neurosurgery & Psychiatry*, *70*(2), 236–239.

Poggel, D. A., Mueller, I., Kasten, E., Bunzenthal, U., & Sabel, B. A. (2010). Subjective and objective outcome measures of computer-based vision restoration training [Publisher: IOS Press]. *NeuroRehabilitation*, *27*(2), 173–187.

Pollatsek, A., & Rayner, K. (1982). Eye movement control in reading: The role of word boundaries. [Publisher: American Psychological Association]. *Journal of Experimental Psychology: Human Perception and Performance*, *8*(6), 817.

Pollock, A., Hazelton, C., Henderson, C. A., Angilley, J., Dhillon, B., Langhorne, P., Livingstone, K., Munro, F. A., Orr, H., & Rowe, F. J.

(2011). Interventions for visual field defects in patients with stroke [Publisher: John Wiley & Sons, Ltd]. *Cochrane Database of Systematic Reviews*, (10).

Puig, J., Blasco, G., Schlaug, G., Stinear, C., Daunis-i-Estadella, P., Biarnes, C., Figueras, J., Serena, J., Hernández-Pérez, M., Alberich-Bayarri, A., Castellanos, M., Liebeskind, D., Demchuk, A., Menon, B., Thomalla, G., Nael, K., Wintermark, M., & Pedraza, S. (2017). Diffusion tensor imaging as a prognostic biomarker for motor recovery and rehabilitation after stroke. *Neuroradiology*, *59*. https://doi.org/10.1007/s00234-017-1816-0

Qian, X., Lin, Y., Zhao, Y., Yue, X., Lu, B., & Wang, J. (2017). Objective Ventricle Segmentation in Brain CT with Ischemic Stroke Based on Anatomical Knowledge [Publisher: Hindawi]. *BioMed Research International*, *2017*, e8690892. https://doi.org/10.1155/2017/8690892

R Core Team. (2021). *R: A Language and Environment for Statistical Computing*. R Foundation for Statistical Computing. https://www.R-project.org/

Radoeva, P. D., Prasad, S., Brainard, D. H., & Aguirre, G. K. (2008). Neural activity within area V1 reflects unconscious visual performance in a case of blindsight [Publisher: MIT Press One Rogers Street, Cambridge, MA 02142-1209, USA journals-info . . .]. *Journal of cognitive neuroscience*, *20*(11), 1927–1939.

Ramulu, P. Y., Swenor, B. K., Jefferys, J. L., & Rubin, G. S. (2013). Description and Validation of a Test to Evaluate Sustained Silent Reading [Number: 1 Publisher: The Association for Research in

Vision and Ophthalmology]. *Investigative Ophthalmology & Visual Science*, *54*(1), 673–680. https://doi.org/10.1167/iovs.12-10617

Rayner, K. (1998). Eye movements in reading and information processing: 20 years of research [Place: US Publisher: American Psychological Association]. *Psychological Bulletin*, *124*(3), 372–422. https://doi.org/10.1037/0033-2909.124.3.372

Rayner, K., Castelhano, M. S., & Yang, J. (2009). Eye movements and the perceptual span in older and younger readers. [Publisher: American Psychological Association]. *Psychology and aging*, *24*(3), 755.

Rayner, K., Slattery, T. J., & Bélanger, N. N. (2010). Eye movements, the perceptual span, and reading speed. *Psychonomic Bulletin & Review*, *17*(6), 834–839. https://doi.org/10.3758/PBR.17.6.834

Rayner, K., Well, A. D., Pollatsek, A., & Bertera, J. H. (1982). The availability of useful information to the right of fixation in reading. *Perception & Psychophysics*, *31*(6), 537–550. https://doi.org/10.3758/BF03204186

Reinhard, J., Schreiber, A., Schiefer, U., Kasten, E., Sabel, B. A., Kenkel, S., Vonthein, R., & Trauzettel-Klosinski, S. (2005). Does visual restitution training change absolute homonymous visual field defects? A fundus controlled study [Publisher: BMJ Publishing Group Ltd]. *British Journal of Ophthalmology*, *89*(1), 30–35.

Risse, S., & Kliegl, R. (2011). Adult age differences in the perceptual span during reading. *Psychology and Aging*, *26*(2), 451–460. https://doi.org/10.1037/a0021616

Roh, M., Laíns, I., Shin, H. J., Park, D. H., Mach, S., Vavvas, D. G., Kim, I. K., Miller, J. W., Husain, D., & Miller, J. B. (2019). Microperimetry in age-related macular degeneration: Association with macular morphology assessed by optical coherence tomography [Publisher: BMJ Publishing Group Ltd]. *British Journal of Ophthalmology*, *103*(12), 1769–1776.

Ross, J. E., Clarke, D. D., & Bron, A. J. (1985). Effect of age on contrast sensitivity function: Uniocular and binocular findings. *British Journal of Ophthalmology*, *69*(1), 51–56. https://doi.org/10.1136/bjo.69.1.51

Roth, T., Sokolov, A. N., Messias, A., Roth, P., Weller, M., & Trauzettel-Klosinski, S. (2009). Comparing explorative saccade and flicker training in hemianopia: A randomized controlled study. *Neurology*, *72*(4), 324–331. https://doi.org/10.1212/01.wnl.0000341276.65721.f2

Rowe, F. J. (2010). Who Sees Visual Impairment Following Stroke? [Publisher: Taylor & Francis _eprint: https://doi.org/10.3109/09273971003758396]. *Strabismus*, *18*(2), 37–40. https://doi.org/10.3109/09273971003758396

Rowe, F. J., Hepworth, L. R., Howard, C., Hanna, K. L., Cheyne, C. P., & Currie, J. (2019). High incidence and prevalence of visual problems after acute stroke: An epidemiology study with implications for service delivery [Publisher: Public Library of Science]. *PLOS ONE*, *14*(3), e0213035. https://doi.org/10.1371/journal.pone.0213035

Rowe, F. J., Wright, D., Brand, D., Jackson, C., Harrison, S., Maan, T., Scott, C., Vogwell, L., Peel, S., Akerman, N., Dodridge, C., Howard, C., Shipman, T., Sperring, U., MacDiarmid, S., & Freeman, C. (2013). A Prospective Profile of Visual Field Loss following Stroke: Prevalence, Type, Rehabilitation, and Outcome [ISSN: 2314-6133

Pages: e719096 Publisher: Hindawi Volume: 2013]. https://doi.org/https://doi.org/10.1155/2013/719096

Sabel, B. A. (1997). Unrecognized Potential of Surviving Neurons:: Within-systems Plasticity, Recovery of Function, and the Hypothesis of Minimal Residual Structure [Publisher: Sage Publications Sage CA: Thousand Oaks, CA]. *The Neuroscientist*, *3*(6), 366–370.

Sahraie, A., Trevethan, C. T., MacLeod, M. J., Murray, A. D., Olson, J. A., & Weiskrantz, L. (2006). Increased sensitivity after repeated stimulation of residual spatial channels in blindsight. *Proceedings of the National Academy of Sciences*, *103*(40), 14971–14976. https://doi.org/10.1073/pnas.0607073103

Saj, A., Honoré, J., Bernati, T., & Rousseaux, M. (2010). *Post-stroke delay influences consequences of hemianopia on spatial neglect signs* [Pages: S56].

Sakoe, H., & Chiba, S. (1978). Dynamic programming algorithm optimization for spoken word recognition [Publisher: IEEE]. *IEEE transactions on acoustics, speech, and signal processing*, *26*(1), 43–49.

Salvucci, D. D., & Goldberg, J. H. (2000). Identifying fixations and saccades in eye-tracking protocols. *Proceedings of the 2000 symposium on Eye tracking research & applications*, 71–78.

Sanchez-Lopez, J., Cardobi, N., Pedersini, C. A., Savazzi, S., & Marzi, C. A. (2020). What cortical areas are responsible for blindsight in hemianopic patients? *Cortex*, *132*, 113–134. https://doi.org/10.1016/j.cortex.2020.08.007

Sanders, M. D., Warrington, E., Marshall, J., & Wieskrantz, L. (1974). " Blindsight": Vision in a field defect [Publisher: Elsevier]. *The Lancet*, *303*(7860), 707–708.

Savitzky, A., & Golay, M. J. (1964). Smoothing and differentiation of data by simplified least squares procedures. [Number: 8 Publisher: ACS Publications]. *Analytical chemistry*, *36*(8), 1627–1639.

Schmid, M. C., Mrowka, S. W., Turchi, J., Saunders, R. C., Wilke, M., Peters, A. J., Ye, F. Q., & Leopold, D. A. (2010). Blindsight depends on the lateral geniculate nucleus [Publisher: Nature Publishing Group]. *Nature*, *466*(7304), 373–377.

Schmidt, C. F., Degonda, N., Luechinger, R., Henke, K., & Boesiger, P. (2005). Sensitivity-encoded (SENSE) echo planar fMRI at 3T in the medial temporal lobe. *NeuroImage*, *25*(2), 625–641. https://doi.org/10.1016/j.neuroimage.2004.12.002

Schotter, E. R., Angele, B., & Rayner, K. (2012). Parafoveal processing in reading. *Attention, Perception, & Psychophysics*, *74*(1), 5–35. https://doi.org/10.3758/s13414-011-0219-2

Schuett, S. (2009). The rehabilitation of hemianopic dyslexia [Num Pages: 11 Place: London, United States Publisher: Nature Publishing Group]. *Nature Reviews. Neurology*, *5*(8), 427–437. https://doi.org/http://dx.doi.org/10.1038/nrneurol.2009.97

Schuett, S., Heywood, C. A., Kentridge, R. W., & Zihl, J. (2008a). Rehabilitation of hemianopic dyslexia: Are words necessary for re-learning oculomotor control? *Brain*, *131*(12), 3156–3168. https://doi.org/10.1093/brain/awn285

Schuett, S., Heywood, C. A., Kentridge, R. W., & Zihl, J. (2008b). The significance of visual information processing in reading: Insights from hemianopic dyslexia. *Neuropsychologia*, *46*(10), 2445–2462. https://doi.org/10.1016/j.neuropsychologia.2008.04.016

Shinoura, N., Suzuki, Y., Yamada, R., Tabei, Y., Saito, K., & Yagi, K. (2009). Damage to the right superior longitudinal fasciculus in the inferior parietal lobe plays a role in spatial neglect. *Neuropsychologia*, *47*(12), 2600–2603. https://doi.org/10.1016/j.neuropsychologia.2009.05.010

Silson, E. H., Reynolds, R. C., Kravitz, D. J., & Baker, C. I. (2018). Differential Sampling of Visual Space in Ventral and Dorsal Early Visual Cortex. *The Journal of Neuroscience*, *38*(9), 2294–2303. https://doi.org/10.1523/JNEUROSCI.2717-17.2018

Silvanto, J., Cowey, A., & Walsh, V. (2008). Inducing conscious perception of colour in blindsight. *Current Biology*, *18*(20), R950–R951. https://doi.org/10.1016/j.cub.2008.08.016

Silvanto, J., Walsh, V., & Cowey, A. (2009). Abnormal functional connectivity between ipsilesional V5/MT+ and contralesional striate cortex (V1) in blindsight [Publisher: Springer]. *Experimental brain research*, *193*(4), 645–650.

Sincich, L. C., Park, K. F., Wohlgemuth, M. J., & Horton, J. C. (2004). Bypassing V1: A direct geniculate input to area MT [Number: 10 Publisher: Nature Publishing Group]. *Nature Neuroscience*, *7*(10), 1123–1128. https://doi.org/10.1038/nn1318

Smirnakis, S., Brewer, A., Schmid, M., Tolias, A., Schüz, A., Augath, M., Inhoffen, W., Wandell, B., & Logothetis, N. (2005). Lack of long-term cortical reorganization after macaque retinal lesions. *Nature*, *435*, 300–7. https://doi.org/10.1038/nature03495

Smith, A. M., Lewis, B. K., Ruttimann, U. E., Ye, F. Q., Sinnwell, T. M., Yang, Y., Duyn, J. H., & Frank, J. A. (1999). Investigation of low frequency drift in fMRI signal. *NeuroImage*, 526–533.

Smith, A., Singh, K., Williams, A., & Greenlee, M. (2001). Estimating Receptive Field Size from fMRI Data in Human Striate and Extrastriate Visual Cortex. *Cerebral Cortex*, *11*(12), 1182–1190. https://doi.org/10.1093/cercor/11.12.1182

Smith, J. L. (1962). Homonymous Hemianopia * : A review of one hundred cases [Publisher: Elsevier]. *American Journal of Ophthalmology*, *54*(4), 616–623. https://doi.org/10.1016/0002-9394(62)92192-X

Smith, S. M., Jenkinson, M., Woolrich, M. W., Beckmann, C. F., Behrens, T. E. J., Johansen-Berg, H., Bannister, P. R., De Luca, M., Drobnjak, I., Flitney, D. E., Niazy, R. K., Saunders, J., Vickers, J., Zhang, Y., De Stefano, N., Brady, J. M., & Matthews, P. M. (2004). Advances in functional and structural MR image analysis and implementation as FSL. *NeuroImage*, *23*, S208–S219. https://doi.org/10.1016/j.neuroimage.2004.07.051

Smith, S. M. (2002). Fast robust automated brain extraction. *Human Brain Mapping*, *17*(3), 143–155. https://doi.org/10.1002/hbm.10062

Spalding, K. L., Bergmann, O., Alkass, K., Bernard, S., Salehpour, M., Huttner, H. B., Boström, E., Westerlund, I., Vial, C., & Buchholz, B. A. (2013). Dynamics of hippocampal neurogenesis in adult humans [Publisher: Elsevier]. *Cell*, *153*(6), 1219–1227.

Steinman, R. M. (1965). Effect of Target Size, Luminance, and Color on Monocular Fixation*. *Journal of the Optical Society of America*, *55*(9), 1158. https://doi.org/10.1364/JOSA.55.001158

Susanna Jr, R., & Vessani, R. M. (2009). Staging glaucoma patient: Why and how? [Publisher: Bentham Science Publishers]. *The open ophthalmology journal*, *3*, 59.

Szlyk, J. P., Seiple, W., Stelmack, J., & McMahon, T. (2005). Use of prisms for navigation and driving in hemianopic patients [Publisher: Wiley Online Library]. *Ophthalmic and Physiological Optics*, *25*(2), 128–135.

Tae, W.-S., Ham, B.-J., Pyun, S.-B., Kang, S.-H., & Kim, B.-J. (2018). Current Clinical Applications of Diffusion-Tensor Imaging in Neurological Disorders. *Journal of Clinical Neurology*, *14*(2), 129. https://doi.org/10.3988/jcn.2018.14.2.129

Takeuchi, N., & Izumi, S.-I. (2013). Rehabilitation with Poststroke Motor Recovery: A Review with a Focus on Neural Plasticity [Publisher: Hindawi]. *Stroke Research and Treatment*, *2013*, e128641. https://doi.org/10.1155/2013/128641

Tootell, R. B., Mendola, J. D., Hadjikhani, N. K., Ledden, P. J., Liu, A. K., Reppas, J. B., Sereno, M. I., & Dale, A. M. (1997). Functional analysis of V3A and related areas in human visual cortex [Publisher: Soc Neuroscience]. *Journal of Neuroscience*, *17*(18), 7060–7078.

Townend, B. S., Sturm, J. W., Petsoglou, C., O'Leary, B., Whyte, S., & Crimmins, D. (2007). Perimetric homonymous visual field loss post-stroke. *Journal of Clinical Neuroscience*, *14*(8), 754–756. https://doi.org/10.1016/j.jocn.2006.02.022

Trauzettel-Klosinski, S., & Brendler, K. (1998a). Eye movements in reading with hemianopic field defects: The significance of clinical parameters [Number: 2]. *Graefe's Archive for Clinical and Experimental Ophthalmology*, *236*(2), 91–102. https://doi.org/10.1007/s004170050048

Trauzettel-Klosinski, S., & Brendler, K. (1998b). Eye movements in reading with hemianopic field defects: The significance of clinical parameters

[Number: 2]. *Graefe's Archive for Clinical and Experimental Ophthalmology*, *236*(2), 91–102. https://doi.org/10.1007/s004170050048

Trauzettel-Klosinski, S., Dietz, K., & Group, t. I. S. (2012). Standardized Assessment of Reading Performance: The New International Reading Speed Texts IReST [Number: 9 Publisher: The Association for Research in Vision and Ophthalmology]. *Investigative Ophthalmology & Visual Science*, *53*(9), 5452–5461. https://doi.org/10.1167/iovs.11-8284

Trauzettel-Klosinski, S., & Reinhard, J. (1998). The vertical field border in hemianopia and its significance for fixation and reading [Publisher: JB LIPPINCOTT CO]. *Investigative Ophthalmology and Visual Science*, *39*, 2177–2185.

Uchino, K., Kolikonda, M. K., Brown, D., Kovi, S., Collins, D., Khawaja, Z., Buletko, A. B., Russman, A. N., & Hussain, M. S. (2020). Decline in stroke presentations during COVID-19 surge [Publisher: Am Heart Assoc]. *Stroke*, *51*(8), 2544–2547.

Unema, P., & Rötting, M. (1990). Differences in Eye Movements and Mental Workload between Experienced and Inexperienced Drivers In: D. Brogan (Ed.), Visual Search.

Uppal, S., Walker, R., & Atkins, E. (2012). Cavernous Malformation of the Optic Chiasm - A Diagnostic and Treatment Dilemma. *The Canadian journal of neurological sciences. Le journal canadien des sciences neurologiques*, *39*, 533–5. https://doi.org/10.1017/S0317167100014104

van Essen, D. C., Donahue, C. J., Coalson, T. S., Kennedy, H., Hayashi, T., & Glasser, M. F. (2019). Cerebral cortical folding, parcellation, and connectivity in humans, nonhuman primates, and mice. *Proceedings of the National Academy of Sciences*, *116*(52), 26173–26180.

Vuilleumier, P. (2013). Mapping the functional neuroanatomy of spatial neglect and human parietal lobe functions: Progress and challenges [_eprint: https://onlinelibrary.wiley.com/doi/pdf/10.1111/nyas.12161]. *Annals of the New York Academy of Sciences*, *1296*(1), 50–74. https://doi.org/10.1111/nyas.12161

Walker, R., Mannan, S., Maurer, D., Pambakian, A. L. M., & Kennard, C. (2000). The oculomotor distractor effect in normal and hemianopic vision [Publisher: Royal Society]. *Proceedings of the Royal Society of London. Series B: Biological Sciences*, *267*(1442), 431–438. https://doi.org/10.1098/rspb.2000.1018

Walker, R., Findlay, J. M., Young, A. W., & Welch, J. (1991). Disentangling neglect and hemianopia. *Neuropsychologia*, *29*(10), 1019–1027. https://doi.org/10.1016/0028-3932(91)90065-G

Wandell, B. A., Dumoulin, S. O., & Brewer, A. A. (2007). Visual Field Maps in Human Cortex. *Neuron*, *56*(2), 366–383. https://doi.org/10.1016/j.neuron.2007.10.012

Wandell, B. A., & Smirnakis, S. M. (2009). Plasticity and stability of visual field maps in adult primary visual cortex. *Nature reviews. Neuroscience*, *10*(12), 873–884. https://doi.org/10.1038/nrn2741

Wang, J., He, L., Zheng, H., & Lu, Z.-L. (2014). Optimizing the magnetization-prepared rapid gradient-echo (MP-RAGE) sequence [Publisher: Public Library of Science San Francisco, USA]. *PloS one*, *9*(5), e96899.

Wang, L., Mruczek, R. E., Arcaro, M. J., & Kastner, S. (2015). Probabilistic Maps of Visual Topography in Human Cortex. *Cerebral Cortex (New York, NY)*, *25*(10), 3911–3931. https://doi.org/10.1093/cercor/bhu277

Warner, C. E., Kwan, W. C., Wright, D., Johnston, L. A., Egan, G. F., & Bourne, J. A. (2015). Preservation of Vision by the Pulvinar following Early-Life Primary Visual Cortex Lesions. *Current Biology*, *25*(4), 424–434. https://doi.org/10.1016/j.cub.2014.12.028

Warrington, S., Bryant, K., Khrapitchev, A., Sallet, J., Charquero-Ballester, M., Douaud, G., Jbabdi, S., Mars, R., & Sotiropoulos, S. (2019). XTRACT-Standardised protocols for automated tractography and connectivity blueprints in the human and macaque brain. bioRxiv. *doi*, *10*(804641), 804641.

Watanabe, T., Takayama, Y., Kawasaki, T., Yagi, H., & Akiguchi, I. (2006). A functional MRI study of unilateral spatial neglect. *Trends in brain mapping research* (pp. 173–199). Nova Science Publishers Inc. New York.

Weiger, M., Pruessmann, K. P., Österbauer, R., Börnert, P., Boesiger, P., & Jezzard, P. (2002). Sensitivity-encoded single-shot spiral imaging for reduced susceptibility artifacts in BOLD fMRI [_eprint: https://onlinelibrary.wiley.com/doi/pdf/10.1002/mrm.10286]. *Magnetic Resonance in Medicine*, *48*(5), 860–866. https://doi.org/10.1002/mrm.10286

Weiskrantz, L., Harlow, A., & Barbur, J. L. (1991). Factors affecting visual sensitivity in a hemianopic subject [Publisher: Oxford University Press]. *Brain*, *114*(5), 2269–2282.

Weiskrantz, L., Barbur, J. L., & Sahraie, A. (1995). Parameters affecting conscious versus unconscious visual discrimination with damage to the visual cortex (V1) [Publisher: National Acad Sciences]. *Proceedings of the National Academy of Sciences*, *92*(13), 6122–6126.

Wessinger, C. M., Fendrich, R., & Gazzaniga, M. S. (1999). Variability of residual vision in hemianopic subjects [Publisher: IOS Press]. *Restorative neurology and neuroscience*, *15*(2-3), 243–253.

Westheimer, G. (2014). Can perceptual learning compensate for optical image blur? *Vision Research*, *94*, 58–61. https://doi.org/10.1016/j.visres.2013.11.001

Williams, C. C., Perea, M., Pollatsek, A., & Rayner, K. (2006). Previewing the neighborhood: The role of orthographic neighbors as parafoveal previews in reading. [Publisher: American Psychological Association]. *Journal of Experimental Psychology: Human Perception and Performance*, *32*(4), 1072.

Wong, E. N., Morgan, W. H., & Chen, F. K. (2017). Intersession test–retest variability of 10-2 MAIA microperimetry in fixation-threatening glaucoma. *Clinical Ophthalmology (Auckland, N.Z.)*, *11*, 745–752. https://doi.org/10.2147/OPTH.S131371

Wood, J. M., McGwin, G., Jr, Elgin, J., Vaphiades, M. S., Braswell, R. A., DeCarlo, D. K., Kline, L. B., & Owsley, C. (2011). Hemianopic and Quadrantanopic Field Loss, Eye and Head Movements, and Driving. *Investigative Ophthalmology & Visual Science*, *52*(3), 1220–1225. https://doi.org/10.1167/iovs.10-6296

Yeon, H., Shin, Y.-O., Lee, O.-Y., Kwon, E., & Jeong, E.-H. (2013). Temporary homonymous hemianopsia after epidural blood patch.

Obstetrics & gynecology science, *56*, 130–133. https://doi.org/10.5468/OGS.2013.56.2.130

Yildirim, F., Carvalho, J., & Cornelissen, F. W. (2018). A second-order orientation-contrast stimulus for population-receptive-field-based retinotopic mapping. *NeuroImage*, *164*, 183–193. https://doi.org/10.1016/j.neuroimage.2017.06.073

Yushkevich, P. A., Gao, Y., & Gerig, G. (2016). ITK-SNAP: An interactive tool for semi-automatic segmentation of multi-modality biomedical images [ISSN: 1558-4615]. *2016 38th Annual International Conference of the IEEE Engineering in Medicine and Biology Society (EMBC)*, 3342–3345. https://doi.org/10.1109/EMBC.2016.7591443

Yushkevich, P. A., Piven, J., Hazlett, H. C., Smith, R. G., Ho, S., Gee, J. C., & Gerig, G. (2006). User-guided 3D active contour segmentation of anatomical structures: Significantly improved efficiency and reliability [http://www.itksnap.org/]. *NeuroImage*, *31*(3), 1116–1128. https://doi.org/10.1016/j.neuroimage.2006.01.015

Zangemeister, H., Oechsner, U., & Freksa, C. (1995). Short-term adaptation of eye movements in patients with visual hemifield defects indicates high level control of human scanpath. *Optometry and vision science : official publication of the American Academy of Optometry*, *72*, 467–77.

Zeidman, P., Silson, E. H., Schwarzkopf, D. S., Baker, C. I., & Penny, W. (2018). Bayesian population receptive field modelling. *NeuroImage*, *180*, 173–187. https://doi.org/10.1016/j.neuroimage.2017.09.008

Zhang, X., Kedar, S., Lynn, M. J., Newman, N. J., & Biousse, V. (2006a). Homonymous hemianopias: Clinical–anatomic correlations in 904 cases [Publisher: Wolters Kluwer Health, Inc. on behalf of the

American Academy of Neurology Section: Articles]. *Neurology*, *66*(6), 906–910. https://doi.org/10.1212/01.wnl.0000203913.12088.93

Zhang, X., Kedar, S., Lynn, M. J., Newman, N. J., & Biousse, V. (2006b). Natural history of homonymous hemianopia [Publisher: AAN Enterprises]. *Neurology*, *66*(6), 901–905.

Zhang, X., Kedar, S., Lynn, M. J., Newman, N. J., & Biousse, V. (2006c). Homonymous Hemianopia in Stroke. *Journal of Neuro-Ophthalmology*, *26*(3), 180–183. https://doi.org/10.1097/01.wno.0000235587.41040.39

Zhu, S. C., & Yuille, A. (1996). Region competition: Unifying snakes, region growing, and Bayes/MDL for multiband image segmentation [Conference Name: IEEE Transactions on Pattern Analysis and Machine Intelligence]. *IEEE Transactions on Pattern Analysis and Machine Intelligence*, *18*(9), 884–900. https://doi.org/10.1109/34.537343

Zihl, J. (1995). Visual scanning behavior in patients with homonymous hemianopia [Publisher: Elsevier]. *Neuropsychologia*, *33*(3), 287–303.

Zihl, J. (2010). *Rehabilitation of visual disorders after brain injury*. Psychology Press.

Zuiderbaan, W., Harvey, B. M., & Dumoulin, S. O. (2012). Modeling center–surround configurations in population receptive fields using fMRI. *Journal of Vision*, *12*(3), 10. https://doi.org/10.1167/12.3.10